Title
Plastic-Buckling Fatigue Testing of Large Diameter Steel Reinforcing Bars

Author
Duck Rodriguez, David Elias

Publication Date
2019

UNIVERSITY OF CALIFORNIA SAN DIEGO

Plastic-Buckling Fatigue Testing of Large Diameter Steel Reinforcing Bars

A dissertation submitted in partial satisfaction of the
requirements for the degree Doctor of Philosophy

in

Structural Engineering

by

David Elias Duck Rodriguez

Committee in charge:

Professor José I. Restrepo, Chair
Professor Joel P. Conte
Professor Javier E. Garay
Professor Francesco Lanza di Scalea
Professor P. Benson Shing

2019

The Dissertation of David Elias Duck Rodriguez is approved, and it is acceptable in quality and form for publication on microfilm and electronically:

Chair

University of California San Diego

2019

DEDICATION

To my parents Gloria and Mario; and to my grandmother Tina and aunt Maru.

EPIGRAPH

Get wisdom, get understanding;
Do not forget my words or turn away from them.
Do not forsake wisdom, and she will protect you;
Love her, and she will watch over you.
Wisdom is supreme; therefore get wisdom.
Though it cost all you have, get understanding.

Proverbs 4:5-7

TABLE OF CONTENTS

LIST OF SYMBOLS

$\mathrm{c}_0, \mathrm{c}_1, \mathrm{c}_2,$	Plane equation parameters
d	Cross section depth
d_b	Diameter of longitudinal reinforcement
d_{bn}	Nominal diameter of longitudinal reinforcement
d_{POI}	Distance between points of inflection in buckled reinforcement
e	Initial lateral deformation of reinforcement
$f_c^{'}$	Compressive strength of concrete
f_{cr}	Critical buckling stress
f_s	Steel stress
f_{su}	Steel uniform stress (tension)
f_{suc}	Steel uniform stress in compression
f_{u}	Steel tensile strength
f_y	Steel yield stress
f_{ys}	Yield stress of transverse (shear) reinforcement
$f_{y,l}$	Yield stress of longitudinal reinforcement
$f_{y,t}$	Yield stress of transverse reinforcement
h	Height of rebar deformation
$k_{e\text{-}bb}$	Transverse reinforcement factor for computation of $\Delta_{bb\text{-}calc}$
$\hat{\mathrm{n}}, \hat{\mathrm{n}}_0$	Normal unit vectors
n_{bar}	Number of longitudinal bars in the section
q	Reduction factor for critical load in formulation by Papia
r	Rebar lug radius
$r_{\mathrm{a}}, r_{\mathrm{b}}$	Rebar lug radii
s	On center spacing between hoops
s_{r}	Rebar lug spacing
v_0	Lateral deflection of buckled columns
w	Rebar lug width

A , A_g	(Gross) section area of column
D	Column Diameter
DI	Damage Index
DIC	Digital Image Correlation
E_{eff} , E_r	Effective (reduced) modulus
E_0 , E_s	Elastic Young’s Modulus
E_T	Tangent modulus
I	Section moment of inertia
L	Length of buckled element
L	Column shear span
L_P	Length of plastic hinge
MFR	Manufacturer
MOE	Modulus of elasticity
P_{cr}	Critical buckling load
P_{max}	Maximum tensile force
P_T	Critical buckling load according to tangent modulus theory
T/Y	Tensile-to-yield strength ratio
W_{ft}	Total dissipated energy
W_y	Dissipated elastic energy
$2N_f$	Number of half-cycles to fatigue failure
Z	Axis in the vertical direction
α	Linear factor for computation of L_p
β	Linear factor for computation of L_p
ε_a	Total strain amplitude
ε_{ave}	Average strain at plane origin
ε_{bb}	Buckling strain
ε_{cr}	Strain corresponding to f_{cr}
ε_{conc}	Strain in fiber in concave side of the buckled shape plastic hinge section

ε_{max}	Maximum strain from strain history
ε_{min}	Minimum strain from strain history
$\varepsilon'_o(1)$	Maximum compressive plastic strain in natural coordinates
$\varepsilon'_{peak,comp}$	Maximum compressive strain in natural coordinates
$\varepsilon'_{peak,tens}$	Maximum tensile strain in natural coordinates
ε_{sh}	Steel strain at onset of strain hardening
ε_{su}	Steel uniform strain (tension)
ε'_{su}	Steel uniform strain (tension) in natural coordinates
ε_{suc}	Steel uniform strain in compression
ε_y	Steel yield strain
ε_z	Strain in the Z direction
θ	Angle of rotation
κ	Curvature amplitude
λ	Transverse reinforcement configuration factor for Δ_y
μ_Δ	Displacement ductility
ξ	Linear factor for computation of L_p
ρ_{eff}	Volumetric transverse ratio $\rho_s \cdot f_{ys}/f'_c$
ρ_s	Volumetric ratio of transverse reinforcement
ρ_l	Longitudinal reinforcement ratio
τ	E_T/E_0
$\phi, \bar{\phi}$	Section curvature
ϕ_k	Computed peak curvature
$\phi_{p\text{-}bb}$	Plastic curvature in RC column when long. reinforcement reaches ε_{bb}
Δ_{bb}	Lateral displacement of column when long. Reinforcement reaches ε_{bb}
$\Delta_{bb\text{-}calc}$	Estimation of Δ_{bb} according to Berry and Eberhard
Δ_y	Lateral displacement of column at yield
Φ	Column Diameter

LIST OF FIGURES

LIST OF TABLES

ACKNOWLEDGMENTS

First and foremost, I thank God for the innumerable blessings throughout my life. All the glory and honor are His.

I want to express my gratitude to Professor Restrepo, for all his teachings and help in becoming a better engineer and a more resilient person. You’ve had a great impact in my life and will always consider you a mentor and a friend.

Special recognition goes to my parents, Gloria and Mario and aunt Maru for their unconditional love, wise guidance, and financial support. I will never be able to repay all that you have done for me. I also want to thank my maternal grandmother Tina for all that she did for me. I will always try my best to make you proud.

I want to thank my sister Jaqueline and brother Mario for all your love and support throughout my life.

I would also like to thank all members of my doctoral committee, Professor Conte, Professor Benson Shing, Professor Francesco Lanza di Scalea, and Professor Javier Garay, for their time, support, and contribution to my doctoral dissertation.

I would like to thank Mr. Darren McKay, Dr. Christopher Latham, Mr. Michael Sanders, Mr. Abdullah Hamid, Mr. Robert Beckley, and Mr. Alex Sherman for their invaluable contribution to the experimental work of my research.

I want to thank the staff at the structural engineering department for all their help. Special thanks to Yvonne Wilson and Debra Bomar for their guidance.

Also, I want to thank all my fellow students and department co-workers, both past and present. You all have made this experience much more enjoyable and will always

cherish the time spent with each of you. Most notably Dr. Gabrielle Guerrini, Dr. Rodrigo Astroza, Dr. Rodrigo Carreño, Dr. Arpit Nema, and Mr. Koorosh Lotfizadeh.

This study was made possible by funding from the California Department of Transportation under contract No. 65A0502. Technical input from Dr. Charles Sikorsky, Ray Zelinski, and Fadel Alameddine was greatly appreciated.

Chapters 1-5, in part, are a reprint of the material as it appears in *SSRP Report 17/10: Plastic buckling-straightening fatigue of large diameter reinforcing steel bars*, 2018. Duck, D. E.; Carreño, R.; and Restrepo, J. I. The dissertation author was the primary investigator and author of this report.

Chapters 2-4, in part, are currently being prepared for submission for publication of the material. Duck, D. E. & Restrepo, J. I. The dissertation author was the primary investigator and author of this material.

Chapters 3-4, in part, are currently being prepared for submission for publication of the material. Duck, D. E., Restrepo, J. I, & Carreño, R. The dissertation author was the primary investigator and author of this material.

VITA

EDUCATION

2008	Bachelor of Science, Structural Engineering, University of California, San Diego
2011	Master of Science, Structural Engineering, University of California, San Diego
2016	Candidate in Philosophy, Structural Engineering, University of California, San Diego
2019	Doctor of Philosophy, Structural Engineering, University of California, San Diego

EXPERIENCE

2008 – 2009	Design Engineer, KPFF Consulting Engineers
2010	Graduate Researcher, Large High-Performance Outdoor Shake Table, University of California, San Diego
2012-2013	Graduate Researcher, Powell Laboratory, University of California, San Diego
2014	Teaching Assistant, Department of Structural Engineering, University of California, San Diego
2013-2014	Graduate Researcher, Large High-Performance Outdoor Shake Table, University of California, San Diego

2014-2015	Structural Design Consultant, San Pablo Commercial Center, Oakland, California
2015-2017	Graduate Researcher, Powell Laboratory, University of California, San Diego
2017	Teaching Assistant, Department of Structural Engineering, University of California, San Diego
2018	Teaching Assistant, Department of Structural Engineering, University of California, San Diego
2018-Present	Project Manager, Level 3 Construction

PUBLICATIONS

Schoettler, M.J, Restrepo, J.I., Guerrini, G., **Duck, D.E.**, & Carrea, F., "*Bridge Column Response to Ground Shaking Induced by a Shake Table*". Proc. 7th National Seismic Conference on Bridges & Highways, Oakland, CA, USA, May 20-22, 2013.

Duck, D. E. & Restrepo, J. I. (2014). *TR 14-01: Repaired Spandrel Beam-Column Connection Test – Phase I.* University of California, San Diego. La Jolla: Dept. of Structural Engineering.

Duck, D. E. & Restrepo, J. I. (2014). *TR 14-02: Repaired Spandrel Beam-Column Connection Test – Phase II.* University of California, San Diego. La Jolla: Dept. of Structural Engineering.

Schoettler, M. J., Restrepo, J. I., Guerrini, G., **Duck, D. E.**, & Carrea, F. (2015). *PEER 2015/02: A Full-Scale, Single-Column Bridge Bent Tested by Shake-table Excitation.* Pacific Earthquake Engineering Research Center, University of California, Berkeley.

Duck, D. E., Carreño, R., & Restrepo, J. I. (2018). *SSRP-17/10: Plastic Buckling-Straightening Fatigue of Large Diameter Reinforcing Steel Bars (Vol I & II)*. University of California, San Diego. La Jolla: Dept. of Structural Engineering.

AWARDS

2019	"Nevada Medal for Distinguished Graduate Student Paper in Bridge Engineering", University of Nevada, Reno.

ABSTRACT OF THE DISSERTATION

Plastic-Buckling Fatigue Testing of
Large Diameter Steel Reinforcing Bars

by

David Elias Duck Rodriguez

Doctor of Philosophy in Structural Engineering

University of California San Diego, 2019

Professor José I. Restrepo, Chair

Critical regions of reinforced concrete elements designed for ductility and energy dissipation are required to sustain many large-amplitude strain cycles during rare and strong intensity earthquakes. Steel reinforcing bars in such critical regions often end up

buckling and then fracturing in a mode of failure that defines the collapse prevention limit-state. While this failure mode is commonly misnamed low-cycle fatigue, it does not meet ASTM Manual on Low-Cycle Fatigue (1969) guidelines which require to avoid buckling or bending. Instead, the term Plastic Buckling-Straightening Fatigue (PBSF) is used to describe the fatigue testing where the effects of plastic buckling are included.

Historically, the longitudinal reinforcement used for ordinary large-diameter RC bridge columns has been limited to No. 11 and smaller bars. The combination of such longitudinal reinforcement and the closely spaced transverse reinforcement at the plastic hinge region results in result in heavily congested column cages that prove challenging to build and require large amounts of labor and materials. To help reduce the congestion, larger sized bars could be used to reduce the number of bars needed to provide the same longitudinal reinforcement ratio. This would reduce the amount of material, construction time, and amount of labor needed. Furthermore, in some particular cases, the use of mechanical splices for these large diameter bars would further accelerate bridge construction by allowing the use of precast concrete techniques. However, the PBSF life of large diameter bars and their mechanical splices has not been investigated. To date, research to investigate the effects of buckling in strain-controlled fatigue testing of longitudinal steel reinforcement have focused on No. 11 and smaller bar sizes. The experimental results presented here provide the first successful PBSF data for large diameter bars and are used to implement a Damage Index to quantify the fatigue life of a reinforcing steel bar.

The innovative design and implementation of a loading apparatus used to test large-diameter reinforcing bars and their mechanical splices for PBSF is described. Main features of the loading apparatus are the high rotational stiffness and the gripping method, which was successfully achieved by exploiting the thermoplastic properties of sulfur concrete.

CHAPTER 1.

INTRODUCTION

1.1. Background

The structural design of most reinforced (RC) concrete bridge columns in seismic-prone regions rely on the ductile response of specific regions of the columns where most of the inelastic deformations are expected to develop and concentrate. To obtain such ductile response during large-amplitude cyclic strain reversals caused by earthquake excitation, closely spaced transverse reinforcement is used to confine the concrete core of the column and to help delay the buckling of the longitudinal reinforcement. Eventually, however, the longitudinal bars will buckle and fracture, as demonstrated by the full-scale testing of a large-diameter bridge column designed using such principles (Schoettler et al. 2015). By the end of testing under several stronger-than-design-earthquakes, more than half of the longitudinal bars in the plastic hinge region of the column fractured after the onset of buckling. Furthermore, incipient cracks were observed at the root of bar deformations in the concave side of the remaining buckled bars. Such failure mode suggests the deformation capacity of this type of columns may be limited by longitudinal reinforcement fatigue fracture after bar buckling. While this failure mode has been misnamed low-cycle fatigue, doing so violates the limitation placed by the ASTM Manual on Low-Cycle Fatigue (1969), which explicitly requires to avoid buckling or bending. Instead, the term Plastic Buckling-Straightening Fatigue (PBSF) is used to refer to strain-controlled fatigue testing where the effects of buckling are included. The term "low-cycle" fatigue in quotations will be used to refer to previous work where buckling was included.

Historically, the longitudinal reinforcement used for ordinary large-diameter RC bridge columns has been limited to No. 11 and smaller bars (J. B. Mander, 1983; Monti and Nuti, 1992; J. Mander, Panthaki, and Kasalanati, 1994; Gomes and Appleton, 1997; Rodriguez, Botero, and Villa, 1999; J.Brown and S.K.Kunnath, 2000; Dhakal and Maekawa, 2002; Brown and Kunnath, 2004; Bae, Mieses, and Bayrak, 2005; Massone and Moroder, 2009; Kashani, Crewe, and Alexander, 2013; Kashani, Barmi, and Malinova, 2015a). The combination of such longitudinal reinforcement and the closely spaced transverse reinforcement at the plastic hinge region results in result in heavily congested column cages that prove challenging to build and require large amounts of labor and materials. To help reduce the congestion, larger sized bars could be used to reduce the number of bars needed to provide the same longitudinal reinforcement ratio. This would reduce the amount of material, construction time, and amount of labor needed. Furthermore, in some particular cases, the use of mechanical splices for these large diameter bars would further accelerate bridge construction by allowing the use of precast concrete techniques. However, the PBSF life of large diameter bars and their mechanical splices has not been investigated. To date, research to investigate the effects of buckling in strain-controlled fatigue testing of longitudinal steel reinforcement have focused on No. 11

and smaller bar sizes. While attempts have been made to perform PBSF testing on large-diameter bars (No. 14 and larger) and their mechanical splices, the research has been hampered by difficulties in the gripping of the bars, the flexibility of the loading apparatus, and the complexity of accurately measuring strains when the bars buckle (Sanchez 2001; Kunnath et al. 2009). The experimental results presented here provide the first successful PBSF data for large diameter bars and briefly describes the innovative loading apparatus used to perform such test. Also, the results are used to implement a Damage Index to quantify the fatigue life of a reinforcing steel bar.

1.2. Motivation

In the quest to accelerate bridge construction nationwide, the development and implementation of new construction techniques is desired. Among such techniques is the wider use of precast concrete construction. The use of large diameter reinforcement, such as #18 bars, combined with mechanical splicing between precast members could greatly accelerate the construction process. However, large diameter bars have been rarely utilized in seismic-prone regions as longitudinal reinforcement of large-diameter reinforced concrete bridge columns, with #11 bars being widely used in vertical members of ordinary bridges. However, significant gaps in knowledge exist on the behavior of bridge columns built with large size bars and the large strain cyclic behavior of mechanical connections. One concern is the low-cycle fatigue life of large-diameter reinforcement, as experimental tests have shown a reduction in fatigue life with increasing bar size in #9 and smaller diameter bars (Brown and Kunnath 2004). Another uncertainty is whether large-diameter bars can be mechanically spliced at critical regions or not, and how to evaluate if a mechanical coupler is suitable as a connecting member, that is, without limiting the deformation capacity of the element or connection. An extensive literature review could not find publicly available results on the performance of mechanically spliced large-size reinforcement under large amplitude strain reversals, as most research work has focused on high-cycle fatigue. Furthermore, current qualification procedures for mechanical splices, such as California Department of Transportation (Caltrans) CT 670 (2013), only address high-cycle fatigue, for deformations well below yield.

1.3. Objective

Testing the behavior of large size reinforcement under large amplitude cyclic strains presents multiple challenges, with previous research attempts under the sponsorship of Caltrans substantially reducing their scope due to problems with the loading apparatus.

The first objective of the research was the design of a loading apparatus capable of performing the required tests, making the experimental results presented herein the first successful examination of the response of #18 size reinforcement under large amplitude strain reversals, including failure under low-cycle fatigue.

Previous experimental work has found that low-cycle fatigue in reinforcing bars results in the development and progression of cracks at the root of bar deformations (Restrepo-Posada 1993). Large shear strain concentrations, developed after the onset of bar buckling, result in a rearrangement of the steel microstructure, and micro-cracks, initially invisible to the naked eye, start to propagate and lead to bar fracture.

The current understanding of the fracture mechanism in reinforcing bars suggests an approach other than the typically used for high-cycle fatigue models (e.g. Coffin-Manson), which only consider the number of cycles and strain amplitude, is needed. First, the definition of strain requires some clarification: should the strain at the global, local or microscopic level be considered in the analysis? Perhaps the best engineering approach is to establish a relation between global and local strains, and then relate strain amplitude and damage between the two definitions. Research work by Restrepo-Posada (1993) suggests the ultimate tensile strain is strongly dependent on the maximum compressive strain experienced in the concave side of the buckled reinforcement, as well as the number of large amplitude cycles. Because of this, a practical formulation linking global and local strains in the buckled reinforcement under cyclic load is developed herein and calibrated to experimental results.

Temperature effects in the fatigue life of reinforcement are expected to be significant, as low temperatures cracks will likely propagate faster. However, the scope of this research is limited to ambient temperature tests.

1.4. Outline

A brief description of the experimental and analytical results from this study is presented as follows:

- Chapter 1 provides a description of the background, motivation, and objective of the research work.

- Chapter 2 gives a State-of-the-Art description of the theory of buckling and "low-cycle" fatigue including the effects of buckling.
- Chapter 3 gives a detailed description of the loading apparatus used in the experimental work, instrumentation, loading protocols, and experimental results for large diameter bar cyclic testing under large amplitude strain histories.
- Chapter 4 develops a strain-based Damage Index to calculate the onset of localization in a large-diameter steel reinforcing bar subjected to PBSF.

Chapter 1, in part, is a reprint of the material as it appears in *SSRP Report 17/10: Plastic buckling-straightening fatigue of large diameter reinforcing steel bars*, 2018. Duck, D. E.; Carreño, R.; and Restrepo, J. I. The dissertation author was the primary investigator and author of this report.

CHAPTER 2.

LITERATURE REVIEW

2.1. General

Buckling and straightening of longitudinal reinforcement in the plastic hinge of bridge columns can be caused by the dynamic response of a bridge during earthquake input. Such phenomena can have a significant impact on the deformation capacity and ductility of these elements. Buckling and straightening results in "low-cycle" fatigue in those regions of the buckled bar where the curvature reaches the peak. Crack initiation, see Figure 2.1, is believed to be dependent on factors like the geometry of the deformations, including local defects at the root of the bar deformations arising during the rolling process and the pattern of the deformations. On the other hand, crack propagation is believed to be dependent on the strain history and temperature of the bar at the onset of buckling, among various other parameters. Chapter 2 reviews existing literature relevant to the plastic buckling of longitudinal reinforcement as well as the fatigue life of reinforcing bars.

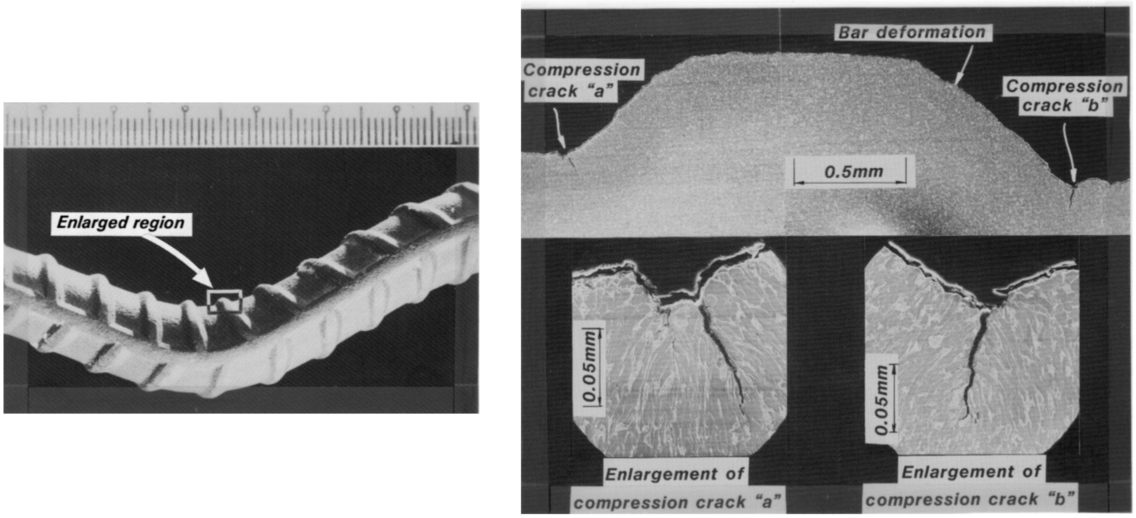

(a) (b)

Figure 2.1. Electron Microscope Image of a Longitudinal Section of a Deformed Reinforcing Bar After Buckling Showing Crack Initiation: (a) Buckled Longitudinal Bar (scale in mm.); (b) Cracks at the Bar Deformation Roots (Restrepo-Posada et al., 1993).

2.2. Plastic Buckling of Longitudinal Reinforcement

The first mathematical formulation of the buckling phenomenon was introduced by Euler in 1757 (Oldfather, Ellis, and Brown 1933). Under the assumption of a linear-elastic material, Euler found the critical axial load under which a column will develop lateral deformations,

$$P_{cr} = \frac{\pi^2 \cdot E_0 I}{L^2} \qquad \textbf{Equation 2-1}$$

Where E_0 is the elastic Young's Modulus, I is the moment of inertia of the section, L is the length between supports, and P_{cr} is the critical load for the onset of buckling. More than a century after Euler, Engesser (1889) and Considère (1891) began studying the plastic buckling phenomenon, proposing formulations similar to Euler's critical load, replacing the elastic Young's Modulus by either a tangent (Engesser, see Equation 2-2a) or effective stiffness (Considère, see Equation 2-2b) as a way to calculate the critical plastic buckling load, see Figure 2.2.

$$P_{cr}=\frac{\pi^2 \cdot E_T I}{L^2} \text{ (Engesser) (a) ; } P_{cr}=\frac{\pi^2 \cdot E_{\text{eff}} I}{L^2} \text{ (Considère) (b)}$$ **Equation 2-2**

Where E_T is the tangent modulus, and E_{eff} the effective (or reduced) modulus, satisfying the condition $E_T \leq E_{eff} \leq E_0$, although Considère did not specify a formulation for E_{eff}.

Research work into critical load leading to plastic buckling was continued by von Karman (1910), who introduced the concept of double-modulus (see Equation 2-3). This concept accounts for the effect of strain bifurcation, where some fibers in the cross section begin to decompress (unload) while the others continue deforming in compression, developing a curvature in the bar, see Figure 2.3.

Although von Karman's formulation was theoretically more accurate than any previous work, many researchers found the tangent-modulus theory (Engesser 1889) to be more consistent with experimental results (Templin et al. 1938).

$$P_{cr}=\frac{\pi^2 E_r I}{L^2} \text{ (a) ; } E_r=\frac{E_0 \cdot I_1+E_T \cdot I_2}{I_1+I_2} \text{ (b)}$$ **Equation 2-3**

where E_r is the reduced modulus (double modulus), I_1 and I_2 are the moments of inertia of the segments of the section being decompressed and compressed (after bifurcation takes place), respectively.

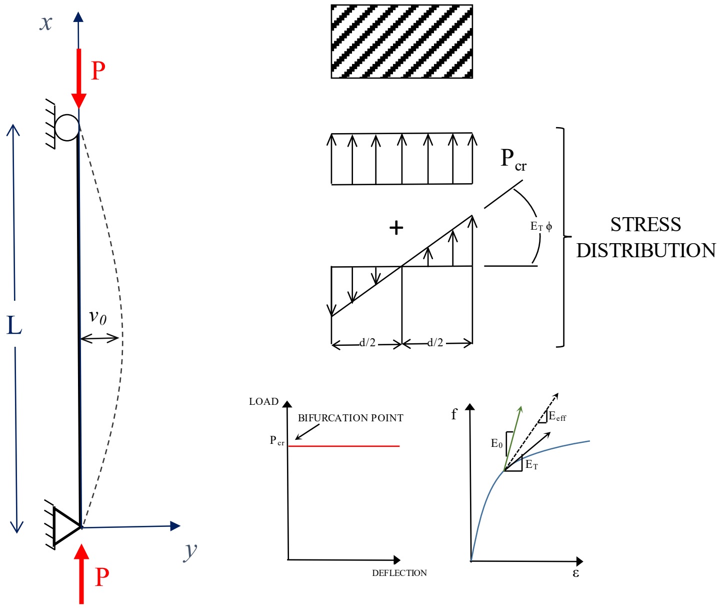

Figure 2.2. Engesser-Considère buckling formulation (Chen and Lui 1987).

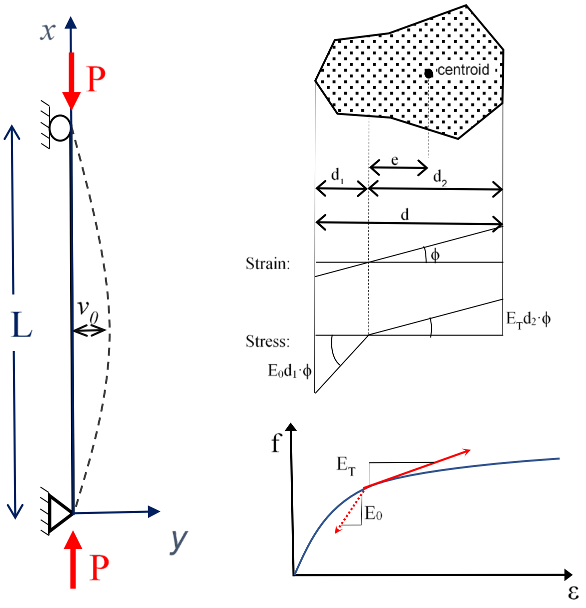

Figure 2.3. Double modulus formulation by von Karman (Chen and Lui, 1987).

The controversy between Engesser-Considère tangent modulus and Von Karman's double-modulus theories, which appear correct but led to different plastic buckling loads, was not resolved until Shanley published his historical paper "The Column Paradox" (1946). In this paper Shanley demonstrated that both formulations were in fact correct, but each represented a different state of the plastic buckling process. By assuming that a short column has additional axial load capacity after the onset of buckling, thanks to post-yield hardening of the material, it was possible to have bending without any strain reversal, the main assumption in the double-modulus theory. The tangent modulus predicts the load at the onset of buckling, while the double-modulus returns the maximum capacity of the buckled element if the tangent modulus remains constant.

To prove his formulation, Shanley (1947) analyzed the simple case of a two-legged hinge column, in which the hinge is a unit "cell" formed by two small axial elements, see Figure 2.4. By equating the internal and external moment, the critical load can be easily defined as,

$$\mathrm{P_{cr}} = P_T \cdot \left[1 + \frac{1}{\frac{d}{2 \cdot v_0} + \frac{1+\tau}{1-\tau}} \right]$$

Equation 2-4

Where $P_T = \frac{A \cdot d}{L} E_T$ and $\tau = \frac{E_T}{E_0}$, with *A* the area of the deformable cell, *d* the distance between the two legs in the cell, and v_0 the lateral deformation of the column, see Figure 2.4 and Figure 2.5.

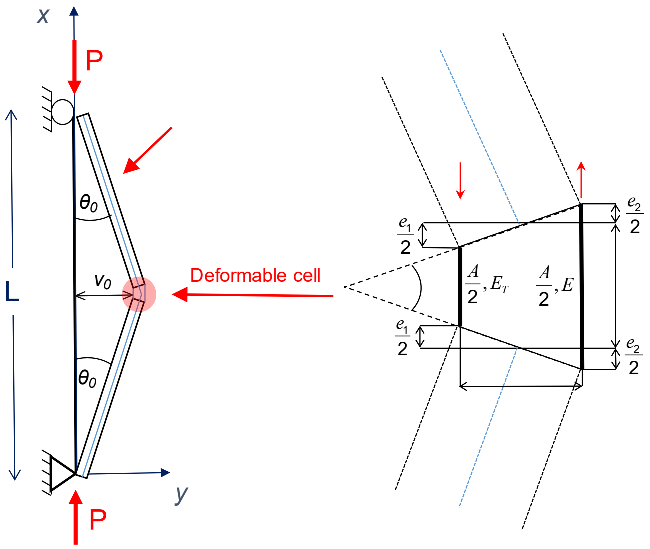

Figure 2.4. Shanley's simplified two-flange column (Shanley, 1947).

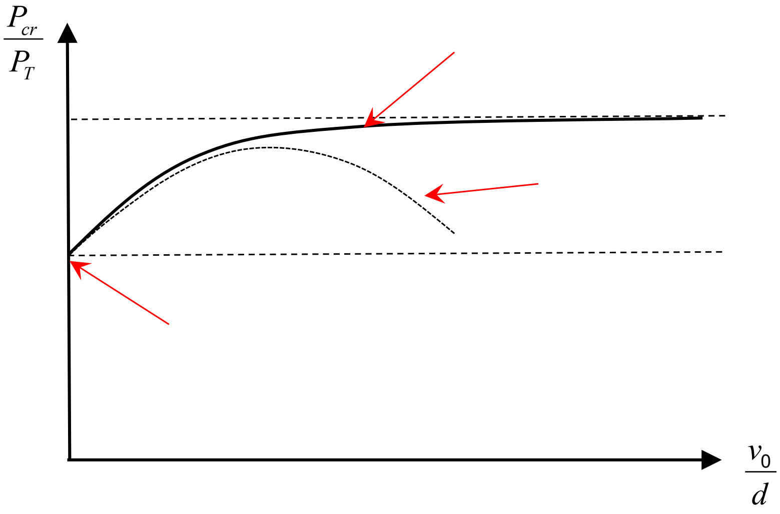

Figure 2.5. Variation of column load capacity (normalized by load at onset of buckling) vs lateral deformation (Shanley, 1947).

Following Shanley's demonstration, extensive experimental work by several authors (Madsen 1941; W. R. Osgood 1951) focused on the effect of residual stresses in steel columns, resulting in significant advances in the understanding of the behavior of these elements.

Bresler and Gilbert (1961) developed some of the earliest work on critical loads in reinforcing steel, and were the first proponents on tie spacing to ensure the stability of longitudinal reinforcing bars, based on tangent modulus theory.

One of the first closed-form solution for the hysteretic response of a pinned column under axial load, including the effect of buckling, was developed by Nonaka (1973), under the simplifying assumption the material was elastoplastic. Papadrakakis and Loukakis (1988) extended this formulation for partially restrained imperfect bars with various end conditions, using a piece-wise linear approximation of the axial force-moment interaction curve of the section. These formulations rely on the plastic-hinge concept and cannot predict the decrease in carrying capacity of the column after the first cycle of loading, which is mostly attributed to the spread of plasticity near the plastic hinges. Both the original and extended formulations were developed analytically only, without experimental verification.

Mander et al. (1994) conducted monotonic tests on reinforcing bars at different slenderness ratios, and proposed a modification to the double modulus theory, to account for the onset of buckling observed experimentally when the longitudinal reinforcement yields in compression, see Figure 2.6. This modified double modulus theory uses a secant modulus E_T', defined in Equation 2-5, instead of the tangent modulus E_T to compute the critical load P_{cr} (see Equation 2-3).

$$E_T' = \frac{f_{cr} - f(\varepsilon_{cr} - \varepsilon_{sh})}{\varepsilon_{sh}}$$

Equation 2-5

Where f_{cr} is the critical buckling stress, ε_{sh} the steel strain at onset of strain hardening, ε_{cr} the strain corresponding to f_{cr}, and $f(\varepsilon_{cr}-\varepsilon_{sh})$ is the steel stress at strain of $\varepsilon_{cr}-\varepsilon_{sh}$.

Another finding by Mander et al. (1994) was that a limit spacing of approximately six bar diameters is a suitable ratio to preclude premature longitudinal bar buckling and to ensure the desired ductility is achieved. The spacing limitation resulted from the modified double modulus theory (see Equation 2-5), by imposing the critical buckling stress f_{cr} to match the steel tension stress at a strain of 5%, well within the plastic-zone of the material,

$$\frac{s}{d_{bn}}=1.5\cdot\sqrt{\frac{E_r}{f_{cr}}}$$

Equation 2-6

where d_{bn} is the nominal diameter of the longitudinal reinforcement, and s the spacing between hoops.

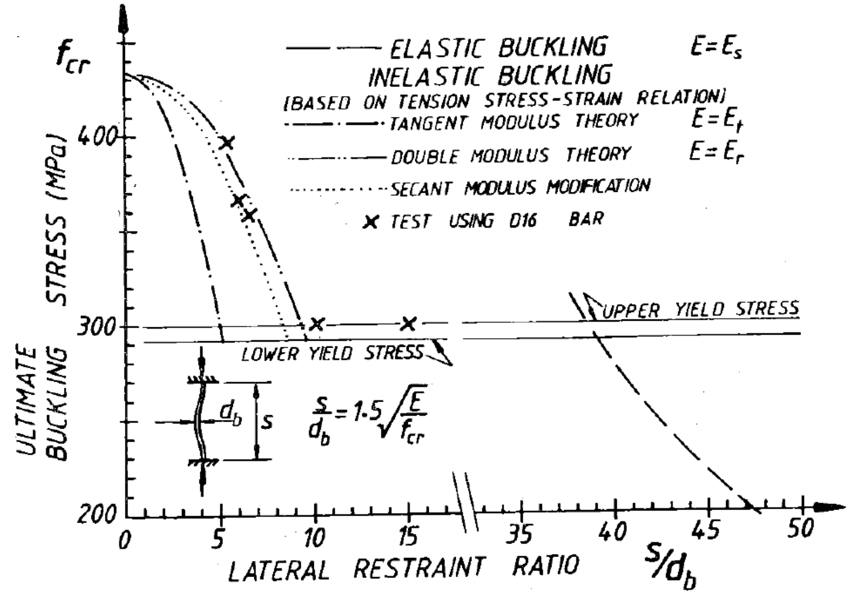

Figure 2.6. Test results compared with theoretical predictions (Mander et al., 1984).

Mander et al. formulation assumed the transverse reinforcement was stiff enough to limit bar buckling between consecutive sets of hoops, for an effective buckling length of *s/2* , Figure 2.7.Figure 2.7. Model for buckling of longitudinal reinforcement used by Mander (Zhan, 1985). Zahn (1985) extended Mander et al.'s work by testing the spacing limit (Equation 2-6) for different steel grades, and developed diagrams for the maximum spacing allowed for a given critical stress, f_{cr}, and strain, ε_{cr}, see Figure 2.8 and Figure 2.9. A linear formulation of the critical strain and stress for $s/d_b \geq 4$ (at lower slenderness levels the buckling effect is negligible) is also shown in the figures, closely matching experimental results.

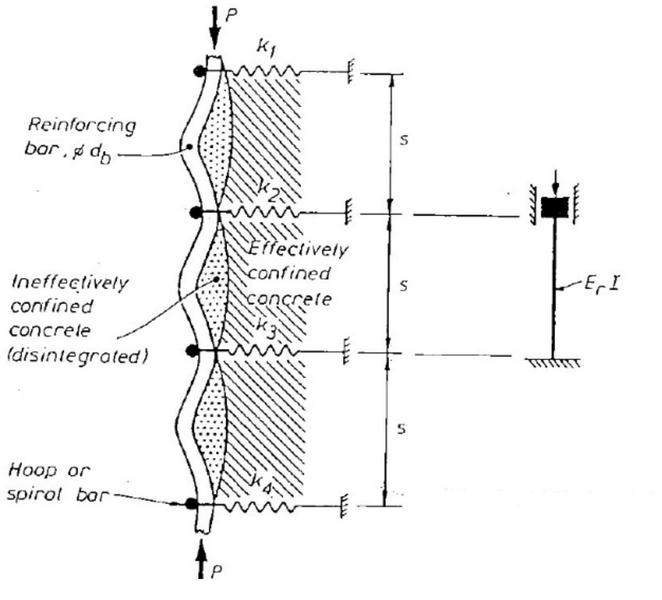

Figure 2.7. Model for buckling of longitudinal reinforcement used by Mander (Zhan, 1985).

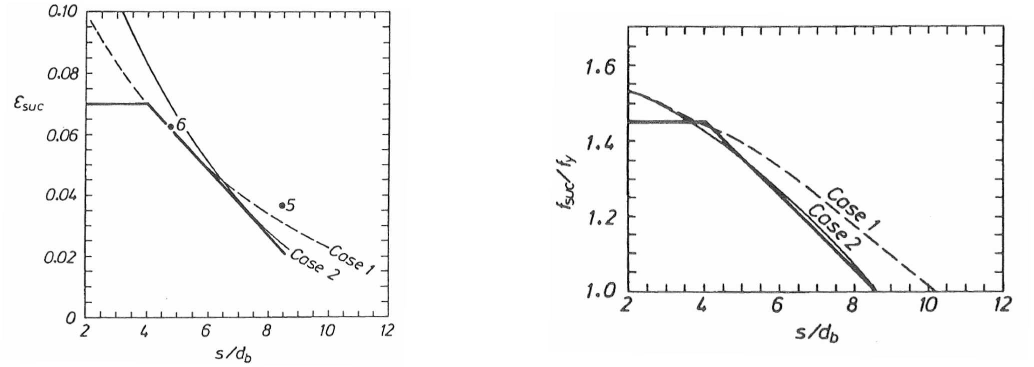

(a) (b)

Figure 2.8. Ultimate compressive strain and stress vs hoop spacing. Grade 275 MPa steel (Zahn, 1985): (a) Buckling strain ε_{suc} vs hoop spacing; (b) Normalized buckling stress f_{suc} / f_y vs hoop spacing.

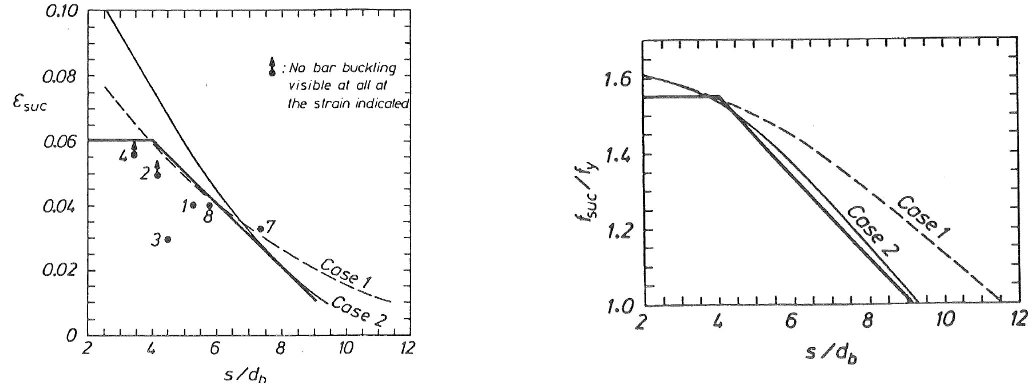

(a) (b)

Figure 2.9. Ultimate compressive strain and stress vs hoop spacing. Grade 380 MPa steel (Zahn, 1985): (a) Buckling strain ε_{suc} vs hoop spacing; (b) Normalized buckling stress f_{suc} / f_y vs hoop spacing.

In his work, Zhan observed that in some tests the bars tended to buckle across several hoops, especially for $s/d_b \leq 4$, but did not consider those cases in the analysis. Also, since the formulation assumes monotonic load, Zhan suggested a correction for cyclic loading, where the compressive strains are increased to an equivalent monotonic strain as a function of the compressive axial load. According to these researchers, the predicted results with this correction were likely unreliable, and therefore the simplistic monotonic formulation was recommended.

Tanaka et al. (1990), continuing the work by Mander et al. and Zahn, studied the buckling of reinforcement across multiple hoops, see Figure 2.10. They determined analytically the capacity of 90° hook ties and peripheral hoops to prevent buckling of longitudinal reinforcement. The analyses included the effects of core concrete expansion (Poisson effect) and initial imperfections of the longitudinal reinforcement.

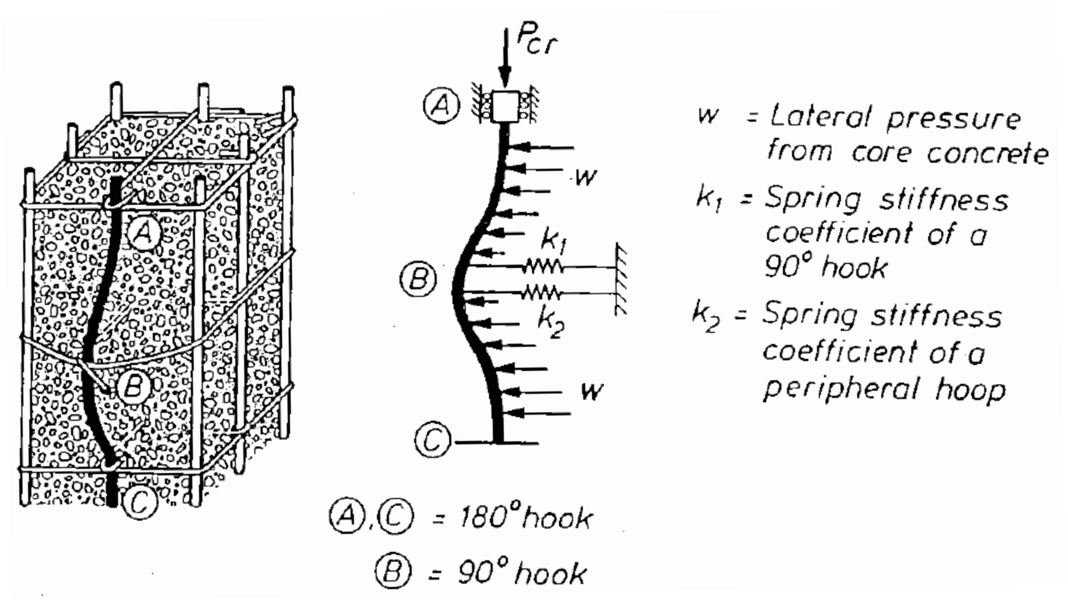

(a) (b)

Figure 2.10. Buckling of intermediate longitudinal bar restrained by cross ties with 90° and 135° or 180° (Tanaka, 1990): (a) Buckling mode; (b) Buckling model.

Papia et al. (1988) studied the critical load of longitudinal reinforcement considering a buckled bar could span multiple sets of hoops. They modeled the hoops as linear-elastic and used Bernoulli-Euler beam elements to represent the longitudinal reinforcement, see Figure 2.11a. The addition of appropriate boundary conditions, including a restriction for elements bending into the core concrete, complete the system of equations to determine the critical buckling load. Figure 2.11b shows the resulting critical load, P_c, normalized by the critical load of a hinged segment between consecutive hoops ($P_0=\pi^2 EI/s^2$), as a function of γ, the ratio between hoop stiffness, α, and shear stiffness of the longitudinal bars between hoops, EI/s^3. Results from the formulation consistently overestimated critical loads obtained experimentally, which was attributed to geometric and mechanical imperfections of the real specimens. Based on the average error between analytical and experimental results, Papia et al. suggested reducing the predicted critical load by a factor equal to $q=1.2$.

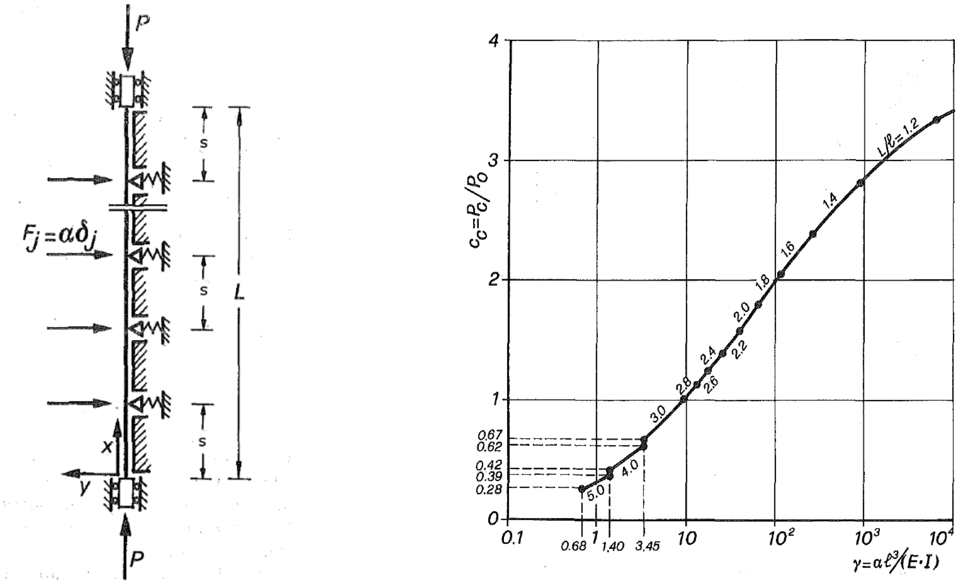

(a) **(b)**

Figure 2.11. Analysis model and critical load result diagram (Papia et al. 1988): (a) Mechanical model; (b) Normalized critical load vs γ parameter.

Although initial studies on the buckling of reinforcing steel focused on the critical load rather than the post-critical behavior, Mau and El-Mabsout (1989) carried out a series of parametric analyses using beam-column elements to predict the post-buckling stress-strain response of reinforcement at different slenderness levels, closely matching previous experimental results for reinforcement under monotonic load, see Figure 2.12.

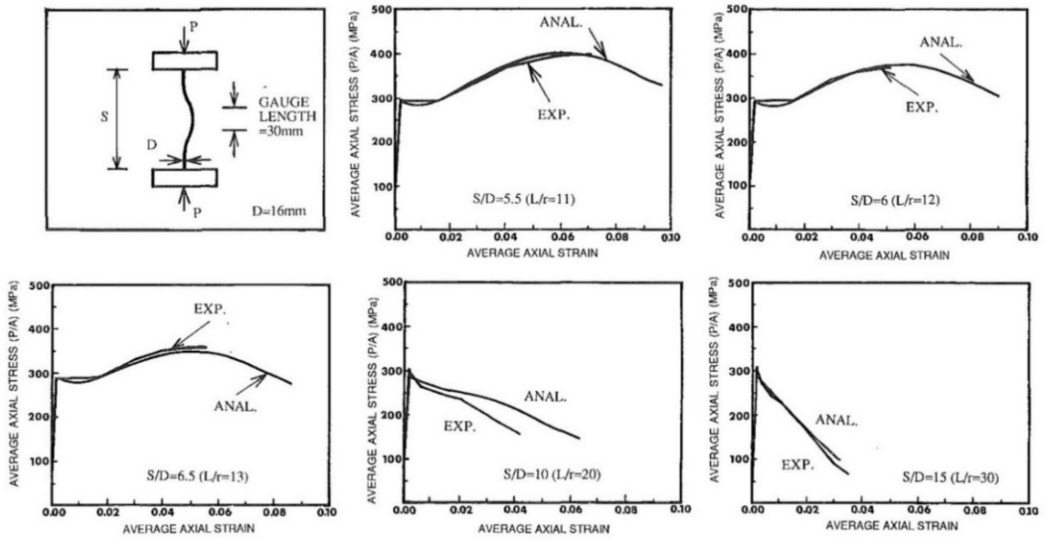

Figure 2.12. Comparison of experimental results and analytical results (Mau and El-Mabsout, 1989).

Monti and Nuti (1992) performed a series of monotonic and cyclic tests on FeB44 steel bars to investigate the effects of inelastic buckling. Aspect (slenderness) ratios of lateral support spacing to bar diameter (*s/d_b*) equal to 5, 8, and 11 were used for this purpose. Random, symmetrical, and non-symmetrical strain histories were used. They observe that, for monotonic behavior for bars with an aspect ratio of 5, the compressive monotonic curve essentially coincides with the tensile one. For an aspect ratio of 8, only a short superposition length (strain on the compressive curve diverges more than 5% from the tensile one towards lower values after yielding) is observed. For an aspect ratio of 11, as soon as the yield point is reached, buckling starts and the compressive monotonic curve departs from the tensile one. Based on these results, they created a simple, yet effective model for the cyclic response of steel including inelastic buckling, calibrated experimentally in terms of the slenderness ratio s/d_b. The model was tested under both symmetric and anti-symmetric strain histories, showing significant improvement in the fit of experimental results for $s/d_b > 5$, compared to typically used material models that do not include buckling, see Figure 2.13. Like the model by Menegotto and Pinto (1973) on which it is based, the formulation by Monti and Nuti (1992) overestimated the stress response following a partial unloading and reloading, this issue was later resolved by Fragiadakis et al. (2008), see Figure 2.14.

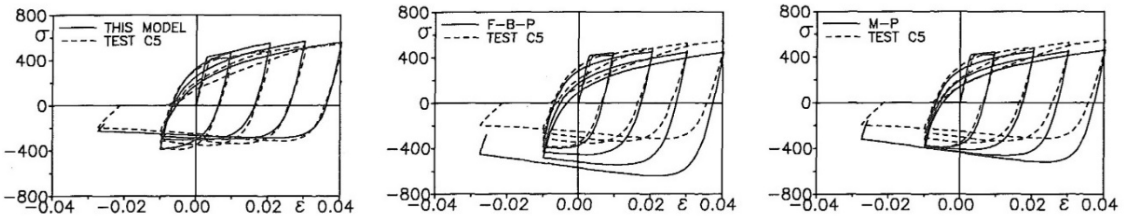

(a) **(b)** **(c)**

Figure 2.13. Comparison between experimental and analytical models for asymmetric strain history. $s / d_b = 11$ (Monti and Nuti, 1992): (a) Monti- Nuti; (b) Filippou-Bertero-Popov; (c) Menegotto and Pinto.

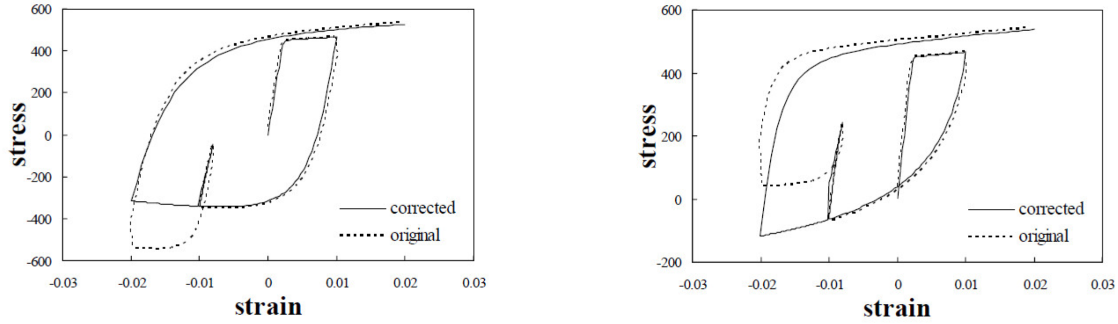

(a) **(b)**

Figure 2.14. Corrected and uncorrected stress-strain paths (Fragiadakis et al., 2008): (a) $s / d_b = 12$; (b) $s / d_b = 6$.

In order to include the effects of buckling in the cyclic stress-strain steel relationship, Gomes and Appleton (1997) presented a modification of the Menegotto-Pinto cyclic stress-strain steel model by combining the Menegotto-Pinto formulation and a lumped plasticity mechanism in the buckled reinforcement, see Figure 2.15. The model assumed the plastic model of the bar is not dependent on the axial force and that buckling concentrates between consecutive hoops. The main objective of the proposed model was to simulate the effect of buckling without heavy calculations, so the axial force and bending moment interaction were not taken into account. For this purpose, they employ a simple model of a buckled bar between two consecutive stirrups, see Figure 2.15. To compare results from the proposed model, they compare the numerical results with experimental results from the cyclic loading test of a reinforced concrete column. While good agreement was obtained, the main difference between the two was a pinching effect on the numerical results that was not observed in the experimental results.

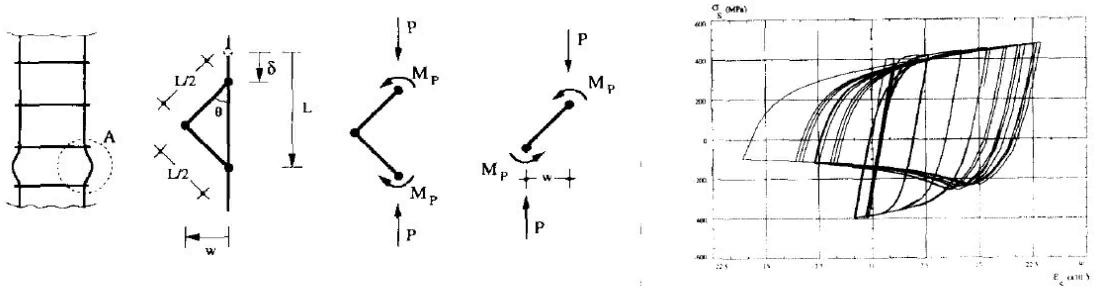

(a) (b)

Figure 2.15. Buckling model Gomes and Appleton (1995): (a) Equilibrium of buckled longitudinal bar; (b) Stress-strain response of the model.

Rodriguez et al. (1999) performed a series of monotonic and cyclic tests on steel reinforcing bars conforming to most of the ASTM A706 requirements with aspect ratios of

2.5, 4, 6, and 8. Based on moment-curvature analyses of typical column sections, values of 1 and 2.3 for the ratio $\varepsilon_m^+ / \varepsilon_m^-$ were used for the cyclic strain histories, were $\varepsilon_m^+, \varepsilon_m^-$ are the maximum tensile and compressive strains for a longitudinal reinforcing bar in a strain cycle. Axial strains, $\varepsilon_1, \varepsilon_2$,were measured using two extensometers supported at opposite sides of the test specimens. The onset of buckling for the cyclic tests was defined by using the strain readings $\varepsilon_1, \varepsilon_2$ and relating them to the peak strains reached in the corresponding cycle, $\varepsilon_m^+, \varepsilon_m^-$. This critical condition was reached when $\varepsilon_1 - \varepsilon_2$ was equal or greater than $0.2(\varepsilon_m^+ - \varepsilon_m^-)$. Based on these results and under the hypothesis that the envelope for the compressive cyclic stress-strain curves reasonably coincides with the monotonic curve, as described by Monti and Nuti (1992), they proposed a procedure for predicting the onset of buckling. The procedure uses the parameter ε_0^+, defined as the axial strain at zero loading after reversal from tension, see Figure 2.16. In addition, the parameter ε_p^*, is used for evaluating the axial strain at buckling, ε_p, and is defined as $\varepsilon_p^* = \varepsilon_0^+ - \varepsilon_p$. Rodriguez et al. suggest that the onset of buckling in a reinforcing bar under hysteresis cycles occurs after a reversal from tension and is strongly dependent on the maximum tensile strain reached before that reversal.

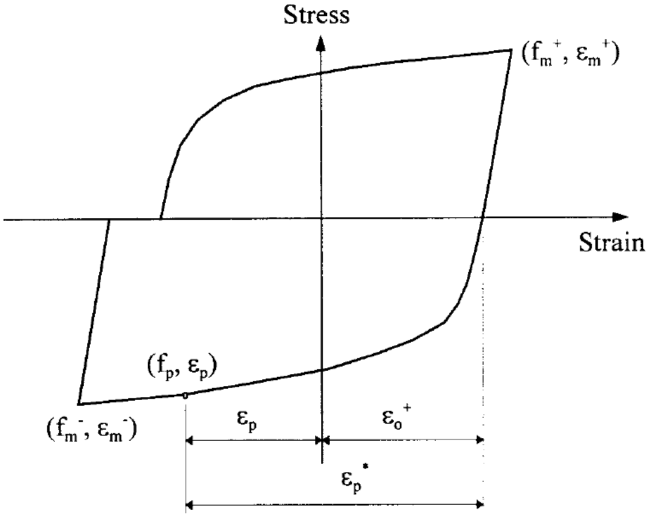

Figure 2.16. Cyclic stress-strain curve for steel (Rodriguez et al., 1999).

El-Bahy et al. (1999) tested six reinforced concrete circular bridge piers under monotonic and cyclic loading to obtain their relevant force-deformation and “low-cycle” fatigue characteristics. Constant amplitude cycles of displacement amplitudes ranging from a corresponding 2 percent lateral drift up 7 percent were used. The authors conclude that, under sequences of predominantly low amplitude cycles, a confinement failure is more probable, while for predominantly high amplitude inelastic cycles, buckling and “low-cycle” fatigue fracture of the longitudinal reinforcement is more likely.

Bayrak and Sheikh (2001) studied the effect of buckling in the longitudinal reinforcement at the section level, developing a procedure to estimate the monotonic moment-curvature response in the plastic hinge of a RC column. The procedure relies on experimental results for the lateral load due to core concrete expansion, and the stress-strain response of longitudinal reinforcement between hoops (in between hoops, the bond between concrete and steel is lost after the onset of buckling). For this purpose, Bayrak and

Sheikh tested 56 #6 steel specimens at multiple slenderness ratios (from $s/d_b=4$ to $s/d_b=10$) and initial imperfection ratios (from $e/d_b=0$ to $e/d_b=0.3$, with e the initial lateral deformation of the reinforcement) under monotonic load. The moment-curvature results from this procedure showed a better fit to experimental data compared to conventional section analyses, Figure 2.17.

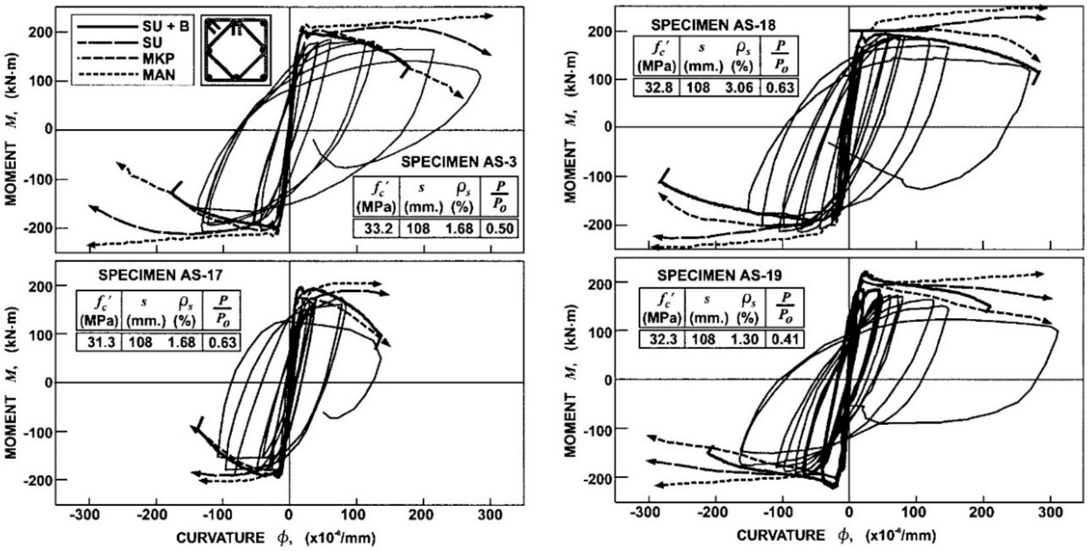

Figure 2.17. Experimental and predicted moment-curvature response. SU: Sheikh and Uzumeri; MKP: Kent and Park; MAN: Mander; SU+B: Bayrak and Sheikh (2001).

Dhakal and Maekawa (2002) ran several finite element simulations of the buckling response of bare reinforcing bars (without core concrete or transverse reinforcement interaction). Through a parametric study, they found the product $s/d_b \cdot \sqrt{f_y}$ (f_y: yield stress), can accurately define the post-buckling behavior of the material, not just the slenderness ratio s/d_b (Monti and Nuti 1992). A model for the monotonic post-buckling response was suggested, see Figure 2.18, which could be used as an envelope for the

Menegotto and Pinto (1973) cyclic model. The model was tested against experimental response originally recorded by Monti and Nuti, see Figure 2.19. Kunnath et al. (2009) implemented a material model including the effects of buckling, low-cycle fatigue and cyclic degradation; using the formulation by Dhakal and Maekawa for the buckling effect. The material model is currently implemented in OpenSees as *ReinforcingSteel*.

Moyer and Kowalsky (2003) showed experimentally how the buckling of reinforcement is dependent on the level of tensile strains the bars are initially subjected to, an observation first made by Wang and Restrepo (1996) in their work on columns confined with fiberglass/epoxy jackets, see Figure 2.20. The relationship can be explained as follows: for a longitudinal bar to buckle, a large tensile strain is first required to open the cracks in the surrounding concrete; at the following loading reversal, the reinforcing bar represents the sole source of compression capacity until the cracks close, if the critical load is reached before then, the bar will start to buckle.

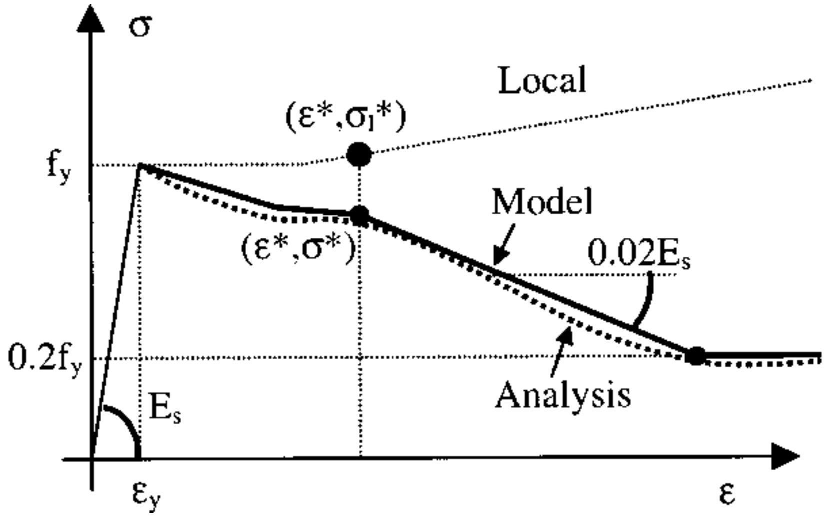

Figure 2.18. Proposed model by Dhakal and Maekawa (2002).

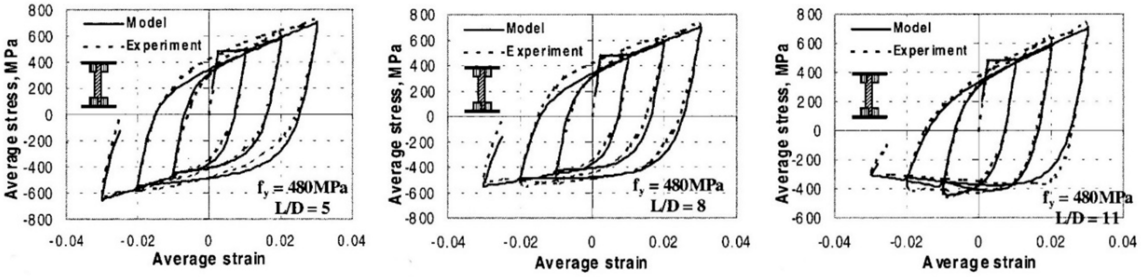

Figure 2.19. Comparison of analytical and experimental hysteretic response (Dhakal and Maekawa, 2002).

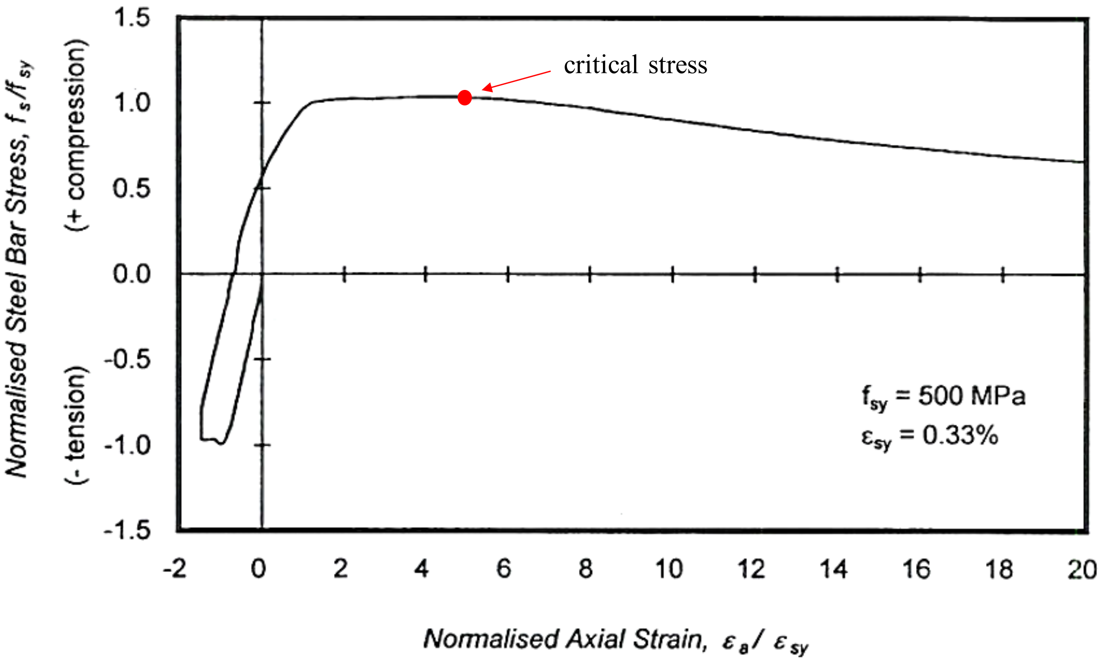

Figure 2.20. Inelastic buckling behavior of Grade 430 deformed reinforcing bar with aspect ratio $s/d_b=9$ (Wang and Restrepo, 1996).

Bae et al. (2005) tested 162 bars #8 and #10 bars under monotonic load for multiple combinations of slenderness ratio and initial lateral imperfection ratio. Using the experimental results to model the relationship between axial stress, lateral displacement, and axial strain, a simple monotonic material model, suitable for fiber discretization models, was developed and tested against experimental data with satisfactory results, as seen in Figure 2.21.

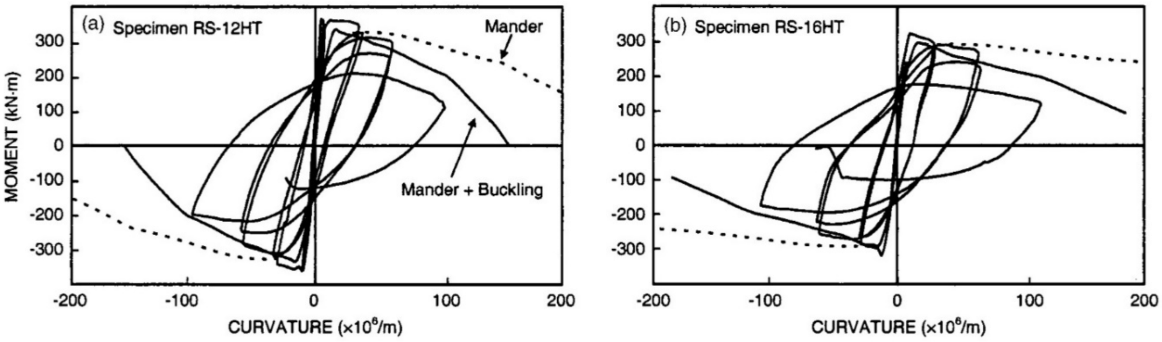

Figure 2.21. Experimental and predicted moment-curvature response (Bae et al., 2005).

Berry and Eberhard (2005) proposed a procedure for earthquake engineering practice to estimate the lateral deformation at which a RC column reaches the onset of buckling, which represents an important performance state of the system. The method combines experimental formulations for the yield displacement (Priestley 2003), see Equation 2-7, plastic hinge length (Mattock 1967), see Equation 2-8, strain of steel at onset of buckling (see Equation 2-9), and plastic curvature (Berry 2003), see Equation 2-10. The resulting equation for the lateral depends on five constants, Equation 2-11, which were calibrated from a database of experiment results for 104 columns tested under cyclic load.

$$\Delta_y \cong \frac{f_y L^2}{3} = \frac{\lambda}{3 \cdot E_s} f_y \frac{L^2}{D}$$ **Equation 2-7**

Where Δ_y is the lateral displacement at yield, f_y and E_s the yield stress and Young's modulus of the longitudinal reinforcement, L and D the length and diameter of the column, and λ a factor dependent on the type of transverse reinforcement (e.g. $\lambda = 2.45$ for spiral reinforcement).

$$L_p=\alpha \cdot L+\beta \cdot D+\xi \cdot f_y \cdot d_b$$

Equation 2-8

With d_b the bar diameter of tension reinforcement, and α, β, and ξ linear factors to be estimated from experimental results.

$$\varepsilon_{bb}=\chi_0 \cdot (1+\chi_1 \cdot \rho_{eff})$$

Equation 2-9

ε_{bb} is the buckling strain, $\rho_{eff}=\rho_s f_{ys}/f_c^{'}$ with ρ_s the volumetric transverse ratio, f_{ys} the yield stress of transverse reinforcement, and $f_c^{'}$ the concrete compressive strength. χ_0 and χ_1 are constants to be determined.

$$\phi_{p\text{-}bb} \cong \frac{\eta_0}{D}\left(\frac{1+\eta_1\rho_{eff}}{1+\eta_2\frac{P}{A_g f_c^{'}}}\right)$$

Equation 2-10

With η_0, η_1, and η_2 constants.

$$\frac{\Delta_{bb}}{\Delta_y}=1+\frac{3E_s}{\lambda f_y}C_0(1+C_1\rho_{eff})\left(1+C_2\frac{P}{A_g f_c^{'}}\right)^{-1}\times\left(\frac{D}{L}+C_3+C_4\frac{D}{L}\frac{f_y d_b}{D}\right)$$

Equation 2-11

Where Δ_{bb} is the predicted lateral displacement at the onset of bar buckling and C_0 through C_4 are calibrated constants.

From the calibration analysis, Berry and Eberhard (2005) proposed the following equation,

$$\frac{\Delta_{bb\text{-}calc}}{\mathrm{L}}(\%)=3.25\left(1+k_{e\text{-}bb}\rho_{eff}\frac{d_b}{D}\right)\left(1-\frac{P}{A_g f_c^{'}}\right)\left(1+\frac{L}{10D}\right)$$

Equation 2-12

With $k_{e\text{-}bb} = 40$ for rectangular-reinforced column, 150 for spiral-reinforced column, and 0.0 when $s/d_b > 6$. The ratio between experimental and predicted results for Δ_{bb} resulted in a mean of 1.0 and standard deviation of 25%.

Cosenza and Prota (2006) performed extensive experimental work on the monotonic response of smooth steel bars under a wide range of slenderness ratios, from $s/d_b=5$ to $s/d_b=70$. They defined threshold values of s/d_b for the type of response to be expected: from plastic behavior without buckling for $s/d_b<5$, to elastic buckling for $s/d_b>20$. Smooth reinforcement and large slenderness ratios are representative of the typical reinforcement in RC structures built in the 1960s. This work was expanded by Prota et al. (2009) with the study of the cyclic response of smooth bars under multiple slenderness ratios. The study found the cyclic behavior to be heavily influenced by the loading history (in particular, the maximum plastic elongation and hysteretic energy dissipated) besides s/d_b. The study also found that most material models available could not capture the response of specimens with $s/d_b > 8$.

Massone and Moroder (2009) proposed a plastic model based on early unpublished work by Restrepo (2007). In it, an initial imperfection is introduced to the reinforcement and the deformations concentrate in four plastic hinge locations along the buckled bar, see Figure 2.22.

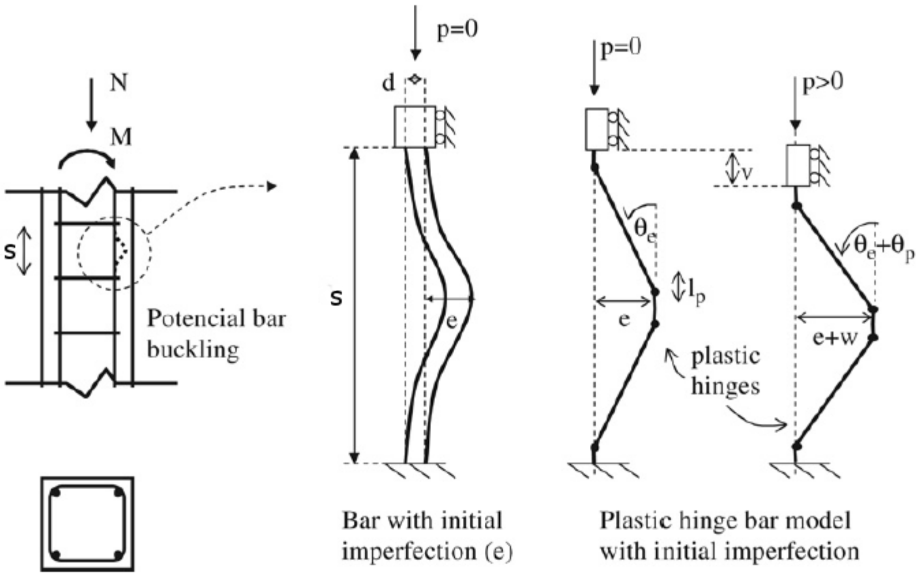

Figure 2.22. Mechanical model for bar buckling (Massone and Moroder, 2009).

Zong et al.(2013) defined a post-buckling envelope curve similar to the formulation by Dhakal and Maekawa (2002), calibrating the model using simulation results from the finite element software LS-DYNA. The interaction with transverse reinforcement was included using the bar-with-spring model developed by Zong (2010).

Feng et al. (2014) proposed a two-step numerical method to predict the occurrence of longitudinal bar buckling under seismic load. First, a fiber-based finite element model is used to obtain the response of the full structural element under seismic excitation. The resulting strain history in the plastic hinge zone is used as input in a second finite element model, developed in the software Abaqus, which includes the interaction with the concrete core and transverse reinforcement, see Figure 2.23. This procedure accurately predicted the observed onset of buckling of three experimental tests.

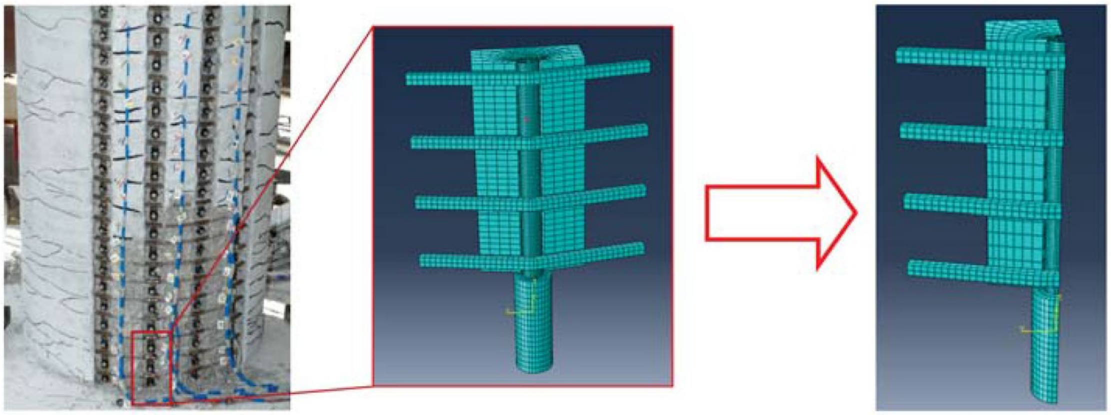

Figure 2.23. Geometry of the plastic hinge zone model in Abaqus (Feng et al., 2014).

Yang et al. (2016) developed a modified version of the Gomes-Appleton model using four plastic hinge locations, improving the prediction of the original model, especially for small slenderness ratios (s/d_b).

Analytical models of the post-buckling behavior can be divided into three main categories: beam-column elements, material models, and geometric formulations. Beam-Column element models rely on Bernoulli-Euler beam theory to analyze the post-buckling behavior. Initial work by Mau and El-Mabsout (1989), Nonaka (1973), Papadrakakis and Loukakis (1988), among others, assumed fixed ends of the reinforcements at the transverse ties.

Material models account for the nonlinear response through various simplifications, calibrating their formulation using computer simulations (e.g. Dhakal and Maekawa, 2002) or experimental results (e.g. Monti and Nuti,1992).

Geometric models address the non-linear geometric compatibility directly, using finite element analysis or a plastic mechanism model. The finite element model approach has been investigated by several authors (e.g. Nakamura and Higai (2002), and Feng et.al

(2014)). The accuracy of the results from this method are, however, at the expense of high computational requirements, making them unpractical for the modeling of full-scale elements.

Plastic mechanism models are based on concentrated plasticity theory, such as the work by Engesser- Considère, von Karman, and Shanley. The simplified models by Gomes and Appleton (1995), and Papadrakakis and Loukakis (1988), also incorporate concentrated plasticity in their formulation.

The experimental efforts of several authors (Bayrak and Sheikh(2001), Bae et al. (2005), Cosenza and Prota (2006)) have enabled the development of a comprehensive database, available for the verification of analytical models of buckling, although results for large diameter reinforcement under cyclic loading are still scarce.

Significant progress has been made over the years in the understanding and prediction of buckling of reinforcement in the plastic hinge zone of RC columns. However, an accurate and efficient formulation of this effect, capable of integrating this phenomenon in simulations of large-scale models, has yet to be developed. Currently, efficient buckling formulations, available for fiber-based finite element models, assume for simplicity that the transverse reinforcement constrains lateral deformations between adjacent hoops, despite experimental results showing otherwise. More accurate material models, which include the interaction between longitudinal, transverse reinforcement and the core concrete, have computational requirements that make them unsuitable for the modeling of large-scale systems. The development of a material model for steel including buckling that is both computationally efficient and considers the interaction with transverse reinforcement and core concrete, which is the purpose of the current study, is a significant contribution for the performance-based design and analysis of structural systems under seismic input.

Kashani et al. (2015a) did a comprehensive experimental testing on ninety reinforcing bars under “low-cycle” fatigue strain history with various slenderness ratios, diameters, yield strengths and surface roughness (deformed and smooth bars). The deformed reinforcing bars were B500B and B460 for the smooth bars. Slenderness ratios of 5, 8, 10, 12, and 15 were used with strain amplitudes ranging from 1-5% for 12 mm bars and 1-4% for 16 mm bars. Their work shows that crack initiation due to fatigue testing occurs earlier for bars with larger aspect ratios and that cracks start at the concave face of the buckled bars. They also suggest that, when a bar buckles, the total strain amplitude at the concave face of the bar increases due to combined axial and bending deformation. Once formed, fatigue cracks propagate away from the transverse rib into the body of the bar normal to the bar axis, suggesting that the largest stresses lie in the longitudinal direction of the bar. A reduction in “low-cycle” fatigue life was noted for larger diameter bars. Kashani et al. (2015b) studied the combined effect of corroded reinforcement and inelastic buckling on “low-cycle” fatigue life of reinforcing bars. Results showed that inelastic buckling has a significant impact on the cyclic stress-strain response, with a quicker cyclic degradation for bars with larger aspect ratios. Also, while the stress-strain response of uncorroded bars with $s/d_b = 5$ was symmetrical in tension and compression, inelastic buckling could be observed on corroded bars with the same aspect ratio. The authors describe strain amplitude as the most important parameter affecting the “low-cycle" fatigue of reinforcing bars, with an increasing influence for bars with larger s/d_b ratios. Kashani (2017) explored the influence of bar diameter on inelastic buckling behavior of uncorroded and corroded reinforcing steel bars. The tested bars had a 10, 12, 16, and 20 mm diameter with aspect ratios ranging from 5-20. The experimental work showed that bar diameter influences the postyield buckling response of reinforcing bars with $s/d_b \leq 8$, but as the aspect ratio increases, such influence decreases. Nojavan et al. (2017) tested RC column specimens under monotonic or progressively increasing displacement reversals until the columns lost more than 80% of their lateral loading capacity. Contrary to common assumptions, it was observed that some of the bars buckled parallel to the compression face of the columns and in many of the buckled bars, in-plane buckling occurred about the strong axis of bending of the bars. Unlike longitudinal bar spacing, the influence of longitudinal bar size on the in-plane bar buckling was described as significant, with bar sizes (No. 8 and above) more likely to experience in-plane buckling due to their higher restraint demands. Qiu et al. (2018) tested 20-mm diameter reinforcing steel bars under monotonic tension and compression. They show that, before the yield strain, most of the average axial strain is due to the axial shortening of the bar. However, after yielding, the buckling effect dominates the behavior of the bar. They conclude that bars with larger s/d_b ratios are more affected by buckling. On the effect of yield strength, the authors suggest that the post-buckling average stress degrades faster with an increase of yield strength and that the bearing capacity of the bars in the post-buckling range increases with the increase of T/Y ratio. Tripathi et al. (2018) performed monotonic uniaxial tension and "low-cycle" fatigue tests with different slenderness ratios on 12 mm un-machined bars.

They conclude that "low-cycle" fatigue life of reinforcing bars is a function of the strain amplitude, yield strength, and slenderness ratio. Furthermore, in addition to adversely affecting the fatigue life of the reinforcing bars, buckling was shown to influence the overall hysteresis behavior of the test bars. Once buckled, a substantial drop in the peak stresses attained by a bar in the first cycle was noted in the subsequent cycles. While mean strain ratio had some effect on the fatigue life or the reinforcing bars, no sustained trend could be observed. Kashani et al. (2019) discussed the influence of bar diameter and s/d_b on the "low-cycle" fatigue life of steel reinforcement. They note that the influence of bar diameter reduces with increasing s/d_b ratios due to the influence of plasticity on the hysteretic response. As s/d_b increases, the geometrical nonlinearity governs the global response. Also, results indicated some influence of bar diameter on the fracture mechanism of the bars. However, once bars buckled and due to a faster crack growth from localized strain amplitude, the bar diameter did not significantly influence the performance of the bars.

2.3. Fatigue Life of Reinforcing Bars

The fatigue phenomenon is of great importance to the response of reinforce concrete (RC) members when subjected to large deflections during an earthquake. While numerous studies have focused on studying and characterizing such phenomenon, there is very limited data on the fatigue characterization of large-diameter steel bars. The purpose of this section is to briefly cover the fundamental concepts of fatigue and the various methods used to characterize the fatigue life of steel reinforcement.

Fatigue can be defined as a degradation of mechanical properties leading to failure under cyclic loading (Meyers and Chawla 2009). From mechanics of materials, the two principal methods for material deformation and failure are crack growth and dislocations as well as plastic flow. As high stress concentrations occur at the tip of cracks, the mechanism of fracture can involve plastic deformation at such locations. A material which allows for such plastic deformations to take place at the cracks is "tough", otherwise, the material is "brittle". Deformation processing, such as rolling, forging, and extrusion involve substantial plastic deformation and the response of the material will depend on its plastic behavior during such processes. The material properties of steel are also highly affected by heat treatment. Quenching produces a hard, martensitic structure, which is gradually softened by tempering treatments at higher temperatures. On the other hand, the annealed structure is ductile, but results in a low yield stress.

2.3.1 Plastic Deformation in Tension and Compression

The response of mild steel loaded in tension is well known, with a very characteristic stress-strain curve up to fracture. It is usually characterized by four regions: (1) The linear elastic region, (2) the Lüders strain or yield plateau, (3) the strain-hardening region, and (4) the post-ultimate stress region, as shown in Figure 2.24 (Dodd and Restrepo-Posada 1995).

The slope of the linear elastic region is known as Young's modulus or elastic modulus E_s. The modulus is mainly dependent on the composition, crystallographic structure, and nature of the bonding of elements. Heat and mechanical treatments have little effect on Young's modulus, hence annealed or cold-rolled steels should have the same modulus of elasticity(Meyers and Chawla 2009). The linear stress-stress relationship in this region is described as:

$$f_s=E_s\cdot\varepsilon_s$$

Equation 2-13

where f_s and ε_s are the steel engineering stress and strain, respectively.

While the yield plateau is typically assumed to be horizontal, Figure 2.24 shows that this is not the case. Instead, the yield stress, f_y, should be taken as the average value of the plateau. The yield strain, ε_y, can therefore be obtained by:

$$\varepsilon_y=f_y/E_s$$

Equation 2-14

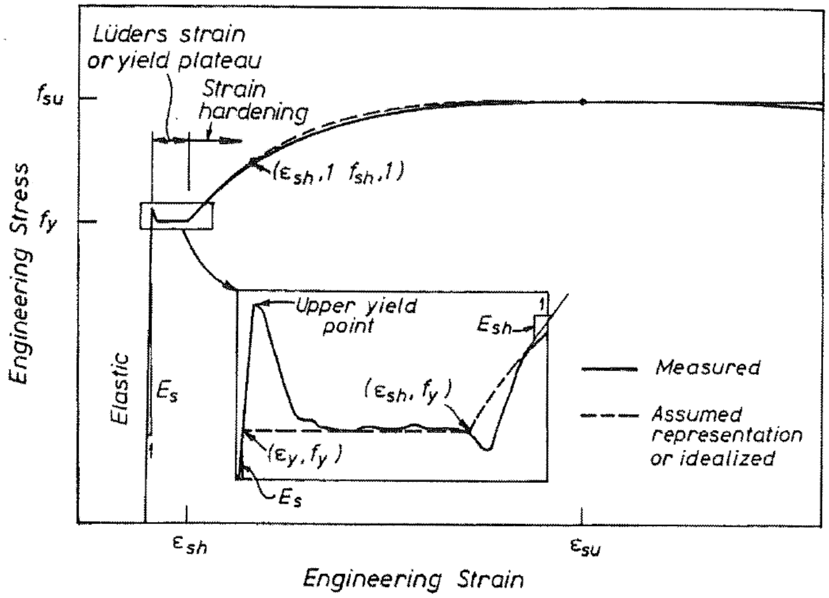

Figure 2.24. Monotonic tensile curve for mild steel (Restrepo-Posada, 1993).

Before the relatively smooth strain-hardening region begins, a dip in the yield plateau is typically observed, followed by a sharp increase that changes slope. The strain-hardening region hence ranges from the idealized coordinates at which strain-hardening begins, $(\varepsilon_{sh,}f_y)$, to the coordinates at which the maximum tensile load is resisted and necking begins, $(\varepsilon_{su,}f_{su})$. The slope at this point is zero in engineering coordinates.

In the post-ultimate stress region, the shape of the tensile stress-strain curve is dependent on the location and gauge length over which data is collected. Therefore, it is typically assumed that the ultimate coordinates mark the end of the useful region of stress-strain curve. Furthermore, once necking begins, the engineering stresses drop due to the localized reduction in cross sectional area. Engineering stress, σ, and engineering strain, ε, are defined as:

$$\sigma = N / A_0 \;\; ; \;\; \varepsilon = \frac{1}{l_0}\int_{l_0}^{l} dl = \frac{l - l_0}{l_0} = \frac{\Delta l}{l_0}$$

Equation 2-15

where l_o=initial length of element, l = instantaneous length of element, Δl = change in length of the element from its initial length; N = axial force acting on the element; and A_o = initial cross-sectional area of the element.

However, the natural stresses continue to rise because of the reduction in cross-sectional area and the work hardening at the necking region. Natural stress, σ', and natural strain, ε', are defined as:

$$\sigma' = N / A \;\; ; \;\; \varepsilon = \int_{l_0}^{l} \frac{dl}{l} = ln\left(\frac{l}{l_0}\right)$$

Equation 2-16

where A = instantaneous cross-sectional area.

By assuming a constant volume, V, during plastic deformation, the natural-stress-natural-strain curves can be obtained from the engineering stress-engineering-strain curve as follows:

$$V = A_0 \cdot l_0 = A \cdot l$$

Equation 2-17

$$\varepsilon = \frac{l - l_0}{l_0} = \frac{A_0}{A} - 1$$

Equation 2-18

$$\frac{\sigma'}{\sigma} = \frac{N}{A} \cdot \frac{A_0}{N} = \frac{A_0}{A} = 1 + \varepsilon$$

Equation 2-19

$$\sigma' = (1 + \varepsilon) \cdot \sigma$$

Equation 2-20

$$\varepsilon' = \ln (1 + \varepsilon)$$

Equation 2-21

For isotropic materials, such as steel, the greatest advantage of the natural coordinate system (ε', σ') is the symmetry between tension and compression curves (Dodd and Restrepo-Posada 1995).

2.3.2 Fatigue Process

As previously mentioned, fatigue can be defined as a degradation of mechanical properties leading to failure of a material under cyclic loading. Typically, the failure under cyclic loading occurs at much lower stress levels that the strength under monotonic loading. The study of cyclic behavior can be divided into three classes: the stress-life approach, the strain-life approach, and the fracture mechanics approach.

The stress-life approach is useful when stresses and strains mainly remain in the elastic range. The main drawback of this approach is the inability to distinguish between the initiation and propagation phases of fatigue life. For elasto-plastic materials, such as reinforcing steel, this approach is used when dealing with high-cycle fatigue (1,000 cycles or more to failure) The strain-life approach is useful when there is a significant amount of plastic strain and will be the basis for the ongoing research. The fatigue life is typically quite short under these conditions and is referred to as low-cycle fatigue (less than 1,000 cycles to failure). In the fracture mechanics approach, the basic ideas of fracture mechanics are applied to cyclic fatigue. The approach estimates the life spent in propagating a crack from an initial to a larger size or to the critical size corresponding to failure.

The first step in the fatigue process in most materials corresponds to crack nucleation at singularities or discontinuities. Discontinuities may be on the surface or in the interior of the material. The singularities can be structural (such as inclusions or second-phase particles) or geometrical (such as scratches or steps). The explanation of preferential nucleation of fatigue cracks at surfaces perhaps resides in the fact that plastic deformation is easier there and that slip steps form on the surface (Meyers and Chawla 2009). While slip steps alone can be responsible for initiating cracks, they can also interact with existing structural or geometric defects to produce cracks. In metals, surface singularities may be present from the beginning or may develop during cyclic deformation, such as the formation of intrusions and extrusions at what are called the persistent slip bands (PSBs). Figure 2.25 illustrates the fatigue crack nucleation at slip bands. As loading takes place, slip occurs on a favorably oriented plane, and during unloading, reverse slip occurs on a parallel plane, since slip of the original plane is inhibited due to hardening or due to the oxidation of the newly formed free surface. The first cyclic slip may create an extrusion or an intrusion at the surface. An intrusion may grow and form a crack by continued plastic deformation during subsequent cycles. At large stress or strain amplitudes, as much as 90% of a material's fatigue life is consumed in the growth or propagation of a crack.

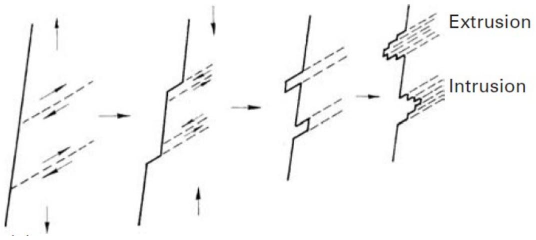

Figure 2.25. Fatigue crack nucleation (Meyers and Chawla, 2010).

2.3.3 Effects of Bar Geometry and Material Properties

Burton (1965) studied the influence of the condition of rolls at the time of manufacture on the fatigue characteristics of reinforcing bars, see Figure 2.26. The three major variables investigated were the position of the longitudinal ribs, the deformations produced by known conditions of the rolls at the time of manufacture, and stress range. High-cycle fatigue tests were performed on RC beams reinforced by a single No. 8 bar conforming to ASTM A-15 and ASTM A-305. Burton concluded that the condition of the rolls only had a minor influence on the fatigue life of the bar. The orientation of the longitudinal ribs relative to the plane of bending had a pronounced effect, with a reduced fatigue life when the longitudinal ribs were parallel to the plane of bending. This, as the author point out, is something that can only be controlled in a laboratory environment and not in construction. Stress range had the most influence on the fatigue life of the bars, with negative relation between fatigue life and stress range.

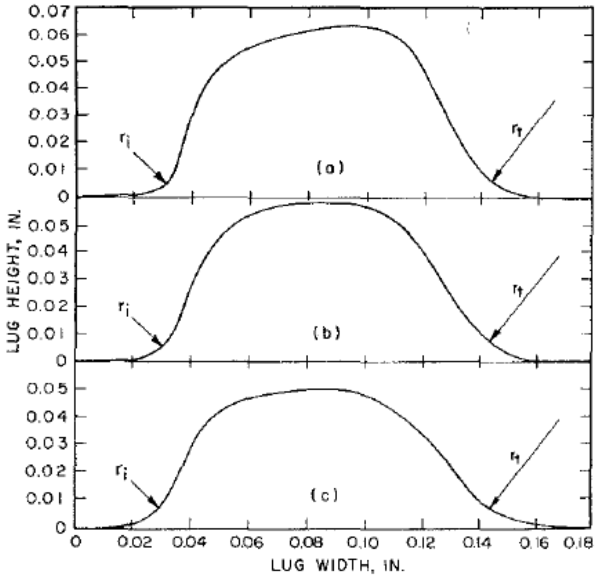

Figure 2.26. Typical profiles of deformations produced by: (a) New rolls; (b) Partially worn rolls; (c) Fully worn rolls (Burton, 1965).

Hanson et al. (1968) performed a series of fatigue tests on No. 8 bar embedded in rectangular concrete beams. Half of the specimens were American-made bars (Series I) with crescent-shape lugs that did not merge into the longitudinal ribs and which had small manufacturer marks, relative to the lug size. See Figure 2.27a. The other half were European-made cold-twisted bars (Series II) with inclined parallel lugs that also did not merge into the longitudinal ribs and did not have manufacturer marks. See Figure 2.27b. They suggest that the radii at the base of the lugs should be approximately equal to the height of the lugs to obtain good fatigue characteristics. An increase in lug radius at the base increases the fatigue strength of steel reinforcement. They also conclude that the fatigue strength of the bars is not necessarily improved by terminating the transverse lugs before they reach the longitudinal ribs. All fatigue cracks for Series I bars started at the base of the lugs and had a fracture surface orthogonal to the axis of the bar. All fatigue cracks for Series II bars started adjacent to the sharp side of a lug and had a 45-degree fracture surface plane relative to the axis of the bar.

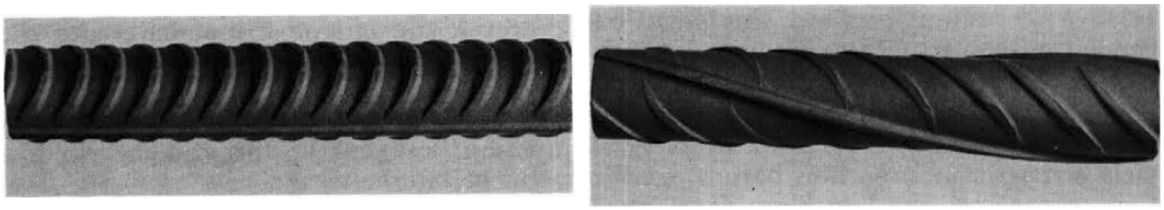

(a) (b)

Figure 2.27. (a) American-made bars; (b) European-made bars (Hanson et al., 1968).

Kokubu and Okamura (1969) performed a series of high-cycle fatigue tests on RC beams using different types of high-strength hot-rolled #6 and #8 deformed bars. They conclude that the most influential factor governing the high-cycle fatigue of deformed bars is the degree of change in slope at the base of the lug given that lug bases constitute weak points due to stress concentrations. Hence, reduced changes in slope would also reduce the degree of stress concentration and greatly increase fatigue life. However, they note that if arcs with radii of 5 or more times the height of the lugs are used, bonding between the bar and concrete is impaired. To reduce this effect, they suggest abruptly changing the slope of a lug at a point about one-third up the lug such that the upper half will be vertically.

MacGregor et al. (1971) carried out high-cycle fatigue tests on RC beams reinforced with a single #5, #8, or #10 bar. Such bars had two longitudinal ribs, parallel transverse lugs inclined at about 75 degrees to the bar axis, and all lugs merged into the longitudinal ribs. They conclude that, for design purposes, the fatigue strength of hot-rolled deformed reinforcing bars is not affected by changes in the tensile strength of the bars. They also note a small decrease in the fatigue strength with an increase in the diameter of the bar.

Hanson et al. (1974) performed a comprehensive experimental investigation on the influence stress range, bar size, and ASTM grade (among other factors) have on the fatigue life of reinforcing bars. Fatigue tests were performed on RC T-beams reinforced by a single deformed bar at different effective depths. No. 5, 6, 8, 10, and 11 bars of Grade 40, Grade 60, and Grade 75 were used. Results indicated a general decrease in fatigue resistance with increasing bar size. Fracture surfaces associated with the fatigue crack were crescent shaped, while the remainder of the fracture surface had a rough, crystalline appearance. All fatigue fractures originated at the base of a lug, with the exception of five out of 236 specimens, where the fracture originated at the base of the manufacture's identification mark. Stress range was noted as the predominant variable affecting fatigue strength of the bars.

Jhamb and Mac Gregor (1974a) studied the influence of deformations, surface decarburization, and grade of steel on the fatigue life of hot-rolled reinforcing bars. ASTM A615 Grade 40 and Grade 60 No. 8 bars were used in the experimental work. Deformed bars, plain rolled bars, and machined bars were tested. All fatigue failures originated at the base of the transverse lugs; however, failure was noted to have been caused due to nucleation of several cracks at the lug base rather than from a single crack. Fatigue strength of deformed reinforcing bars was noted as insensitive to the steel grade. Bar deformations, decarburization, and surface roughness were noted as having a detrimental influence on the fatigue life of the bars.

Jhamb and Mac Gregor (1974b) performed a series of finite element analyses to determine the effect of stress concentration factors, K_T, on the fatigue life of deformed reinforcing bars. K_T is defined as the ratio of the maximum elastic stress in a region of a notch, to the nominal stress in the member. The authors suggest that the ratio of the lug base radius to the lug height (*r*/*h*), had the most influence on K_T. See Figure 2.28. From the experimental work, they concluded that the stresses at the base of the lugs were higher in the direction of the bar than at the same location, but perpendicular to the transverse lug, while stresses at the intersection of the longitudinal and transverse ribs were not as critical. The authors argue that by limiting the *r/h* ratio to 1.25 and specifying a maximum width to height ratio (*w/h*), specifications for higher fatigue strength could be developed.

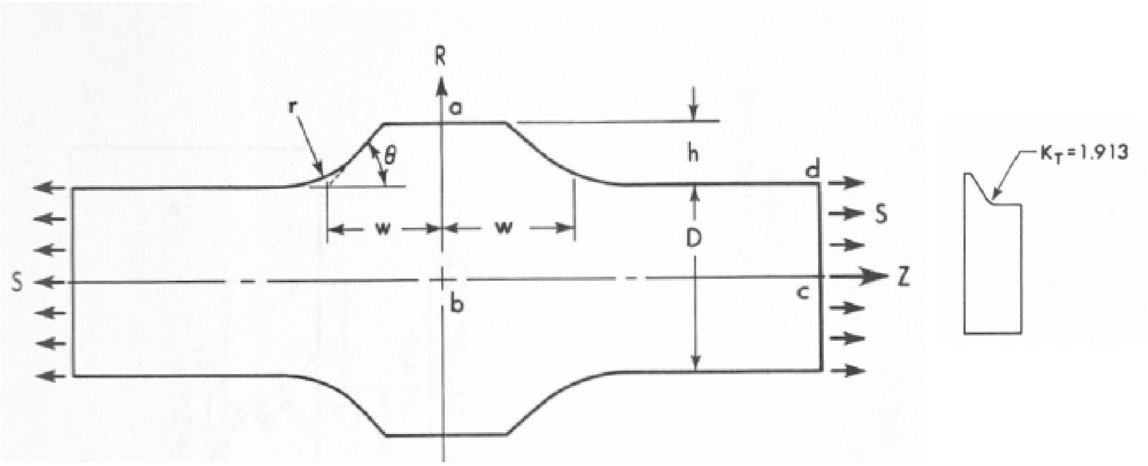

Figure 2.28. Lug modeling (Jhamb and Mac Gregor, 1974).

Helgason et al. (1976) also concluded that bar diameter, grade of bar, and bar geometry all play a role on the fatigue life of reinforcing bars. Larger-sized bars were noted as having a lower fatigue strength, while higher-grade bars had an increased fatigue strength. Noteworthy was the coupled effect bar diameter and lug geometry had on fatigue life, with lug geometry having a greater effect on larger diameter bars. However, the stress range to which a reinforcing bar is subjected was determined as the primary factor to determine the fatigue life of a bar. The role of bar surface deformations in creating stress concentrations was also pointed out by the authors, with all fatigue cracks observed to have been initiated at the base of a transverse lug or, in a few cases, at the base of a manufacturer's bar identification marks. Fracture surfaces were noted as dull with a rubbed appearance surrounded by a crescent-shaped zone with a rough crystalline surface. See Figure 2.29.

Figure 2.29. Test bar fracture surface (Helgason et al., 1976).

ACI Committee 215 (1992) compares data from three different investigations examining the effect of bar size and tabulates results relative to the fatigue strength of a No. 8 bar. See Figure 2.30. A negative relationship between bar size and fatigue strength can be observed. On the effects of deformation geometry, the Committee notes that tests indicate that by increasing the *r/h* ratio to between 1 and 2, the fatigue strength of the bars is increased. A ratio larger than 2, they note, does not show much effect on the fatigue strength of the bar.

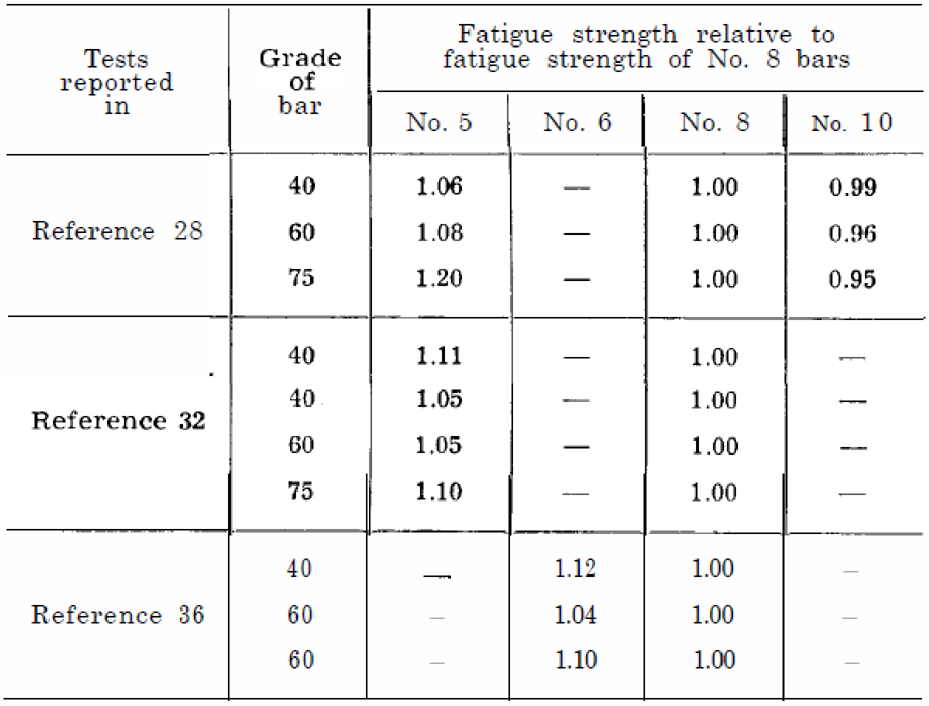

Tests reported in	Grade of bar	Fatigue strength relative to fatigue strength of No. 8 bars			
		No. 5	No. 6	No. 8	No. 10
Reference 28	40	1.06	—	1.00	0.99
	60	1.08	—	1.00	0.96
	75	1.20	—	1.00	0.95
Reference 32	40	1.11	—	1.00	—
	40	1.05	—	1.00	—
	60	1.05	—	1.00	—
	75	1.10	—	1.00	—
Reference 36	40	—	1.12	1.00	—
	60	—	1.04	1.00	—
	60	—	1.10	1.00	—

Figure 2.30. Effect of bar size (ACI Committee 215, 1992)

Restrepo-Posada (1993) tested 24 mm and 40mm diameter, Grade 430 and Grade 300, deformed reinforcing steel bars and found that “low-cycle” fatigue in reinforcing bars results in the development and progression of cracks at the root of bar deformations. Large shear strain concentrations, developed after the onset of bar buckling, result in a rearrangement of the steel microstructure, and micro-cracks, initially invisible to the naked eye, start to propagate and lead to bar fracture. Figure 2.1 shows an electron-microscope photograph where incipient cracks in the micro-structure of the steel are observed at the root of a deformation on the concave side of the buckled bar. The effects of bar deformations were studied by Fei and Darwin (1999). They tested #4 and #5 bars in air and showed that deformations cause high stress concentrations at the root and serve as potential fatigue crack initiators. Also, that the ratio of the lug base radius to the lug height (*r/h*) has a significant influence on the stress concentration at the base of deformations. They conclude that bar diameter has a significant effect on the fatigue strength of bars, with larger bars having a reduced fatigue strength. The authors attribute this phenomenon to both the extra work needed to produce smaller bar sizes and the increased surface area on larger bars. The additional work in rolling a smaller bar size results in a finer grain structure and the fragmentation and dispersion of inclusions, while a larger surface area results in a higher probability of finding a critical notch on the bar surface.

2.4. Low-Cycle Fatigue Models

Various existing models attempt to mathematically predict the fatigue life of steel reinforcement, defined as the number of cycles to failure, based on the imposed strain (or stress) amplitude or cumulative energy.

The Basquin relationship (Basquin 1910) considers the elastic component of strain and can be expressed as:

$$\sigma_a = \sigma_f' \cdot \left(2 \cdot N_f\right)^b$$

Equation 2-22

where σ_a is the true stress amplitude, N_f the number of cycles to failure, $2N_f$ the number of reversals to failure, σ'_f is the fatigue strength coefficient, and b is the fatigue strength exponent. Since the deformation is elastic, it can be written as:

$$\sigma_a = \frac{\Delta\sigma}{2} = \frac{\Delta\varepsilon_e \cdot E}{2}$$ **Equation 2-23**

And:

$$\frac{\Delta\varepsilon_e}{2} = \frac{\sigma_a}{E} = \left(\frac{\sigma_f'}{E}\right) \cdot \left(2 \cdot N_f\right)^b$$ **Equation 2-24**

where $\Delta\varepsilon_e / 2$ is the elastic strain amplitude, and E is the Young's Modulus.

The plastic strain component is most commonly described by the Coffin- Manson (Coffin 1954; Manson 1953) relationship as:

$$\frac{\Delta\varepsilon_p}{2} = \varepsilon_f' \cdot \left(2 \cdot N_f\right)^c$$ **Equation 2-25**

where $\Delta\varepsilon_p / 2$ is the amplitude of the plastic strain, ε_f' is the ductility coefficient in fatigue, and c is the ductility exponent in fatigue. On a log-log plot, the Coffin-Manson relation gives a straight line of slope c. An inverse relationship between the ductility exponent, c, and the fatigue life of the member has been observed, with a lower value of c resulting in a longer fatigue life. The previous elastic and plastic relationships can be combined by superposition to obtain the total strain amplitude:

$$\frac{\Delta\varepsilon_a}{2} = \frac{\Delta\varepsilon_e}{2} + \frac{\Delta\varepsilon_p}{2} = \left(\frac{\sigma_f'}{E}\right) \cdot \left(2 \cdot N_f\right)^b + \varepsilon_f' \cdot \left(2 \cdot N_f\right)^c$$ **Equation 2-26**

It can be expected that the fatigue life curve, in terms of total strain, will tend to the plastic curve at large total-strain amplitudes, whereas it will tend to the elastic curve at low total-strain amplitudes, as shown schematically in Figure 2.31.

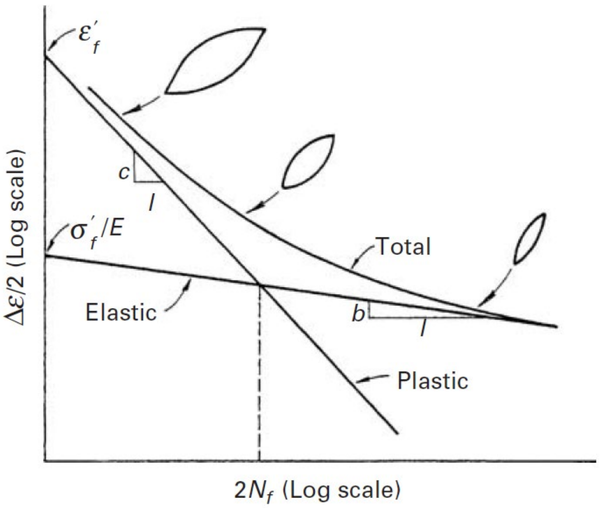

Figure 2.31. Superposition of elastic and plastic curves (Meyers, 2010).

Given the difficulty in clearly defining the plastic-strain component due to Bauschinger effects, Koh and Stephens (1991) proposed a variation of the total strain amplitude relationship as follows:

$$\frac{\Delta\varepsilon_p}{2} = M \cdot \left(2 \cdot N_f\right)^m \qquad \textbf{Equation 2-27}$$

where M and m are material constants obtained by linear regression. From the testing of ASTM A723 machined steel specimens for use in pressure vessels, they note that the mean stress relaxation, caused by the fact that both maximum and minimum stress change with each applied cycle, occur only for strain amplitudes greater than 0.5%, regardless of tensile or compressive mean strain. They conclude that mean stress relaxation is attributed directly to plastic straining.

Unfortunately, this approach only relates the fatigue life of the bar to the total number of cycles to failure, N_f, but does provide any information on the damage sustained by the bar during cycles. Nonetheless, as described by Muraki and Miller (2005), the Coffin-Manson relation virtually represents a crack propagation law. From the testing of machined plain and holed annealed medium carbon steel, Muraki and Miller propose the following Coffin-Mason type relationship derived from crack propagation:

$$ln(l_f/l_0)=5.12x10^{-21}(\Delta\sigma/2)^{6.7}(N_f-N_0) \qquad \textbf{Equation 2-28}$$

where l_0 represents the initial surface crack length at the number of stress cycles N_0, and l_f is the final crack length at failure ($N=N_f$). They conclude that the physical reality of low cycle fatigue damage is the creation of small surface cracks which are the cause of the loss of fracture ductility. Should the surface layer of a fatigued specimen be removed in order to remove the surface cracks, the phenomenon of loss of fracture ductility disappears.

Hawileh et al. (2010) observed that the prediction of fatigue life based on the total strain amplitude is more accurate than that of the plastic strain amplitude. In their work, they tested thirty-two BS 460B and twenty-two BS B500B unmachined steel reinforcing bars with maximum strain ranging from 3-10% for different strain ratios.

Mander et al.(1994) performed a series of constant-amplitude low-cycle fatigue behavior of ASTM A615 grade 40 reinforcing steel bars and ASTM A722 high strength prestressing bars under reversed cyclic loading. Mander concluded that mean stress and mean strain have negligible effect on the low-cycle fatigue life of ordinary deformed steel reinforcement when subjected to large strain amplitudes, between 1-5%.

Similarly, from the testing of machined round solid bars made of carbon 45 steel, Yang (2005) indicates that, for different mean strains under the same cyclic saturated true plastic strain amplitude, mean strain does not have a significant influence on the low-cycle fatigue life of the bars. Nonetheless, mean strain does influence the material's instantaneous plastic behavior. He also suggests that true plastic strain amplitude dominates the low-cycle fatigue life under cyclic strain loading, with and without engineering mean strain.

A major limitation of the fatigue models discussed so far is the restriction to fatigue under the simple condition of constant amplitude. In real life, materials are subjected to random loads, mean stress levels, and variable strain amplitudes. In order to improve these limitations, cumulative-damage theories attempt to predict the fatigue life of a component subjected to variable amplitude conditions, starting from data obtained in simple constant amplitude tests. Basically, these theories keep track of the accumulating damage in a material until a maximum tolerable damage level is reached. This linear damage model is generally known as the Palmer-Miner (Miner 1945) rule and gives an empirical way of predicting the fatigue life of a material after a complex loading sequence. The main assumption is that the rate of damage accumulation at any level does not depend on any prior loading history imposed on the material. In other words, the damage per cycle at a given strain/stress level is the same at the beginning or at the end of loading. This implies that the magnitude and direction of the change in amplitude, from low to high or high to low, do not have an effect on fatigue life. The models also assume that loading is totally reversible. These assumptions are not representative of actual behavior, as for example, a crack initiated at high loads can continue to grow at low loads, whereas in the reverse case, at low loads, perhaps the crack would never have formed. However, Murakami and Miller

(2005) concluded that prior fatigue history hardly influences the subsequent microcrack growth rate in the low-cycle fatigue range.

More recently, energy-based fatigue life models are becoming increasingly popular. An appealing aspect of such models is the possibility of equating the total energy to failure as a function of strain amplitude. Mander et al. (1994) proposed the following relationship:

$$W_{fT} = W_a \cdot \left(\varepsilon_\alpha\right)^p$$

Equation 2-29

$$W_{fT} = W_b \cdot \left(f_{mx} \cdot \varepsilon_\alpha\right)^q$$

Equation 2-30

where W_a, W_b, p, and q are material constants, ε_α can be either the total or plastic strain amplitude, and f_{mx} is the magnitude of the maximum stress (tension or compression) from the entire strain history in order to be applicable for cumulative damage modeling applications for a random history. However, results from Brown and Kunnath (2004) suggest this energy-based model is not as good an indicator of the inelastic fatigue-life as models dealing with half-cycles to failure, $2N_f$.

2.5. Gaps in Knowledge

Little is known about the development of micro-cracks in buckled reinforcing steel bars. As previously noted, all damage processes have typically been simply lumped as "low-cycle fatigue," which only considers the number of cycles and strain amplitude in a formulation such as Coffin-Manson's. Moreover, most of the existing data is for small-diameter reinforcing bars under small-amplitude cyclic testing. Definition of strain alone poses an interesting and rarely explored problem. Should the strain amplitude used to determine the low-fatigue of the bars be defined at the global level, at the local level, or at the microscopic level? The problem of defining strain at the local level alone is that the buckling observed in test samples is slightly different from the buckling observed in longitudinal bars in columns, so such formulation can contain a significant bias. The definition of strain at the microscopic level would also pose a problem as it would only be meaningful within a metallurgist perspective. Perhaps the best engineering approach is to establish relationships between global and local strains and relate strain amplitude and damage between these two strain definitions. Regarding the mechanical splices used with large diameter bars, there is very limited publicly available literature describing their performance under large amplitude strain reversals. Most of the work has been conducted on high-cycle fatigue testing of mechanical splices and such tests are mainly performed to meet acceptance criteria such as Caltrans CT 670 (Caltrans 2013). Paulson and Hanson (1991) summarize many conducted tests.

Chapter 2, in part, is a reprint of the material as it appears in *SSRP Report 17/10: Plastic buckling-straightening fatigue of large diameter reinforcing steel bars*, 2018. Duck, D. E.; Carreño, R.; and Restrepo, J. I. The dissertation author was the primary investigator and author of this report.

Chapter 2, in part is currently being prepared for submission for publication of the material. Duck, D. E. & Restrepo, J. I. The dissertation author was the primary investigator and author of this material.

CHAPTER 3.

EXPERIMENTAL WORK

3.1. General

This chapter will cover the design and implementation of a loading apparatus capable of cyclically testing large diameter reinforcing steel bars under large strain amplitudes. See Figure 3.1. The main objective will be to characterize the plastic buckling-straightening fatigue life of the bars. The innovative use of a modified sulfur-based concrete to grip the bars will be explained along with the many aspects required to perform the experimental work. Experimental issues will also be covered as well as how they were solved. The material properties and geometrical characteristics of the tested large diameter bars will be provided. The geometrical characteristics will be explored to investigate their effect on the fatigue life of the bars. An explanation and derivation of the testing protocols used in the experimental work will be given and results will be studied and compared with existing fatigue models.

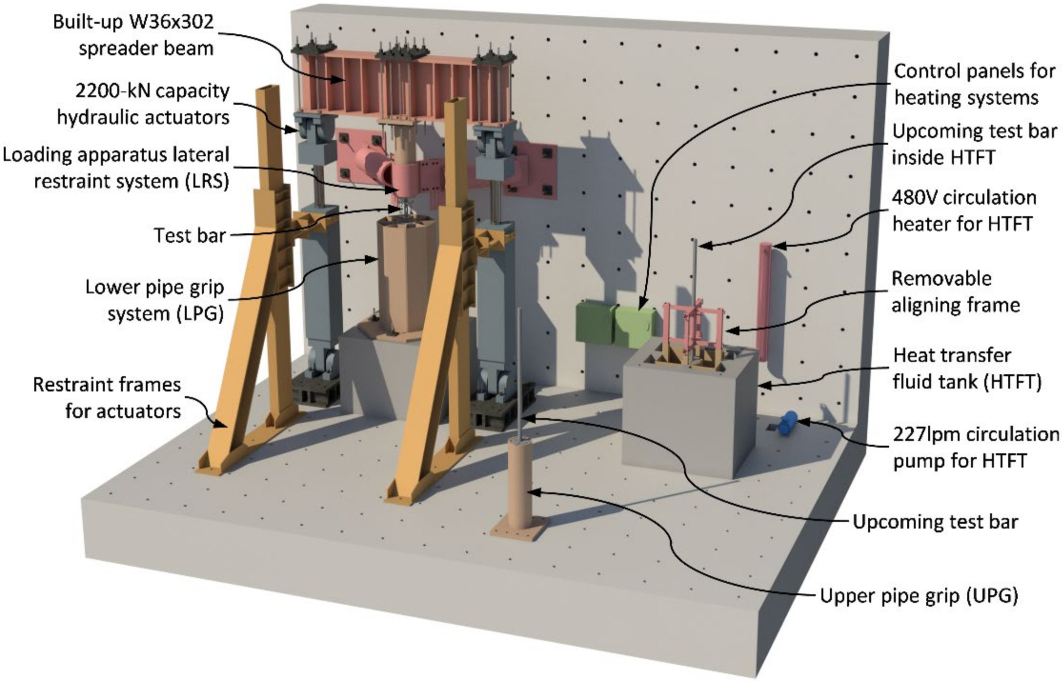

Figure 3.1. Rendering of loading apparatus.

3.2. Loading Apparatus Design and Specifications

Successful PBSF testing of No. 18 bars require a loading apparatus able to transfer the loads to the bars without the use of mechanical grips and to have near zero rotation and relative displacement at the bar ends. Mechanical grips tend to either split or to cause fracture of the bars at the end of the grips (Sanchez, 2001). To overcome these issues, a reusable grip mechanism was provided as part of the loading apparatus by embedding the ends of the bars into a highly-confined sulfur concrete (SC) made out of modified sulfur and coarse mineral aggregate (ACI Committee 548, 1993). Modified sulfur melts at a temperature of 246 °F with an ideal temperature range for handling between 265 °F and 290 °F (ASTM C386 2012). Within this range, molten sulfur behaves as a free-flowing liquid that can easily mix with mineral aggregate. Also, within this temperature range emissions of sulfur dioxide are limited. The main characteristics of SC that made it an ideal candidate to be used as part of the gripping mechanism include:

1) High compressive and bond strength
2) Rapid solidification and strength gain upon cooling
3) Recyclable mix

Similar to the effects that the amount of cement, water content, and aggregate type and gradation have on Portland Cement Concrete (PCC) strength, the strength properties of SC are determined by the amount of sulfur cement binder and aggregate gradation and type. Compression tests on a series of sulfur concrete mix designs were performed in order to obtain the best performance. Different amounts of 3/8-in. diameter smooth beach pebbles and crushed aggregates were mixed with different ratios of plasticized, hot-pour silica filled, modified sulfur. Figure 3.2 shows the different materials used. Table 3.1 summarizes the material weight percentages, the unit weight, compressive strength, as well as the age at the time of testing for the two mix designs used in the experimental work. See Appendix A for a complete list of all mix design trials. Mix designs were divided in four main categories, depending on the materials used: 1) SU – sulfur only, 2) CA – sulfur with crushed aggregate, 3) SA – sulfur with smooth aggregate, and 4) MA – sulfur with mixed crushed and smooth aggregate. As seen from the tabulated results, some mix designs were able to achieve a compressive strength of over 6ksi in less than 24hrs.

(a) (b) (c)

Figure 3.2. Sulfur concrete mix design materials: (a) 3/8 in. diameter smooth beach pebbles; (b) 3/8 in. diameter rough crushed aggregate (c) Plasticized, hot-pour silica filled, modified sulfur.

Table 3.1. Material properties of concrete sulfur mix designs

	Mix Design 1	Mix Design 2
Modified Sulfur, % weight	33	44
Crushed aggregate, % weight	33	56
Smooth aggregate, % weight	34	0
ρ, lb/ft^3 (kg/m^3)	150 (2400)	144 (2300)
f'_c, ksi (MPa)	4.5 (31)	5.1 (35)

A mix design falling under the MA category was used for both upper and lower grip pipes for the first half of the experimental work, which included most of the trial cyclic tests performed. This mix design will be referred to as mix design No. 1. It had a relative density of 2.4 and a compressive strength, f'_c, of 4.5 ksi. Such material properties are very similar to those obtained by normal-weight PCC. The compressive strength of this mix design was not the highest attained (8.5 ksi) from all trials due primarily to the usage of 0.375 in. diameter smooth beach pebbles but was used for the first half of the experimental work for comparison purposes. While the main function of aggregate in both PCC and SC is to act as a filler, it also plays a critical role in helping reduce the inherent thermal contraction in SC (Bretz Jr., 1979). Such thermal contraction is mostly due to the crystallographic inversion from the monoclinic to the orthorhombic form, which can result in considerable shrinkage and voids (Czarnecki and Gillott, 1990). The second mix design used for the second half of the experimental work belonged in the CA category and will be referred to as mix design No. 2. It had a higher f'_c of 5.1 ksi but a lower relative density of 2.3 and only included 0.375 in. crushed aggregate. No significant differences in performance were noted between these two mix designs. These results are in line with those described by Gregor and Hackl (1978) and Czarnecki and Gillot (1989) who concluded that the strength of sulfur concrete was dependent on the content of the sulfur binder. Higher contents of the binder resulted in lower compressive strengths, except when smooth and round aggregate was used, which resulted in a reversed relationship. The compressive strength for all mix designs at 24 hrs. of age attained at least 4.0 ksi, consistent with previous test results by others (ACI Committee 548, 1993; Samarai, Laquerbe, and Al-Hadithi, 1985; McBee, Sullivan, and Fike, 1985; Weber, 1993; Gracia, Vazquez, and Carmona, 2004). Such rapid gain in strength, combined with the fact that sulfur can be recycled, greatly reduced the costs of testing by allowing for the repeated use of a single test setup. Nonetheless, due to the lack of consistent data on the effects on the material properties of SC but with reports of durability problems caused by thermal cycling (Muir, 1982), modified sulfur was gradually but consistently replaced after each test to prevent any considerable deterioration of the SC.

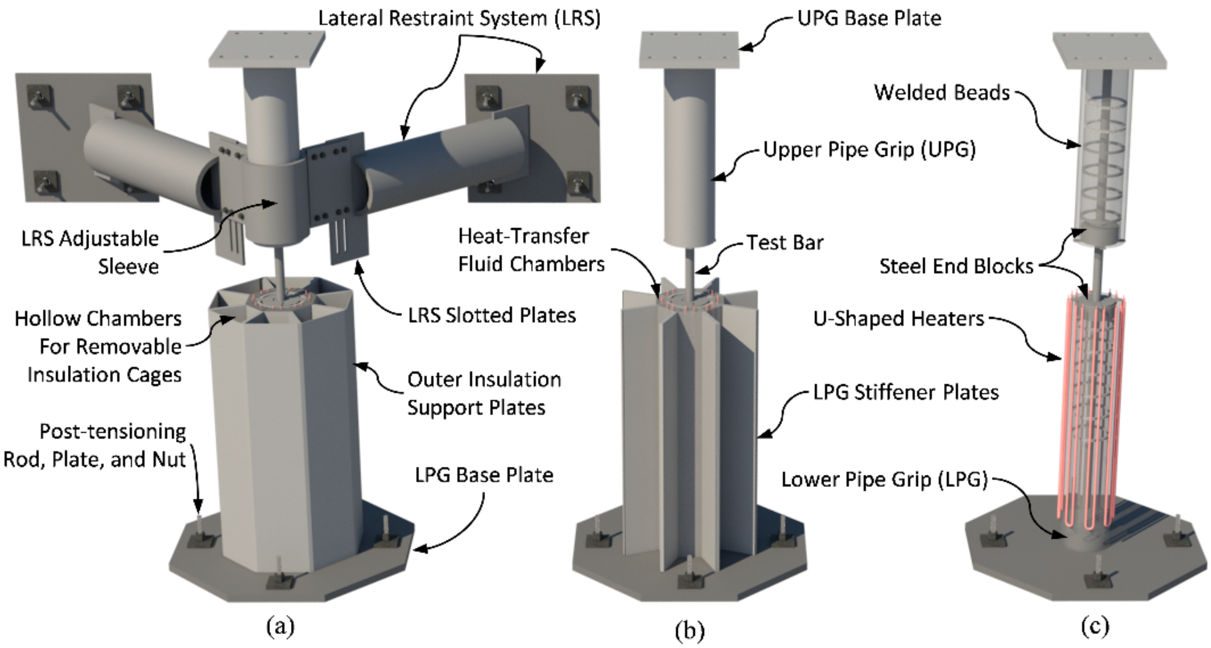

Figure 3.3. Upper and lower pipe grips: (a) Grips and lateral restrain system; (b) Lower pipe grip without external plates and upper pipe without lateral restrain system; (c) Heating system for lower pipe grip and internal view of welded beads and steel blocks for both pipe grips.

The loading apparatus, see Figure 3.3, had to be sufficiently rigid to sustain the bending moment due to buckling of the test bars while providing near perfect fixed-end boundary conditions at the bar ends. A grip rotation of 0.002 radians, or less, was used to define a perfect fixed-end condition. For the design, the expected plastic moment corresponding to a No. 18 Grade 80 bar was used assuming an ultimate compressive load, f_u, equivalent to twice the yield strength of the bar ($f_u = 2 \cdot f_y$). See Figure 3.4.

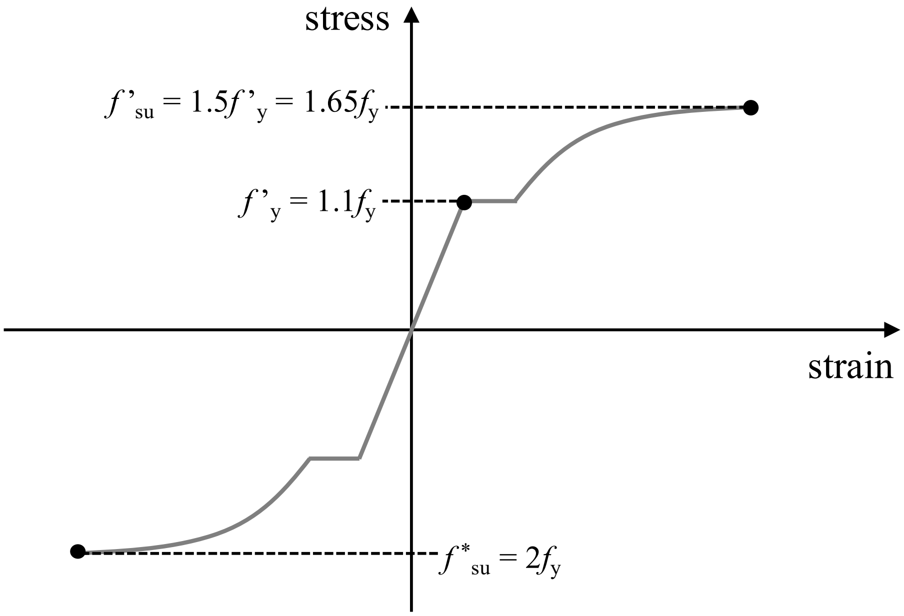

$$A_{\#18}=4.0in^2$$

$$d_{\#18}=2.257in$$

$$f_y=80ksi$$

$$f_{max}=f_s^*=2\times 80ksi=160ksi$$

$$F_{max}=f_{max}\times A_{\#18}=640kips$$

$$Z_p=\frac{(d_{\#18})^3}{6}=1.92in^3$$

$$M_p=f_{max}\times Z_p=25.6k\text{-}ft$$

Figure 3.4. Loading apparatus design stresses.

The resulting design moment of 25.6 kip-ft, see Figure 3.4, had to be resisted by the upper and lower pipe grips, with separate systems used to provide the required stiffness to each grip; see Figure 3.3. For the lower pipe grip (LPG), a total of eight ½ in. thick ASTM A36 stiffener steel plates were welded equally-spaced around the full height of the ASTM A53 Grade B NPS 12 core pipe. The pipe had an outside diameter (OD) of 12.75 in., was

0.687 in. thick and 67 in. tall. Both the pipe and stiffener plates were welded to a 2 in. thick A36 steel base plate. See Figure 3.5.

Figure 3.5. Lower pipe grip with stiffener plates shown.

The base plate was connected to a strong floor through a concrete pedestal using four 2.5 in. diameter post-tensioning threaded bars with a total load of 1,550 kips. Given that the bottom pipe grip was to remain fixed to the foundation for the duration of the experimental work, an in-situ heating system to melt the sulfur concrete inside the pipe grip was incorporated around the pipe. Steel plates with a thickness of 0.188 in. were welded between the pipe grip stiffener plates, around the pipe's circumference and along the pipe’s full length. See Figure 3.6. These chambers were filled with an off-the-shelf high-viscosity index, non-corrosive, paraffinic heat transfer fluid with a flash point above 400 °F. Heat was provided by eight 480V 3-phase custom-made U-shaped electrical heaters embedded the chambers. The eight heaters were connected in parallel and their temperature was regulated to 310 °F by an external control panel. The heating system was designed such that the power provided by the individual heaters would melt the core of the sulfur concrete inside the pipe grip in approximately four hours. To prevent excessive heat loss while heating, the entire lower setup was wrapped in 6 in. thick stone wool insulation capable of withstanding temperatures of up to 2150 °F. To support the insulation, 0.188 in. thick plates were welded at the ends of the stiffener plates, along their full height. Given the hollow chambers created by these plates, removable cages of insulation were placed inside of them to further insulate the system. While the outer insulation was not removable, the interior insulation cages were removable to allow for the system to cool down faster, if desired, by removing such cages. To transfer the axial forces applied to the bar, through bearing and surface bond between the sulfur and the pipe, six rows of ¾-in. thick weld beads spaced at 6 in. on-center, similar to those tested by Gebman et al. (2006), were welded on the interior surface of the pipe grip to provide mechanical bond. See Figure 3.7.

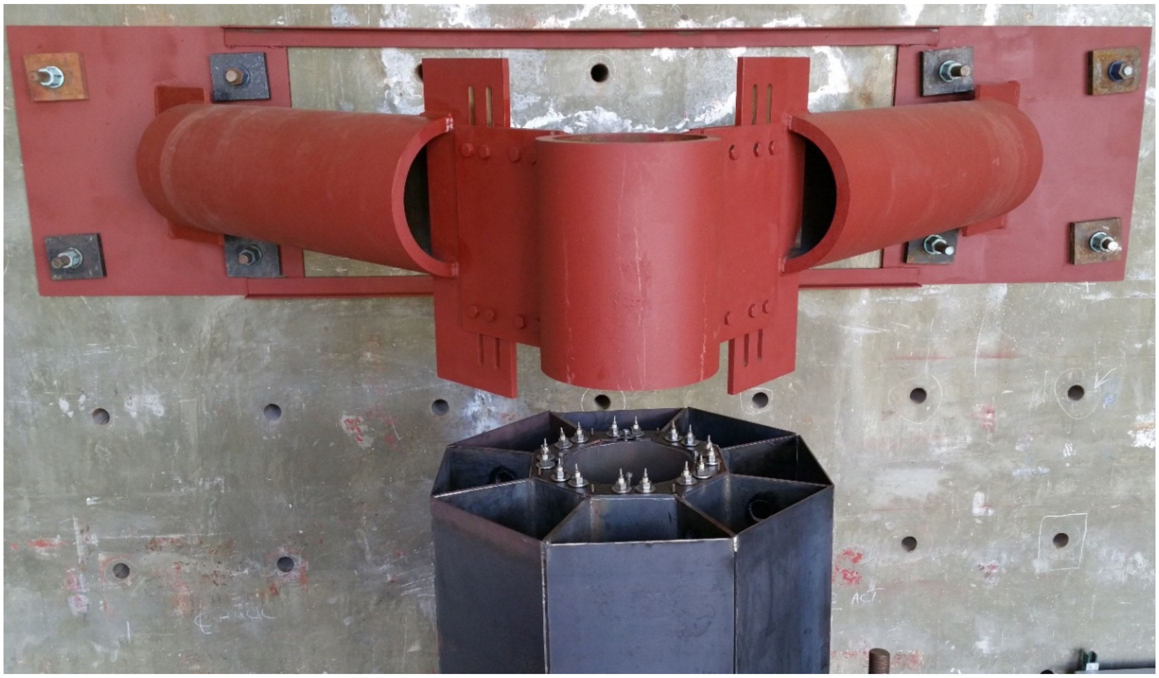

Figure 3.6. View of bottom pipe with heater terminals and lateral bracing system.

Figure 3.7. ¾-in. thick beads at 6 in. on-center inside pipe grip.

Unlike the lower pipe grip which was fixed, the upper pipe grip needed to be able to move vertically. To provide the required lateral stiffness for this pipe grip, a lateral bracing system that only allowed for vertical movement with minimal rotation was designed. The system consisted of an outer sleeve through which the upper pipe grip could slide, connected to two diagonal braces. See Figure 3.6. The sleeve was designed to resist the design moment with minimal friction loss by providing a graphite greased brass shim between the pipe and the sleeve. As shown in Figure 3.8, by assuming contact points between the pipe and the sleeve, when the bar buckles, equivalent to ¾ of the sleeve length, the expected friction force was calculated to be 1.2% of the applied load.

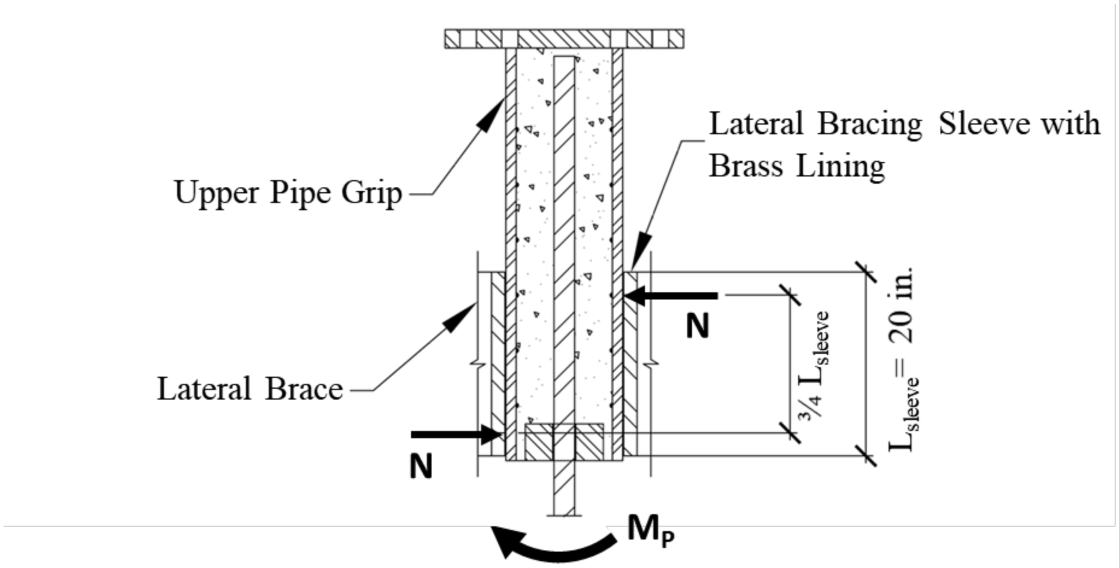

$$\mu_s = 0.19 \ \text{(friction coefficient)}$$

$$N = \frac{M_p}{\frac{3}{4}\times L_{sleeve}} = \frac{307\,kip\text{-}in}{15\,in} = 20.5\,kips$$

$$F_{friction} = 2\times\mu_s\times N = 7.78\,kips \ \ (1.2\% \text{ of } F_{max} < 2\%)$$

Figure 3.8. Friction calculation between upper pipe grip and outer sleeve.

The outer sleeve and lateral braces were ASTM A53 Grade B NPS 16 pipes with an OD of 16 in. and a thickness of 1.44 in. The connection between the sleeve and each lateral brace was made with three ¾ in. thick plates. An inner plate with four 13/16 in. diameter slotted holes to allow for vertical adjustments of the sleeve and two outside plates with eight 13/16 in. diameter holes to clamp the inner plate. A preliminary finite element analysis of the lower pipe grip was performed in SAP2000 to ensure that the maximum rotation at the top of the grip remained below 0.002 radians when the design moment, equivalent to the plastic moment of the Grade80 #18 bar, was applied at the center of the pipe. The pipe, stiffener plates, and base plate were modeled as thick shell elements with material properties meeting the previously discussed ASTM standards; the concrete pedestal was modeled as a solid element with a compressive strength of 4,000 psi. The sulfur concrete inside the pipe was not modeled in order to simplify the analysis and to be conservative, by ignoring the stiffening effect of the sulfur concrete inside the pipe. A "plate" constraint was added to all the top nodes of the pipe, stiffener plates, and center node (where the load was applied). This type of constraint is flexible in-plane and rigid against out-of-plane bending. Results of the normalized Von Mises stresses, shown in Figure 3.9, showed that the entire system was expected to remain well in the elastic range. The maximum expected rotation was $1.61\text{x}10^{-4}$ radians, or about 8.05% of the maximum allowable rotation of 0.002 radians. The length of each of the pipe grips was determined from the minimum length required to develop the expected ultimate strength of a No. 18 Grade 60 bar. Based on AASHTO-14 (2014) recommendations, a minimum development length, l_d, equivalent to $25d_b$ or 56.3 in. was required.

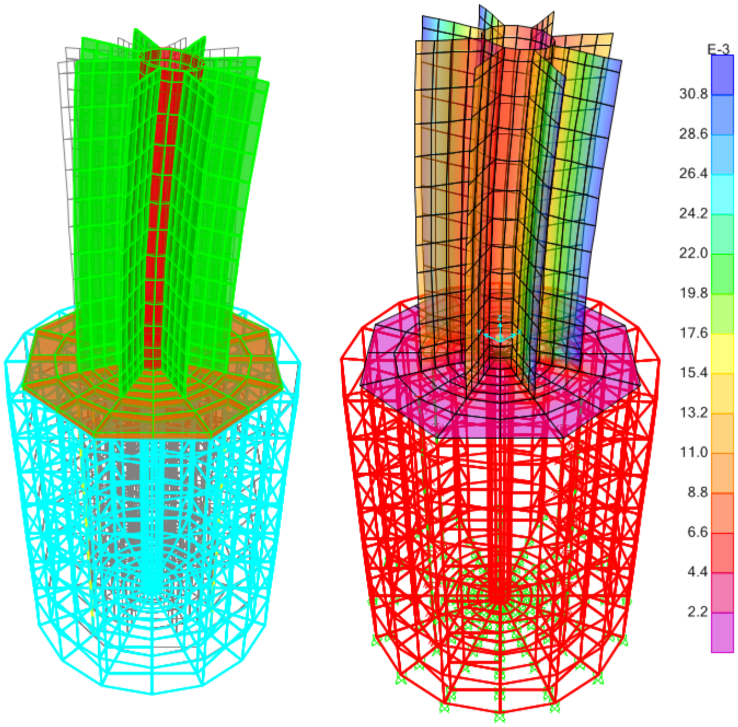

Figure 3.9. Normalized Von Mises stresses on lower pipe grip setup from finite element analysis performed in SAP2000.

In order to reduce the material cost of the loading apparatus (steel, sulfur, transfer fluid) and melting time of the sulfur, a reduced minimum l_d of 19d_b or 42.8 in. was attained by taking into account the high confinement provided by the pipes and based on results from bond slip tests (Raynor, Lehman, and Stanton 2002; Murcia-Delso and Benson Shing 2015). While such tests successfully used shorter l_d than suggested by current code equations, the tests were monotonically performed on bars grouted into corrugated steel ducts that do not necessarily replicated the test configuration used in the loading apparatus. Hence, a conservative design approach led to an upper pipe grip length of 48 in. Furthermore, due to the complexity of the lower pipe grip and in order to allow for testing of mechanically-spliced No. 18 Grade 60 bars, No. 18 Grade 80 bars or No. 14 Grade 100 bars without the need to make modifications, a larger length of 67 in. was used to accommodate the larger development lengths needed for such tests. Actual embedment lengths used during cyclic testing of unspliced No. 18 ASTM A706 Grade 60 bars ranged from $17d_b$ or 39 in. to $19d_b$ or 44 in. However, two successful trial tensile tests were performed with a development length of only $14d_b$ or 32 in. This reduced development length is in line with previous pullout tests on No. 18 bars grouted into ducts where fracture was achieved with a l_d of only $10d_b$ (Steuck, Eberhard, and Stanton 2009).

Similar to Mander (1983), a 4 in. thick circular steel plate with a 2.5 in. diameter center hole was placed at the top surface of each pipe grip; see Figure 3.10. These plates helped restrain the bars when these buckled and simulated the restraint provided by the transverse reinforcement present in reinforced concrete columns. The plates were supported by L-shaped brackets uniformly welded around the inside of the pipes to reduce stress concentrations and the possibility of yielding the pipe by providing a tight fit that prevented their rotation when the bars buckled. To allow for the removal of the plates in between tests, the plates were machined in two halves and bolted together so they could be placed around the test bars before testing and removed afterwards. The thickness of these plates was not accounted for in the calculation of the bar's development length.


(a) (b)

Figure 3.10. (a) Circular steel plate; (b) L-shaped support brackets for steel blocks.

Since the upper pipe grip was to be removed between tests, a heat transfer fluid tank capable of fitting the entire pipe grip and its 2 in. thick base plate was built adjacent to the loading frame to melt the sulfur inside the pipe grip; see Figure 3.1. The same heat transfer fluid was used as in the lower pipe heating system. The heat transfer fluid was circulated through a 480V 8 in. diameter circulation heater using a pump capable of pumping the fluid at 60 gpm. See Figure 3.11. A flow switch was placed on the heater's inlet to ensure that the heating system would shut off if no flow was detected, therefore, preventing damage to the heater. As with the other heating system, the heater was connected to a control panel capable of regulating the temperature to 310 °F. The heating system was also designed such that the power provided by the circulation heater would melt the core of the sulfur concrete inside the heat transfer fluid tank in four hours. Hollow voids were created around the steel walls containing the heat transfer fluid to place insulation cages similar to those of the lower pipe heating system. Axial load was applied using two 500-kip capacity servo-controlled hydraulic actuators with a ±24 in. stroke. The actuators were connected together by a heavily-reinforced, built-up, W36x302 spreader beam. The upper pipe grip was post-tensioned to the spreader beam by eight 1-3/8 in. diameter high strength post-tensioning rods. The complete set of drawings are shown in Appendix B.

Figure 3.11. Heat transfer fluid tank heat circulation system.

Figure 3.12. Built-up, W36x302 spreader beam.

3.3. Instrumentation

Given the importance of establishing a relationship between smeared and local strains to define strain amplitude and bar damage state, each bar was well-instrumented. Smeared strains for each test bar were measured using at least two diametrically-opposite clip gages with a fixed gage length equal to half the bar's unsupported length, s. The clip gages were designed and built in-house specifically for this project and consisted of 0.0591 in thick, 0.5 in. wide, high-strength 7075-T6 aluminum alloy arches mounted on a steel frame, see Figure 3.13, and were reusable. Each clip gage arch was instrumented with a full Wheatstone bridge (bending) configuration using 0.197 in. long, 120-Ohm electrical foil strain gages, placed at the apex of the arch. The thickness and dimensions of the arches were such that, at a maximum expected bar elongation of 6%, the axial strain in the arches remained below 50% of their yield strain. While the main objective of these clip gages was to accurately measure large deformations even when the bars buckled, their design resulted in an excellent resolution for strains less than the bar's yield strain. Two pairs of clip gages were built, one for unsupported lengths of $6d_b$ or 13.5 in. and another for $8d_b$ or 18 in. The clip gages were calibrated back-to-back with a 1.97 in. gage length axial extensometer meeting ASTM E83 Class B1 standards via various tensile tests on reinforcing bars. From this comparison, calibration factors were obtained to relate the axial strain of the clip gage arches to the axial strain of the bar. The four contact points of the clip gages with the test bars where along the bar's vertical ribs at the quarter points using hardened steel tips used in center punch tools. Four 0.039 in. diameter by 0.0197 in. deep holes were made on the test bar using a center punch for each of the steel tips to rest on.

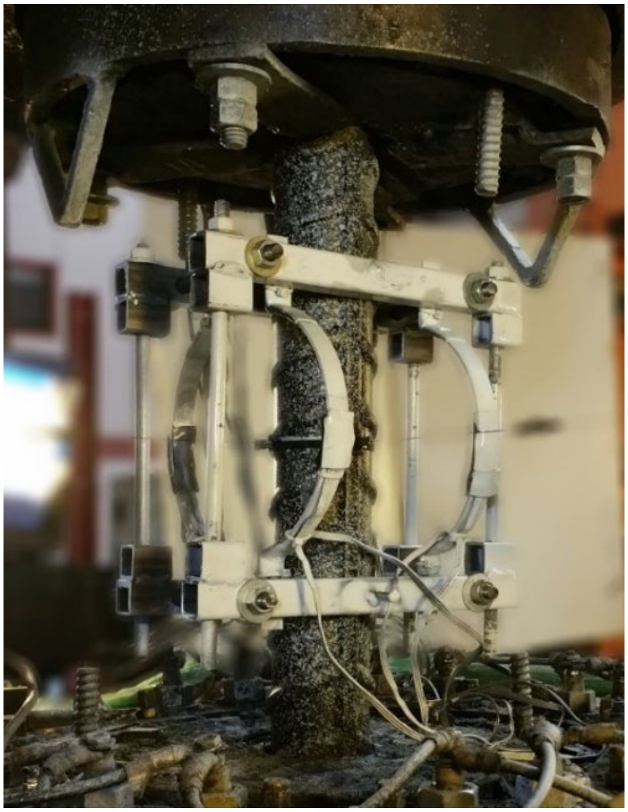

Figure 3.13. Instrumented bar with white-over-black speckle pattern for DIC.

To ensure that the steel tips remained in contact with the test bar at all times, 1.5 in. long, 0.063 in. thick wire-springs with an outside diameter of 0.47 in. were used to clamp the clip gages to the bar. These springs were horizontally placed over each of the four 0.313 in. diameter round rods connecting the two clip gage frames. These rods were threaded at both ends in order to allow for a nut and washer to fully compress the springs and ensure a constant compressive force on the clips gage while testing. The calculated smeared strain from the clip gage was used to control the tests by triggering a load reversal once a predetermined strain target from the strain history protocol was reached. Figure 3.14 shows the loading system diagram. While the attachment mechanism of the clip gage proved effective, the clip gage slipped during testing in two out of the twenty-one tests where the clip gage was used. Results from these two tests were discarded.

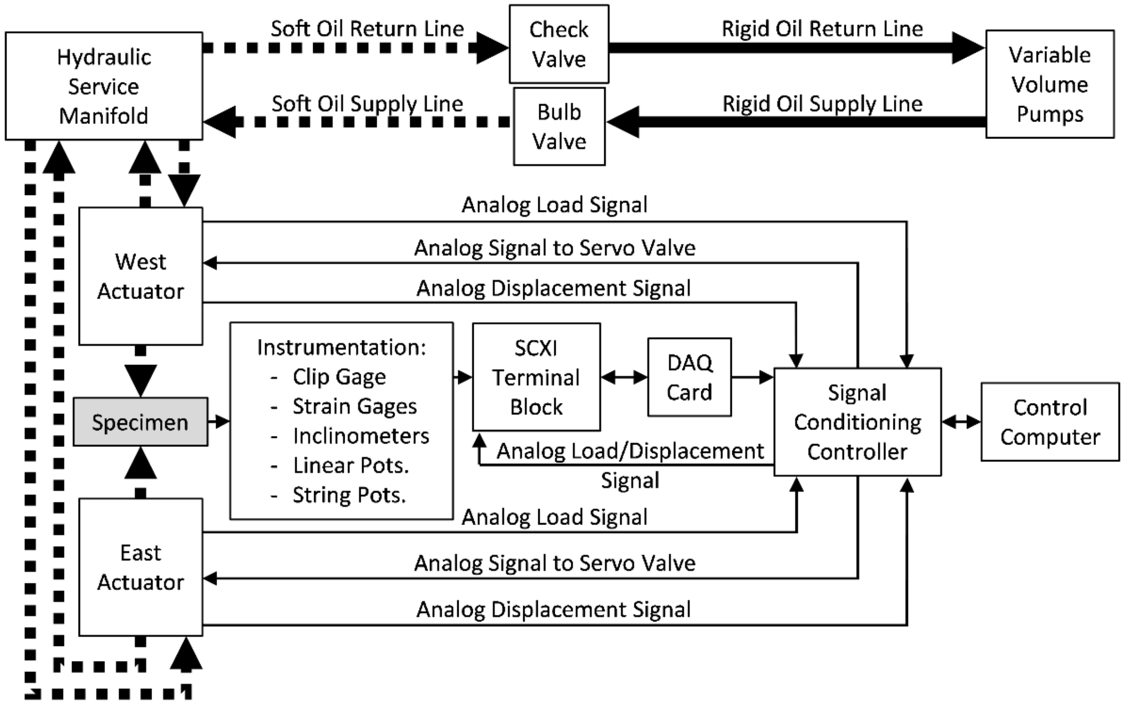

Figure 3.14. Instrumentation and loading system schematics.

Local longitudinal bar strains were measured by 0.197 in. long electrical-foil strain gages. Two diametrically-opposite strain gages, orthogonal to the face of the bar's vertical ribs, were placed at quarter points to measure the axial strain of the test bars. A total of five strain gages were also placed oriented longitudinally at mid-height of the bar's unsupported length to calculate the strain plane and to derive the maximum compressive strain at the concave face and the maximum tensile strain at the convex face of the buckled bars. This was done because the direction of buckling could not be predetermined *a priori* and in spite that the bar cross-section was slightly oblong and the longitudinal deformations had a slight influence on the cross-section properties. By using a least-squares solution based on the exact location of each strain gage relative to each other and comparing the strain data from each strain gage to calculate the curvature at the mid-section of the tested test bars, where the plastic-hinge is generated after the onset of buckling. Under the Euler-Bernoulli assumption that plane sections before bending remain plane after bending, finding the average strain and curvature of a deformed section is equivalent to computing the parameters of the plane containing the deformed section. By using sets of three strain gages, the coordinates of three points are known and the parameters of the equation of the plane could be solved from a simple linear system with equal number of equations and unknowns. Given the average spacing between bar deformations, 1.42 in. for bars from manufacturer A (MFR A) and 1.09 in. for manufacturer B (MFR B), these strain gages were applied on the bar between deformations. By not having to grind deformations to apply the strain gages, the bar's original form was preserved. Removal of a bar deformation in this critical region was likely to impact the fatigue life of the bar.

Rotations at the upper and lower grip pipes and at the loading beam were measured using pairs of inclinometers, placed orthogonal to each other, at each of these locations, see Figure 3.15. These measurements were used to obtain the rotational rigidity of the loading apparatus and ensure it met the required design parameters when the bars buckled. Relative horizontal displacements between the upper pipe grip and the lateral restraint sleeve were measured through four linear potentiometers place atop the sleeve and bearing against the upper pipe grip. The potentiometers were placed facing the four cardinal points. Vertical displacement of the spreader beam was measured by four cable-extension displacement transducers, referred from here on as string potentiometers. The devices were placed on the strong floor, away from the actuators, one on each corner of the beam. In some tests, two orthogonal string potentiometers were also attached at the mid-height of the bar’s unsupported length to measure out-of-plane horizontal displacements when the bars buckled. These were placed approximately 12 in. away from the bar, so any vertical displacement of the bar due to bar elongation or slip affected the horizontal readings of the instruments. Furthermore, in some instances when the bars buckled, the strings of the devices were pushed by the aluminum arches of the clip gage. As a result, data from these devices mainly served as a rough estimate of the overall behavior of the buckled test bars.

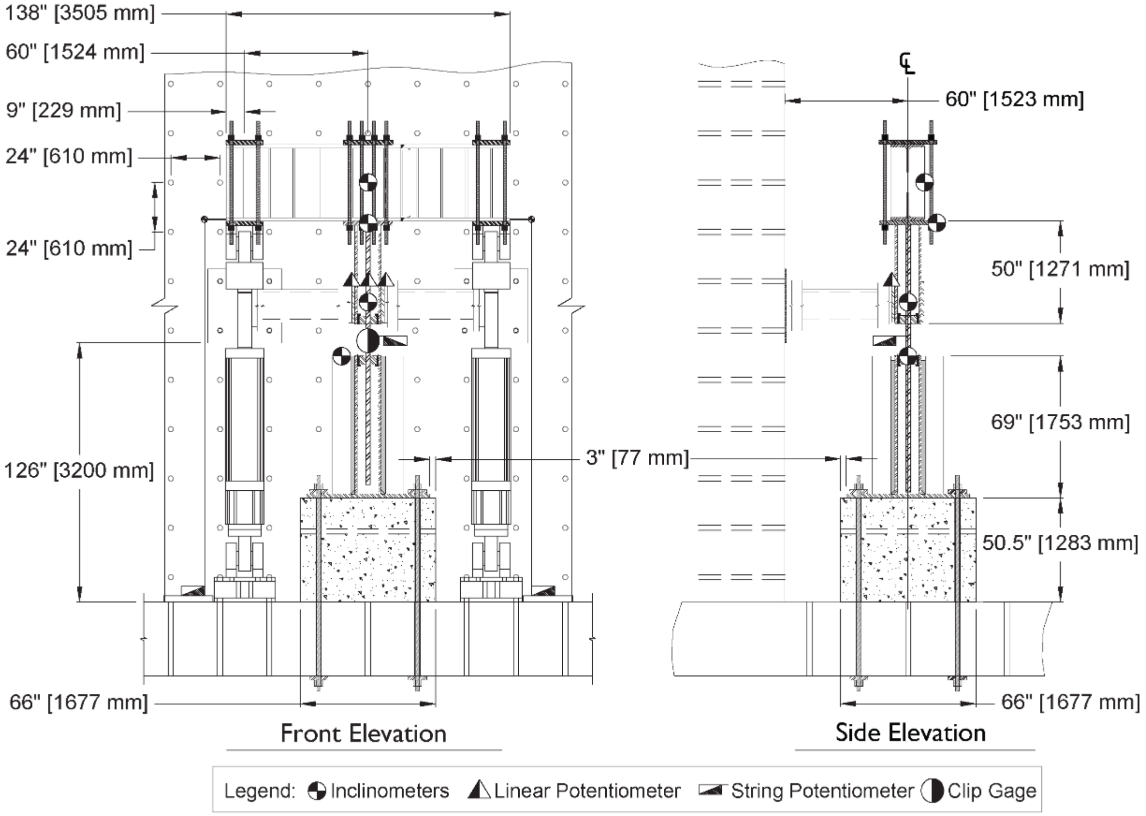

Figure 3.15. Loading apparatus front and side elevations with overall dimensions and instrumentation layout.

Digital Image Correlation (DIC) was employed for redundancy in strain measurements and to obtain information not easily achieved through the use of conventional instrumentation, such as strain profiles and out-of-plane measurements. The DIC setup consisted of six interconnected high-resolution monochromatic cameras with six LED lights. The 2.8-megapixel cameras had a 1928 x 1448 resolution and were capable of taking up to 13 frames per second (fps). The cameras had a 1/1.8 charge-coupled device (CCD) sensor with a 3.69µm pixel size. Four sets of cameras and LED lights were distributed to the north and two sets to the south of the loading apparatus in order to obtain images of the test bars from different angles. The cameras were synchronized using an asynchronous trigger in the form of a square wave signal from a signal generator. Due to the quasi-static nature of the test protocols, a square wave signal with a 0.5Hz frequency was used to record one frame every two seconds. All cameras were interconnected through a USB hub connected to a portable computer that stored all images. The uncompressed monochrome images were post-processed using a commercially available DIC software. Prior to each test, the DIC camera setup was calibrated relative to the test bar using a 3D 2-level calibration plate, see Figure 3.16. The markings on the plate were used by the software to calculate the focal length of each camera as well as the distance to the test bar. This information was used to create a 3D representation of the position of each camera relative to the test bar.

Figure 3.16. Calibration plate for DIC post-processing.

In order to improve the resolution of the results from the DIC, the bar mill scale was removed from the test bars over the unsupported length and a white-over-black speckle pattern was applied using a latex-based spray paint, see Figure 3.13. Similar to the calculation of smeared strains using mechanical instrumentation where the gage length over which the measurements are taken directly influence the results, different size windows (gage lengths) measured in pixels were used in the DIC analysis to obtain bar strain profiles. The smaller the window size used to calculate the displacement vectors resulted in a better spatial resolution but with more noise. Below a lower threshold limit with an equivalent window size of 0.187 in. the amount of noise in the results became excessive, see Figure 3.17(a). By using a larger window size, the calculated displacement vectors were smeared over a larger gage length, resulting in a decrease in spatial resolution and noise, see Figure 3.17(c) with an equivalent window size of 0.815 in. Increasing the window size beyond an upper threshold corresponding to a window size of 1.55 in. resulted in an almost uniform strain profile, see Figure 3.17(d). Based on these results, a window size equal to 0.292 in. was used for all DIC analyses, see Figure 3.17(b).

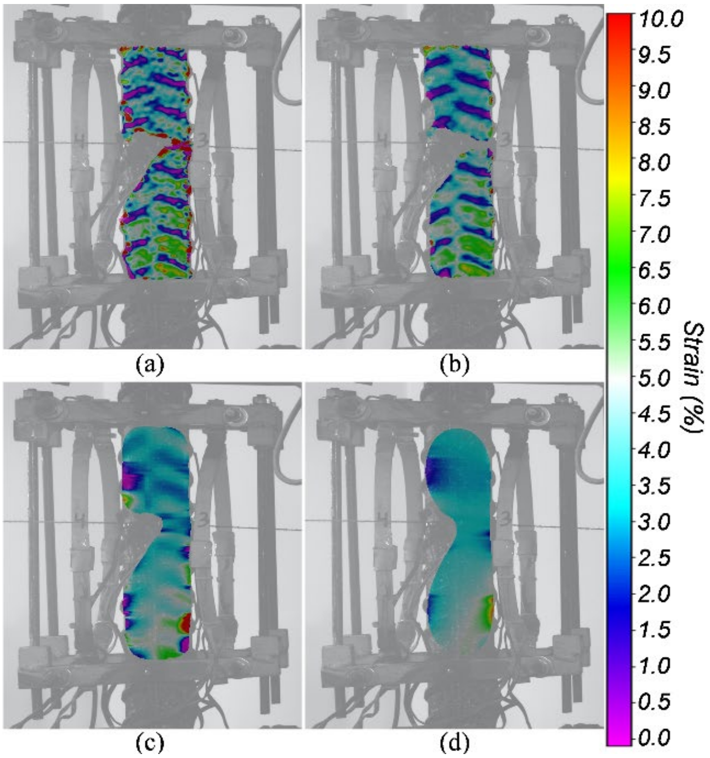

Figure 3.17. DIC Analysis Using Different Window Sizes to Calculate Displacement Vectors: (a) 0.187 in.; (b) 0.292 in.; (c) 0.815 in.; (d) 1.55 in.

High-temperature type K thermocouples (T/C) were used to monitor and regulate the temperature of heat transfer fluid used as part of the heating systems, see Figure 3.18. The lower pipe heating system, a single T/C was used to control the temperature of the heating system by regulating the power provided to the individual heaters around the lower pipe grip to maintain a heat transfer fluid temperature of 310 °F. A second T/C was used to limit the maximum temperature reached by the system. This limit was set to 330 °F, which if reached, would shut off the heating system to ensure that the maximum allowable temperature suggested by the sulfur manufacturer was not reached. Data from the remaining six T/C was recorded by the 16-bit commercial Data Acquisition System (DAQ) and was plotted live to visually monitor the heating process. Similarly, temperature inside the circulation heater used as part of the heat transfer fluid tank system was regulated to 310 °F through an internal T/C. A separate internal T/C was used to shut off the heating system if a transfer fluid temperature of 330 °F was ever reached.

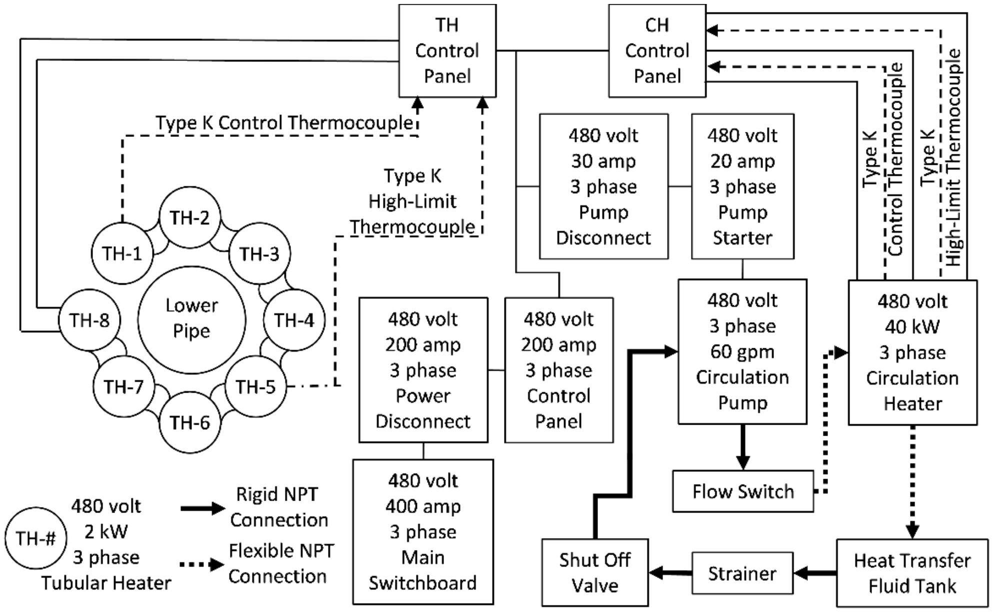

Figure 3.18. Heating system schematics.

3.4. Test Setup Preparation

Once all the previously described components of the loading frame were fabricated and assembled, the first step in the test setup was to fill the pipe grips with the sulfur concrete. The sulfur was first crushed and mixed with the aggregate, in the amounts previously discussed. See Figure 3.19. With the empty upper pipe grip placed inside the concrete tank filled with the heat transfer fluid, the first test specimen was placed inside the pipe and vertically aligned using the metal frame shown in Figure 3.20. Embedment lengths for the upper grip ranged from 39 in. to 44 in. for most tests, but two successful tests were performed with a development length of only 32 in. The 4-in. thickness of the steel blocks was not accounted for in the development length of the bars.

Figure 3.19. Sulfur concrete mix prior to melting.

Figure 3.20. Upper pipe grip (no SC) inside heat transfer fluid tank with test bar and removable aligning frame.

The sulfur concrete mix was then placed inside the pipe and melted. Since air voids were removed as the sulfur melted and through the use of a form vibrator attached to the bar, sulfur concrete was added multiple times until the molten material reached the required height. At this point, the steel block was lowered into the pipe and the concrete tank heating system was turned off. The pipe was left inside the tank overnight to cool down with the insulations cages around the tank removed. Figure 3.21 shows a rendering of the test setup at this stage.

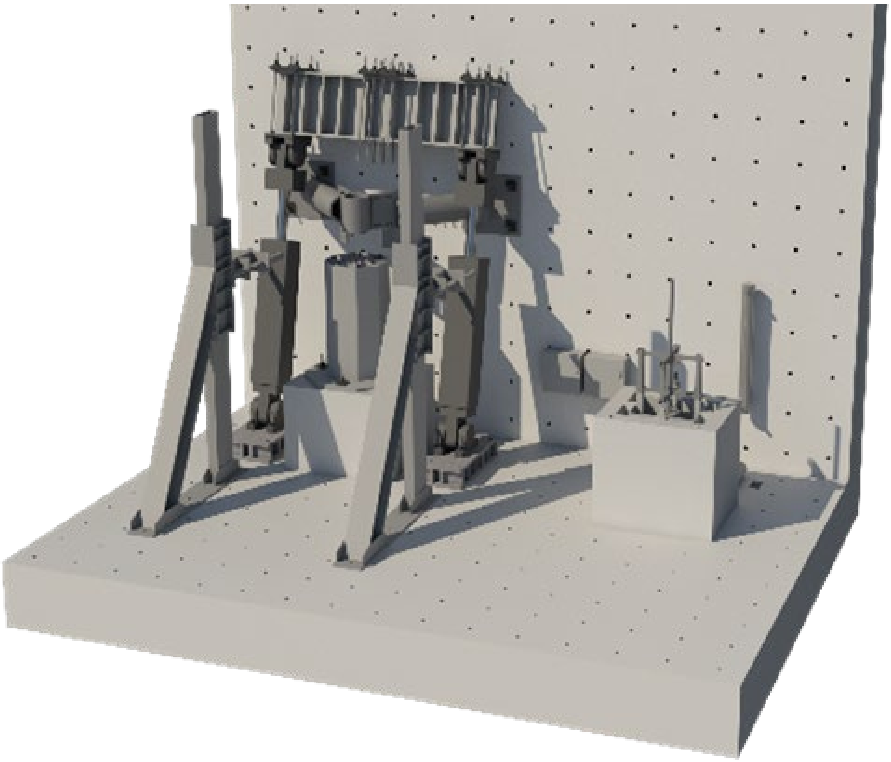

Figure 3.21. 3D rendering of stage #1 of test setup.

The following day, the aligning frame and pipe grip were removed from the tank. Oil on the outside of the pipe was then removed and the pipe was flipped vertically, with the free end of the bar pointing downward. See Figure 3.22. As shown in Figure 3.23, the pipe was then hoisted through the sleeve of the lateral restraint system until the free end of the bar reached the desired depth. Development lengths used for the lower grip ranged from 48 in. to 52 in. and did not take into account the portion of the bar inside of the steel block. Given the tight fit between the sleeve and the pipe, the sleeve helped guide and align the upper pipe with the lower pipe. The sulfur concrete mix was then added to the lower pipe in a similar manner as with the upper pipe. Once the molten sulfur reached the desired level, the steel block for the lower pipe was split open and placed around the bar. It was then bolted together and lowered until it rested on the supporting L-shaped brackets.

Figure 3.22. Transfer of upper pipe grip from heat transfer tank into loading apparatus.

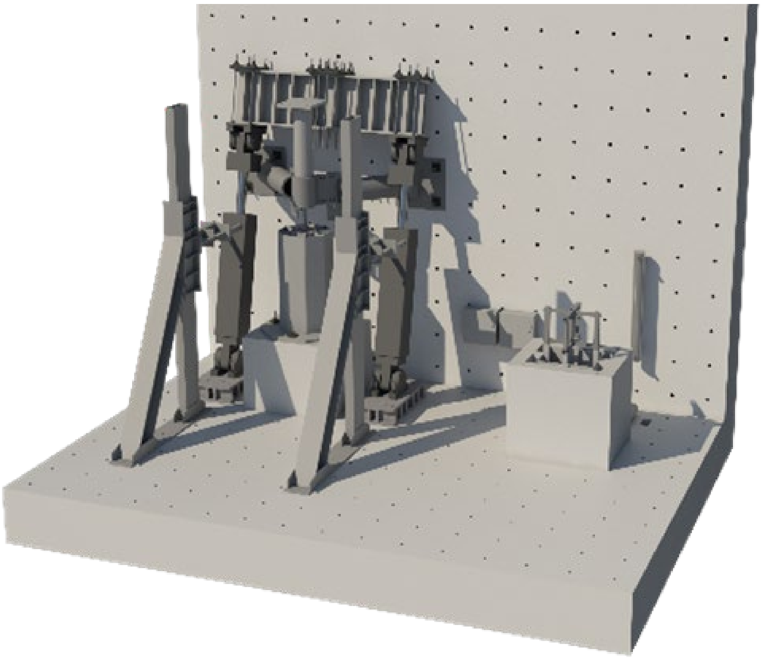

Figure 3.23. 3D rendering of stage #2 of test setup.

At this point, the spreader beam and actuators were moved into position and post-tensioned to the upper pipe base plate. See Figure 3.24. The heating system for the lower pipe grip was then turned off and the sulfur concrete was let cool overnight with the insulations cages around the tank removed. It is worth noting that, while the sulfur concrete has a very rapid strength gain, it also has a very low thermal conductivity. Hence, the outer region of the sulfur concrete inside the pipes would cool at a faster rate than the core of the material. This phenomenon, plus the time it took for the oil around the lower pipe grip to cool, lead the researcher to wait at least 24hrs prior to testing after embedding the lower end of the bars, in order to allow for all materials to reach room temperature and ensure the sulfur concrete had gained the required strength. Two tests were performed less than 24hrs after embedding in order to test this assumption. In both cases, the bars pulled out of the sulfur concrete.

With the bars embedded into the pipe grips, the specimens were then instrumented the following day. First, the strain gages were placed on the bar's theoretical inflection points and mid-height, as described in the instrumentation section. Next, the DIC camera system was calibrated by ensuring that the cameras were focus on the specimen and by using a dual plane, dual sided calibration target plate. Multiple images were captured for different target plate locations around the bar. The horizontal distance from the back of the target plate to the face of the specimen was measured every time. A white-over-black speckle pattern was then applied to the exposed bar in order to improve the results obtained from the DIC analysis. A total of four punch marks were then made on the vertical ribs of the bar at the theoretical inflection points in order to mark the location where the four steel tips of the clip gages would come in contact with the bar. These punch marks also helped the tips to remain in place when the bar elongated or expanded during testing. For a number of tests, two horizontal string pots were attached at the mid-height of the bar in order to measure out of plane displacements. The horizontal linear potentiometers on top of the sleeve were then attached and placed against the side of the upper pipe to measure their relative displacement. Finally, the orthogonal pairs of inclinometers on the upper and lower pipes and loading beam were installed. See Figure 3.25 for a typical instrumented test bar.

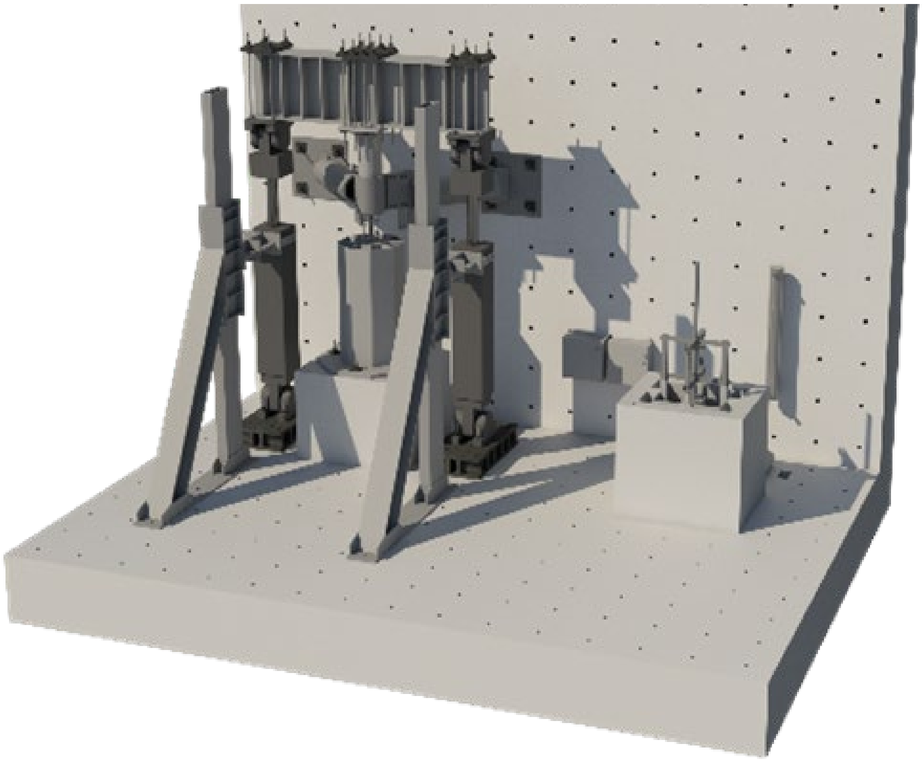

Figure 3.24. 3D rendering of stage #3 of test setup.

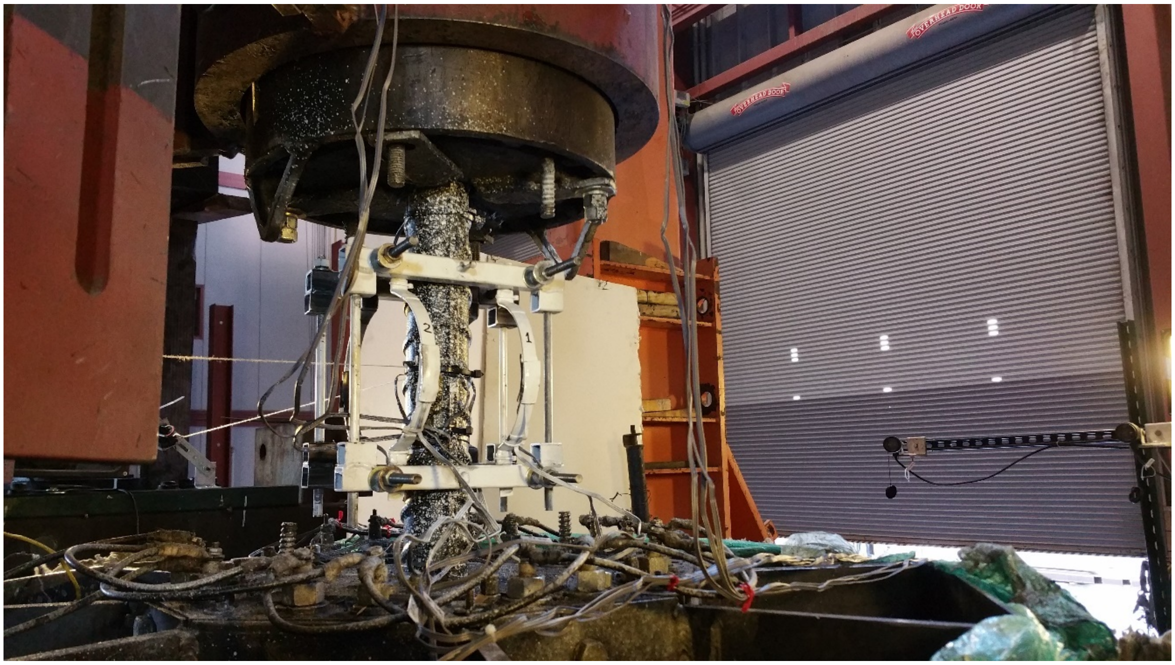

Figure 3.25. Typical fully instrumented test bar.

With all the instrumentation installed, an overall system check was performed in order to balance and shunt the strain gages and ensure all instrumentation was function properly. This was the last step before beginning testing. Once testing was completed with the low-cycle fatigue fracture of the bar, the spreader beam was detached from the upper pipe grip so that the pipe could be removed and placed inside the concrete heating tank. This was the final stage of the test setup.

The same processes were then repeated for the next test, beginning by re-melting the sulfur inside the upper pipe grip and pulling out the fractured bar from the pipe. A new bar was then embedded into the highly confined sulfur mix. This proved to be the most challenging aspect of the experimental work and different approaches were taken to try and perform this task as efficiently as possible. One of those approaches included cutting the bar's end into a spear head to help drive the bar into the sulfur concrete. See Figure 3.26.

This proved effective and was employed for most of the tests for both ends of the bars. The length of the spear head was not accounted for in the embedment length of the bar. However, even with this modification, the embedding process continued to be a challenge as large loads were required to push the bars into the highly confined sulfur concrete.

Figure 3.26. Bar end cut into spear head.

In some cases, the bars would buckle while embedding them and needed to be replaced. A solution for this was the use of a two-person, 4-in. diameter auger. The auger would be used to a depth equal to the desired embedment length after the tested specimens and steel blocks were removed from the pipes and while the sulfur was molten. Any aggregate or sulfur material removed by the auger was replaced before placing the steel blocks back into the pipe. Next, a third approach used to help embed the bars was to heat the bar to about 300°F, prior to embedding it, in order to prevent the sulfur from hardening around the bar, which further complicated the embedding process. In order to heat the bar, a pipe with a 2-3/8 in. inside diameter was sealed from one end and placed inside the heat transfer fluid inside the concrete tank; the bar would then be placed inside the sealed pipe to heat up. Once the bar reached the desired temperature it was embedded into the upper pipe grip with the help of a pneumatic post driver, using the steel block and steel frame to keep the bar leveled. Once the bar reached the desired embedment length, the form vibrator was attached to the bar and used to consolidate the sulfur concrete around the bar and remove any air voids. The heating system was then turned off and the pipe let cool overnight.

A similar procedure with the auger was employed for the lower pipe. After re-melting the sulfur and removing the steel blocks and fractured specimen, the auger was used to loosen the sulfur concrete mix. As with the upper pipe, any material removed by the auger was replaced before placing the steel blocks back into the pipe. The free end of the bar was heated in the same manner as previously explained prior to embedding it. The upper pipe would then be lowered through the lateral restraint sleeve until the spreader beam could be attached to the base plate of the upper pipe. At this point, the actuators were used, in lieu of the post driver, to embed the bar. The form vibrator was also used to consolidate the sulfur concrete around the embedded bar. This concluded the third stage of the test setup. The remaining procedures were the same as previously explained. After trials and errors with the embedding of the bars, the approximate time between the start of work for each test specimen and testing was approximately one week.

3.5. Properties of Steel Reinforcing Bars

3.5.1 Geometric Properties

Given the important role the surface geometrical properties of steel reinforcement have on fatigue life, multiple samples of bars from each MFR were analyzed. The main geometric bar properties are summarized in Table 3.2 and Table 3.3. Geometrical properties of bar deformations are illustrated in Figure 3.28 and Figure 3.27. The measurements were taken on different sections with different characteristics from different bars using multiple methods. The measuring methods range from the simple use of a micro-meter to more advanced, such as the use of high-resolution two-dimensional images from a laser scanner and three-dimensional scanning of the samples. Sample 3D models are shown in Figure 3.28. Measurements were taken according to ASTM A706, with the exception of lug radius, *r*, for which there are no guidelines in the standard. Lug radii were measured using a similar procedure as the one used by Fei and Darwin (1999) and Helgason et al. (1976). As discussed in Section 2.3.3 and illustrated in Figure 3.27, the specimen has two lugs on each side with different surface geometry. Even on the same deformation, different lugs can have different properties, leading to different stress concentrations.

The average spacing of deformations, s_r, was determined by measuring the length of a minimum of 10 spaces and dividing the length by the number of spaces included in the measurement. The measurement was taken from a point on the deformation at the beginning of the first space to a corresponding point on a deformation after the last space. Measurements were not made over a bar containing bar marking symbols.

The average deformation height, h_r, was determined from at least two typical deformations based on three measurements per deformation, one at the center of the overall length and the other two at the quarter points of the overall length. As noted by previous research (see Section 2.3.3), one of the main parameters affecting the fatigue life of a reinforcing bar is the *r/h* ratio. Measurements from the tested bars result in a ratio of 1.51 for MFR-A and 2.13 for MFR-B. Both these values are higher than the 1.25 value suggested by Jhamb and Mac Gregor (1974b) but meet the recommendations by ACI Committee 215 (1992) who suggest a value within 1 and 2, with values higher than 2 not having much effect on the fatigue life of bars. Per ASTM A706 guidelines, given that the ends of the deformations terminated in a rib, the width of the rib, g_r, was taken as the gap between the ends of the deformations, see Figure 3.28a. Geometrical requirements from ASTM A706 as well as measured properties are summarized in Table 3.2.

Table 3.2. Bar geometrical requirements per ASTM A706 and measured properties.

	Diameter, d_b (in)	Cross-Sectional Area, A_b (in^2)	Lug Spacing, s_r (in)	Lug Height, h_r (in)	Lug Gap, g_r (in)
ASTM	2.257	4.00	1.58 (max)	0.102 (min)	0.864 (max)
MFR-A	2.17	3.70	1.39 - 1.44	0.108 - 0.130	0.309 - 0.502
MFR-B	2.15	3.63	1.07 – 1.11	0.112 – 0.149	0.214 – 0.241

Table 3.3. Lug geometrical properties.

	Side	R_a (in)	R_b (in)	h_r (in)	R_a/h_r	R_b/h_r	Critical r/h
MFR-A	1	0.301	0.229	0.111	2.71	2.06	1.51
	1	0.231	0.243	0.109	2.12	2.23	
	2	0.341	0.151	0.100	3.41	1.51	
	2	0.221	0.326	0.107	2.07	3.05	
MFR-B	1	0.188	0.347	0.116	1.62	2.99	2.13
	1	0.364	0.229	0.106	3.44	2.16	
	2	0.186	0.329	0.111	1.67	2.96	
	2	0.435	0.243	0.114	3.81	2.13	

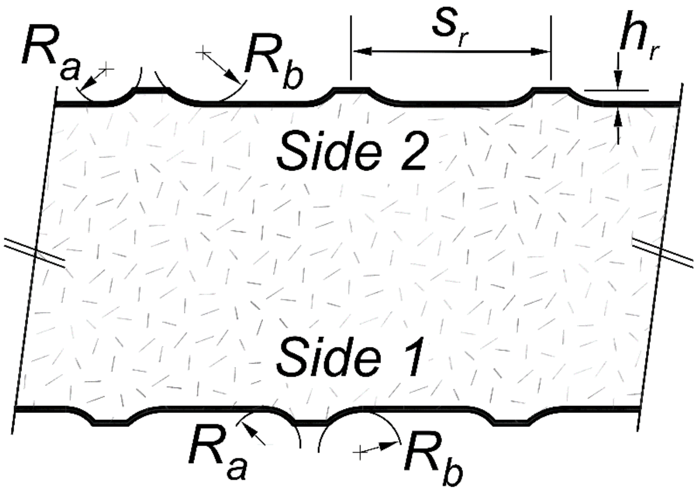

Figure 3.27. Illustration of lug geometry.

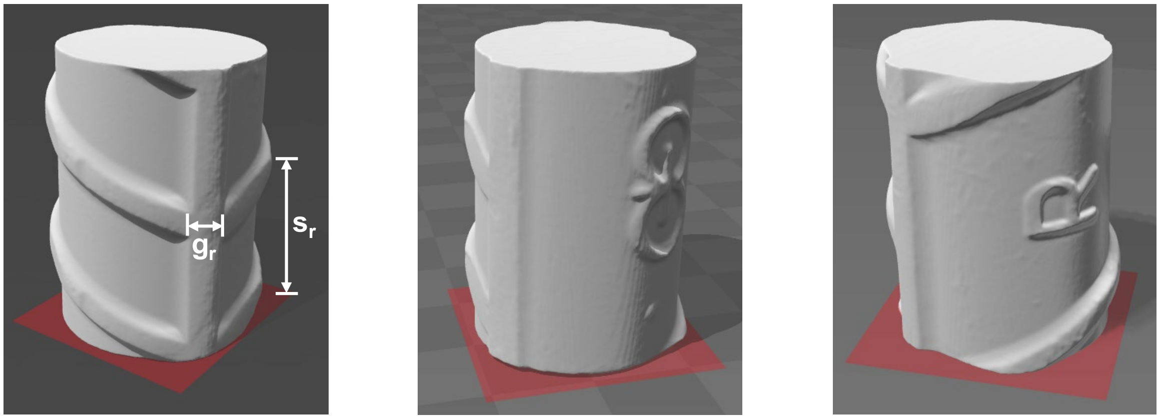

(a) (b) (c)

Figure 3.28. 3D Scanning of bar section: (a) With no markings; (b) With MFR marking and no transverse deformations on one side; (c) With MFR marking and transverse deformations on both sides.

3.5.2 Material Properties

To obtain the material properties of the steel reinforcing bars, a total of four monotonic tensile tests were performed on ASTM A706 Grade 60 bars from each of the two manufacturers (MFR-A and MFR-B). Testing procedures were according to ASTM E8

(2016) using a closed-loop active hydraulic SATEC universal testing machine. Complete monotonic stress-strain responses of the bars, up to fracture, were recorded for all specimens. Strain measurements were obtained using both a 2-in. gage length extensometer and the previously described in-house designed clip gage. Stresses were obtained by dividing the force exerted by the machine, by the nominal bar area. The results of all four tests are plotted in Figure 3.29 and the material properties tabulated in Table 3.4. All specimens exhibited a clear yield plateau and the average yield stresses were obtained by averaging the stresses over the yield plateau of each specimen, between the upper yield stress and up to the onset of strain hardening. The average yield stress, f_y, of the bars from MFR-A was 71.3 ksi which, although high, satisfies the ASTM A706 requirements for Grade 60 bars ($f_y \leq 78$ ksi). On the other hand, the average yield stress for the two MFR-B bars was 60.2 ksi, barely exceeding the minimum strength of 60 ksi prescribed in the A706 standard. The upper and lower yield strengths are also tabulated, per ASTM E8, see Table 3.4. The point at which the yield plateau ends and strain hardening begins was not clear for all tests. For specimen MFR-A-1, a dip occurs in the yield plateau followed by a sharp increase in slope into the relatively smooth strain-hardening region. For the rest of the specimens, there is no dip and the change in slope occurs gradually. Therefore, to estimate the strain at which hardening occurs, a line corresponding to the slope of the strain-hardening smooth curve is fitted and extended until it intersects the yield plateau region. As shown in Figure 3.30, the intersection of both lines is taken as the point where strain-hardening begins. The average tensile strength, f_u, for MFR-A bars was 98.4 ksi ($1.38 f_y$) and 85 ksi ($1.41 \cdot f_y$) for MFR-B bars, thus meeting the ASTM requirement for the tensile-to-yield strength (*T/Y*) ratio $f_u \geq 1.25 \cdot f_y$. The average engineering uniform strain, ε_{su}, equaled 12.4% for MFR-A and 13.1% for MFR-B. Per ASTM E8, the uniform strain corresponds to the strain at maximum force sustained by the bar just prior to necking and includes both elastic and plastic strains. Each individual uniform strain value was determined by zooming in the region close to the tensile strength of the bar. A centered moving average filter was used to smooth the stress and strain data using different increasing values for the filter window size, until a clear signal with a definite peak could be obtained. Figure 3.31 shows a comparison of the unfiltered and filtered data. The power term, *P*, used to obtain the appropriate slope at the initiation of strain-hardening is also tabulated. The elastic energy, W_y, defined as the area under the monotonic curve up to ε_y, is numerically integrated and shown in Table 3.4.

The equivalent carbon content, from the mill certificates provided by the manufacturers, is tabulated in Table 3.5. Both equivalent carbon contents meet the 0.55% limit established by ASTM A706, with 0.470% and 0.436%, for MFR-A and MFR-B, respectively.

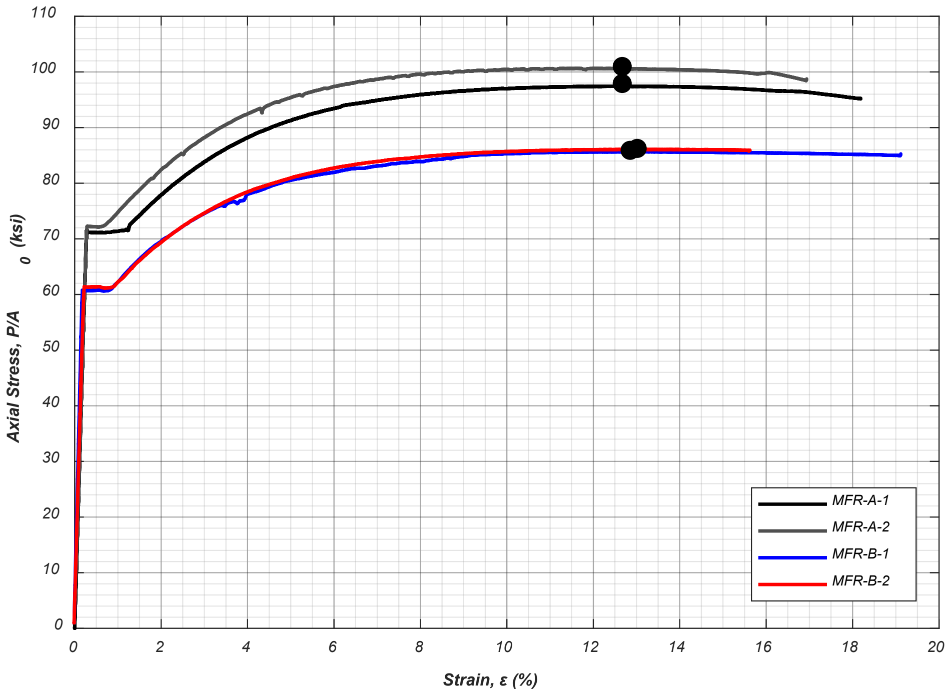

Figure 3.29. Monotonic tensile tests of four ASTM A706 Grade 60 bars from two manufacturers in engineering coordinates.

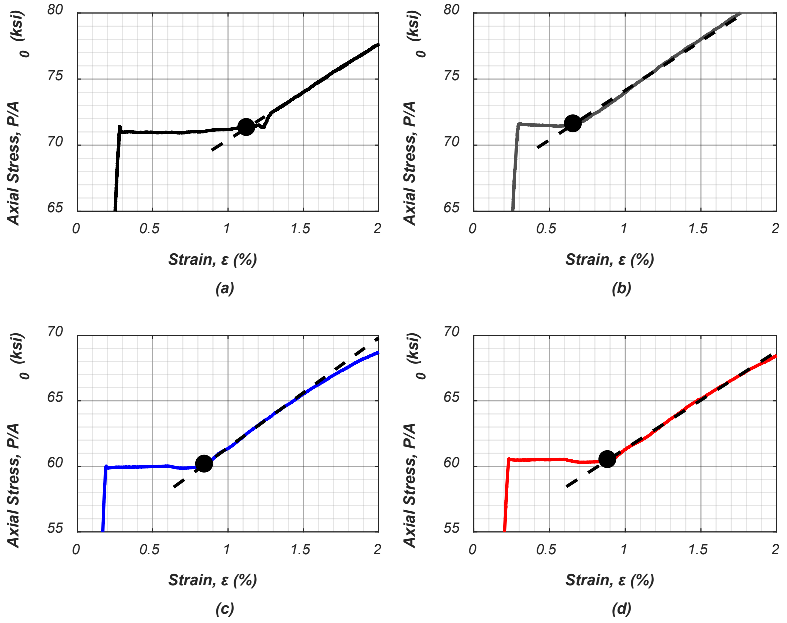

(a)

(b)

(c)

(d)

Figure 3.30. Location of strain-hardening from monotonic tensile curves: (a) MFR-A-1; (b) MFR-A-2; (c) MFR-B-1; (d) MFR-B-2.

Table 3.4. Material properties from monotonic tensile tests in engineering coordinates.

	MFR-A-1	MFR-A-2	MFR-B-1	MFR-B-2
Upper f_y, ksi	71.4	71.6	60.6	60.6
Lower f_y, ksi	70.9	71.5	59.9	60.3
Average f_y, ksi	71.0	71.6	59.9	60.5
ε_y, %	0.28	0.3	0.19	0.23
ε_{sh}, %	1.01	0.660	0.847	0.887
f_u, ksi	96.8	99.9	84.8	85.2
ε_{su}, %	12.7	12.0	12.9	13.2
P	3.2	3.6	3.2	3.4
T/Y Ratio	1.36	1.40	1.42	1.41
W_y (in-kip/in3)	10.2	10.9	5.84	7.36

Table 3.5. Chemical composition and equivalent carbon content (C.E.) of reinforcing steel bars.

	MFR-A	MFR-B
C, %	0.29	0.26
MN, %	0.91	0.98
P, %	0.02	0.007
S, %	0.023	0.021
SI, %	0.29	0.21
CU, %	0.44	0.21
NI, %	0.13	0.08
CR, %	0.16	0.09
MO, %	0.03	0.02
SN, %	0.014	-
V, %	0.043	0.049
NB, %	0.003	-
AL, %	0.003	-
CB, %	-	0.001
C.E.	0.47	0.436

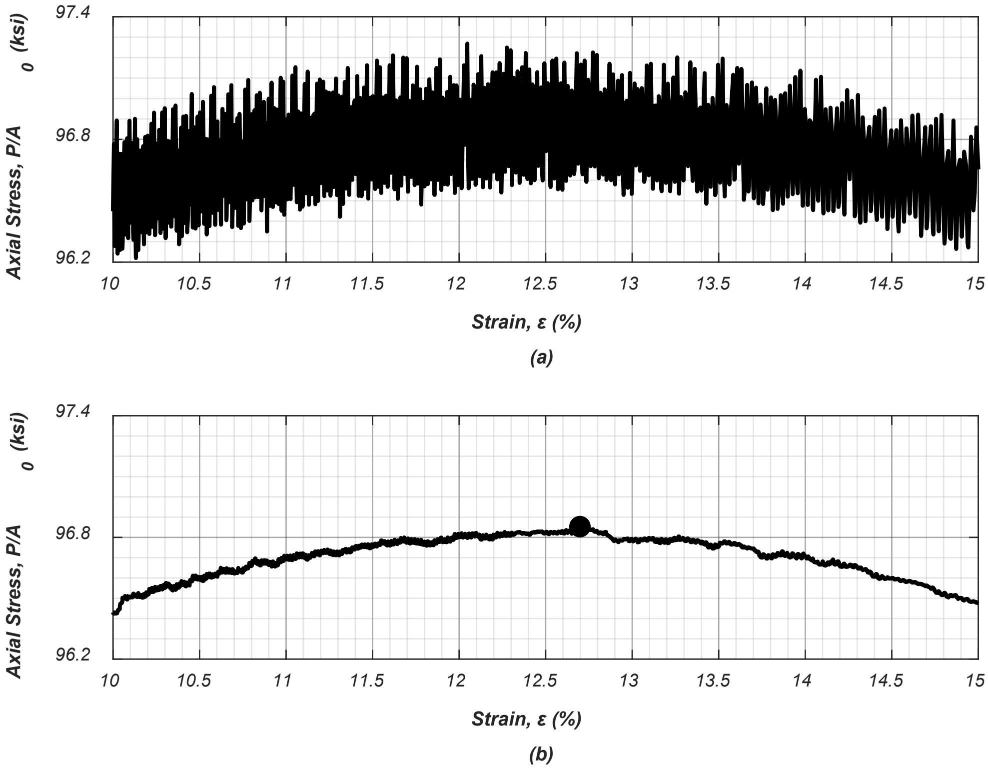

Figure 3.31. Uniform strain determination from monotonic tensile tests: (a) Unfiltered data for MFR-A-1; (b) Filtered data for MFR-A-1.

3.6. Loading Protocols

3.6.1 Development of the Earthquake Smeared Strain History Protocol

To develop a strain history for use in the bar buckling test apparatus, a strain history was derived from the experimental results of a full-scale bridge column tested at the single axis Large High-Performance Outdoor Shake Table (LHPOST) at the University of California - San Diego (Schoettler, Restrepo, Guerrini, Duck, & Carrea, 2012), see Figure 3.32. The longitudinal reinforcement of the 4-ft. diameter by 24 ft. tall column consisted of ASTM A706 Grade 60 18#11 bars with the transverse reinforcement provided by double ASTM A706 Grade 60 #5 hoops spaced at 6 in. on center.

Figure 3.32. Overall view of full-scale reinforced concrete column tested at the Large High-Performance Outdoor Shake Table at the University of California – San Diego (Schoettler et al., 2015).

Local axial strains of the column longitudinal reinforcement were monitored using 5mm long electrical foil strain gages installed on two reinforcing bars at both the East and West faces of the column (total of four bars), where tensile and compressive strains were expected to be the greatest. Column smeared longitudinal strains and curvatures were computed from the vertical displacement sensors placed on the North and South faces (perpendicular to the direction of shaking). The vertical displacement sensors were spaced at 8 in. apart, starting 2 in. above the column base and extending 48 in. (i.e. one column diameter). Above this, 24 in. and 31 in. spacings were used, see Figure 3.33 and Figure 3.34. The 2-in. spacing at the column base was left to ensure that the fixed-end rotation caused by strain penetration of the column bars anchored in the foundation would not have an effect on the curvatures and strains derived from these sensors. The fixed-end rotation was monitored using two pairs of vertical displacement sensors, which spanned the horizontal crack expected to develop at the column-foundation interface (Schoettler et al. 2015).

The selected input ground motions for the experimental work are listed in Table 3.6. The objective of the first six tests was to achieve desired column lateral displacement demands in terms of target displacement ductilities with the first three input motions selected from the 1989 Loma Prieta earthquake and the fourth record from the Takatori station during the 1995 Kobe earthquake. While the original loading protocol consisted of only six input ground motions, due to the significant observed structural integrity after the planned test sequence, the scope was expanded and an additional four tests were conducted and was ended after a number of longitudinal bars had fractured following buckling or had buckled near the column bas where the plastic hinge developed, see Figure 3.35.

Figure 3.33. Curvature, shear, and fixed-end rotation linear potentiometers of the full-scale column: (a) Instrumented South face (b) Plan view of column and linear potentiometers; (c) Instrumented North face (Schoettler et al., 2015).

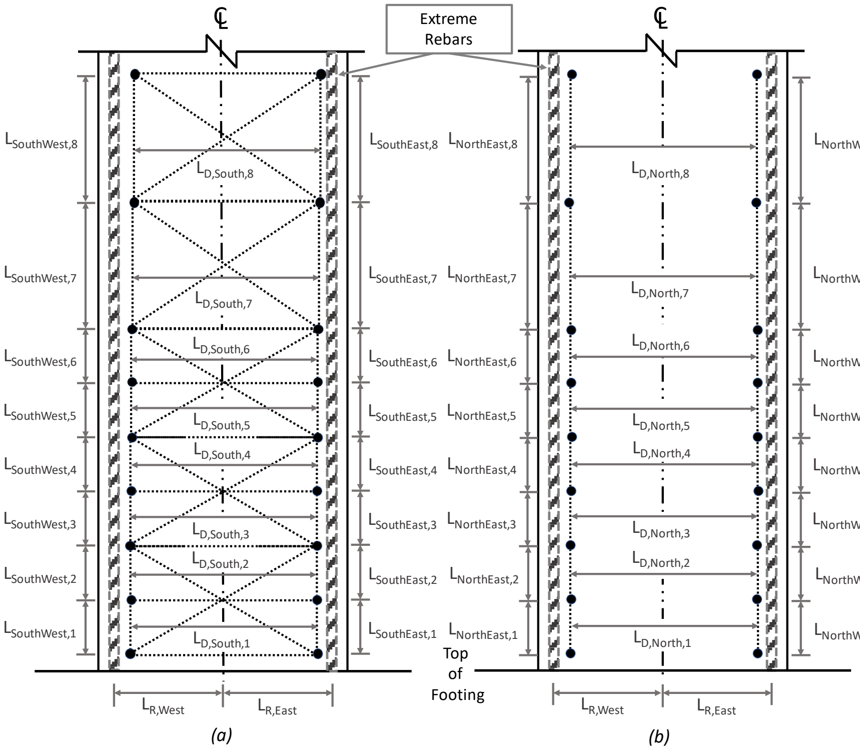

Figure 3.34. Schematics of column deformation panels on: (a) South face; (b) North face.

Table 3.6. Ground motion selection for experimental test of full-scale bridge column (Schoettler et al., 2015).

Test	Earthquake	Date	Moment Magnitude	Station	Scale Factor	Target Displacement Ductility
EQ1	Loma Prieta	10/18/1989	6.9	Agnew State Hospital	1.0	1.0
EQ2	Loma Prieta	10/18/1989	6.9	Corralitos	1.0	2.0
EQ3	Loma Prieta	10/18/1989	6.9	LGPC	1.0	4.0
EQ4	Loma Prieta	10/18/1989	6.9	Corralitos	1.0	2.0
EQ5	Kobe	01/16/1995	6.9	Takatori	-0.8	8.0
EQ6	Loma Prieta	10/18/1989	6.9	LGPC	1.0	4.0
EQ7	Kobe	01/16/1995	6.9	Takatori	1.0	Not Applicable
EQ8	Kobe	01/16/1995	6.9	Takatori	-1.2	Not Applicable
EQ9	Kobe	01/16/1995	6.9	Takatori	1.2	Not Applicable
EQ10	Kobe	01/16/1995	6.9	Takatori	1.2	Not Applicable

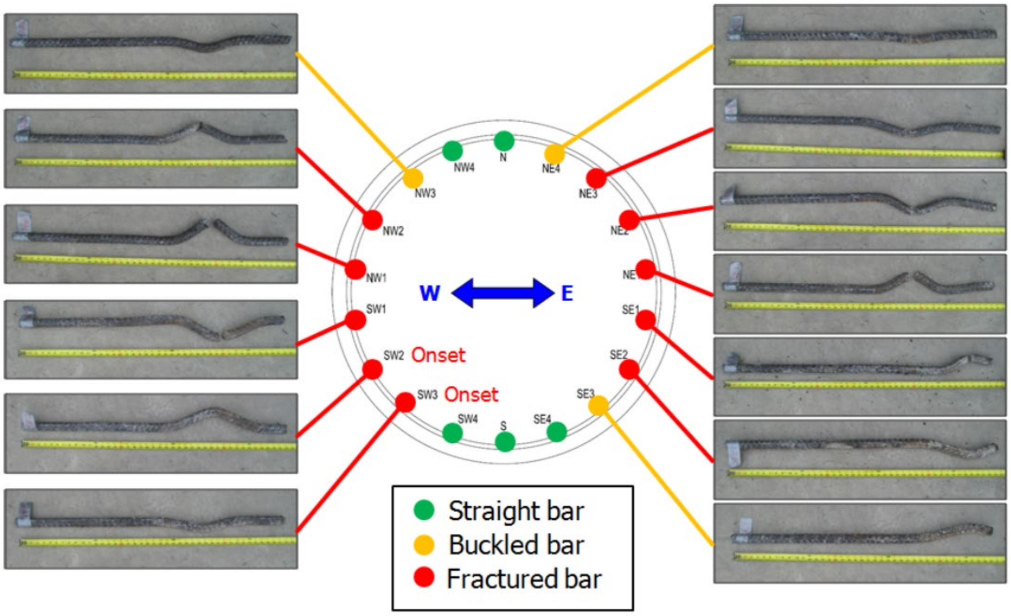

Figure 3.35. Longitudinal bars extracted from column after completion of experimental work (Schoettler et al., 2015).

The classical way to obtain longitudinal strains and strain histories from one such column, has been to compute an equivalent plastic hinge length, L_p, in the following form,

$$L_p = \alpha \cdot L + \beta \cdot f_{ye} \cdot d_{bl}$$ **Equation 3-1**

where L is the column shear span, f_{ye} is the measured yield strength and d_{bl} is the nominal diameter of the column longitudinal bar. The first term of Equation 3-1 is the fraction of the plastic hinge length due to the spread of plasticity along the column height, whereas the second term represents the fraction of the plastic hinge length due to strain penetration. Supported on the experimental work carried out in columns at the University of Canterbury in the late 1970s and 1980s, (Paulay and Priestley, 1992) proposed $\alpha = 0.08$ and $\beta = 0.15$/ksi. These coefficients have been adopted by Caltrans SDC (2019).

Figure 3.36a depicts a laterally loaded column that has been displaced well past yielding to a displacement Δ. Figure 3.36b and Figure 3.36c show the bending moment diagrams and corresponding curvature diagrams at two stages of loading: (i) at first yield and (ii) at a stage well into the plastic range where a plastic hinge has developed in the column. Figure 3.36d shows the idealized curvature diagram used by Paulay and Priestley (1992) to define the equivalent plastic hinge length for the second loading stage. In this approach, the maximum curvature in the idealized curvature diagram is made equal to the peak curvature, ϕ_k, computed for the test column at a stage of loading well into the plastic range. This assumption makes it possible to determine coefficients α and β and the equivalent plastic hinge length L_p (Restrepo et al. 2006).

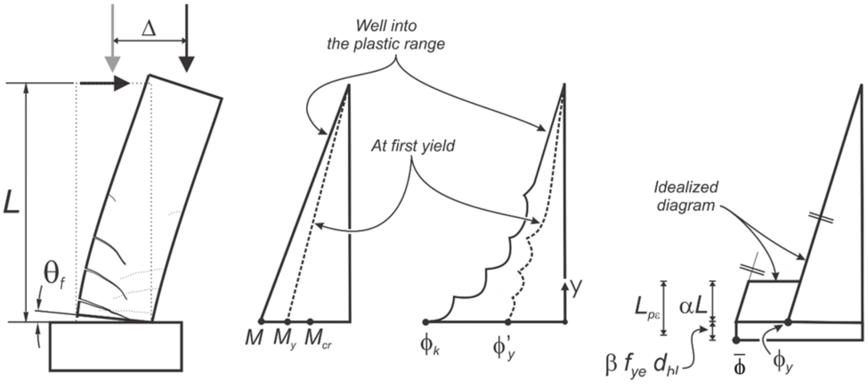

(a) Column (b) BMD (c) Curvature diagram (d) Idealized curvature diagram

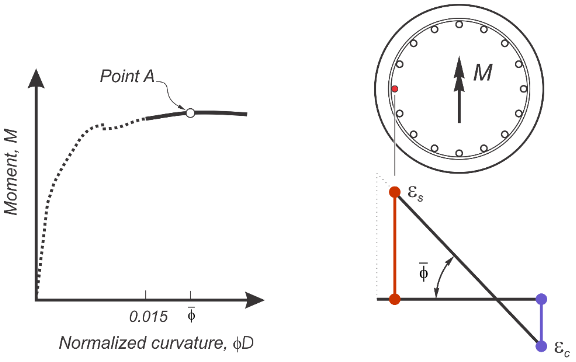

(e) Domain used in the theoretical moment-curvature response (f) Cross section, curvature and key strains at point A

Figure 3.36. Definition of smeared curvature-based equivalent plastic hinge length, $L_{p\varepsilon}$.

Figure 3.37 compares coefficients α and β calculated using the approach proposed by Paulay and Priestley for the test column with the coefficients proposed by these researchers. The values of coefficient α calculated for the experiment, see Figure 3.37a, increase with the drift ratio (or with the displacement ductility). That is, as the column undergoes further plastic displacements, the portion of the equivalent plastic hinge length spreading over the column increases as the displacement ductility increases. The correlation of coefficient α with ductility had also been pointed out by Restrepo et al. (2006). This means that a constant coefficient α seems to be only a fair approximation. The values of coefficient β calculated for the test column, see Figure 3.37b, are largely uncorrelated with the imposed drift ratio (or displacement ductility), an observation also made by Restrepo et al. (2006), which justifies the use of a constant value for this coefficient. Nevertheless, in this test, the values of coefficient β are much lower than that those recommended by Paulay and Priestley. Restrepo et al. (2006) had reported values of β greater than the proposed value of $\beta = 0.15$/ksi.

The significant correlation between coefficient α with displacement ductility implies that the equivalent plastic hinge length, L_p, is also correlated with displacement ductility, something that is not recognized in Equation 3-1, see Figure 3.38.

The development of longitudinal bar strain histories computed with the approach proposed by Paulay and Priestley of using a ductility independent equivalent plastic hinge length distorts the strain amplitudes at low and at large displacement ductilities, which will have an effect in the prediction of the strain amplitudes to determine the life of a bar. A more suitable approach is to calculate longitudinal strain histories using a smeared strain compatible equivalent plastic hinge length, $L_{p\varepsilon}$. In this approach the equivalent plastic hinge experiences a smeared curvature, $\overline{\phi} < \phi_k$, see Figure 3.36d, such that the test tensile strain of the extreme longitudinal bar smeared recorded in the column smeared over length $L_{p\varepsilon}$ and the test compressive extreme fiber compressive strain smeared over length $L_{p\varepsilon}$ equal the strains computed from a moment-curvature analysis at curvature $\overline{\phi}$, Figure 3.36.

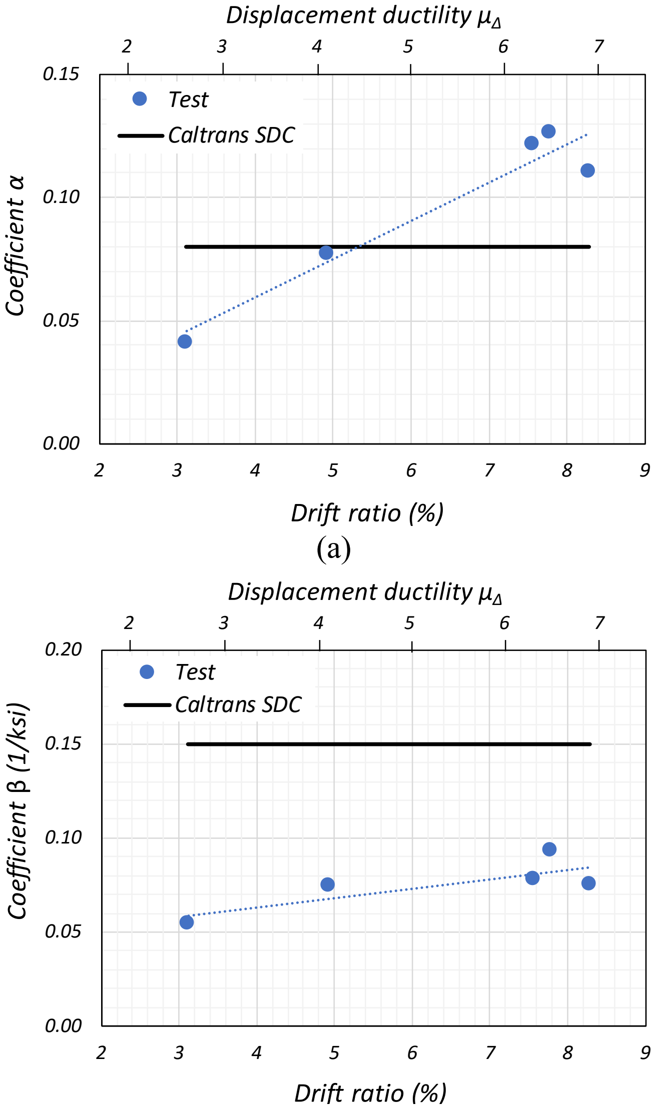

(a)

(b)

Figure 3.37. Comparison of equivalent plastic hinge coefficients α and β

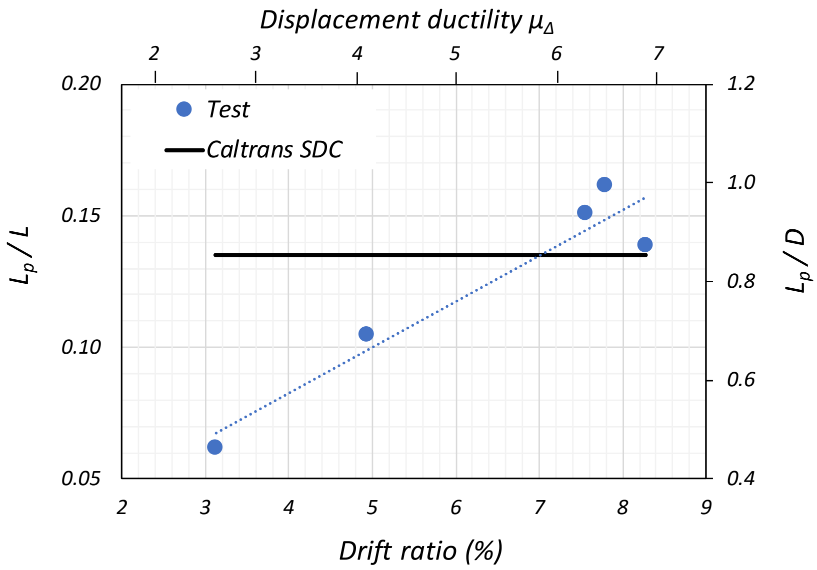

Figure 3.38. Comparison of equivalent plastic hinge lengths.

An optimization procedure was used to determine coefficients $\alpha = 0.248$ and $\beta = 0.15/\text{ksi}$ for the smeared curvature-based equivalent plastic hinge length, resulting in $L_{p\varepsilon} = 0.3L = 1.82D$, or $L_{p\varepsilon} = 2.24L_p$. As expected, the use of the smeared curvature and smeared strains results in length $L_{p\varepsilon}$ being significantly greater than length L_p and significantly greater than $0.5D$, a value often cited for the equivalent plastic hinge length, which clearly indicates these two equivalent plastic hinge lengths should not be used interchangeable. The advantage of the smeared curvature equivalent plastic hinge length is that it can be used to predict very closely the test tensile and compressive strains smeared over the length $L_{p\varepsilon}$ for the entire range of drift ratios and displacement ductilities, see Figure 3.39.

Figure 3.40a plots the smear strain histories computed using length $L_{p\varepsilon}$ for an extreme longitudinal bar in the test column reported by Schoettler et al. (2015) during the first input ground motion tests EQ1-EQ8. Only the most relevant reversed cycles were extracted (solid black lines) from the complete strain history, and then simplified even further (dashed black line), see Figure 3.40b to be used as strain targets in the random test protocol, see Figure 3.40c. A series of three elastic cycles with an amplitude equivalent to half the expected yield strain of the bars were added to the beginning of the beginning of the simplified strain history.

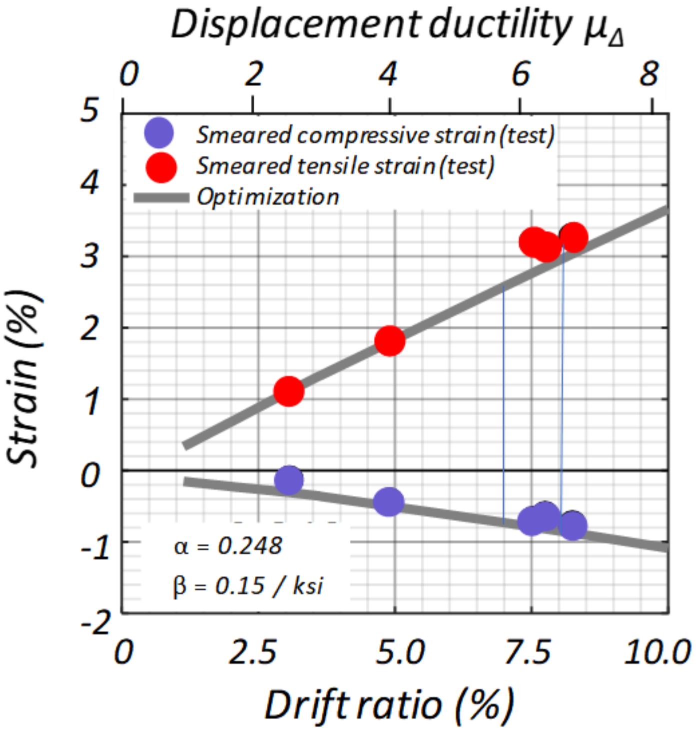

Figure 3.39. Equivalent plastic hinge coefficients α and β computed for the column reported by Schoettler et al. (2015) using the smeared curvature equivalent plastic hinge approach.

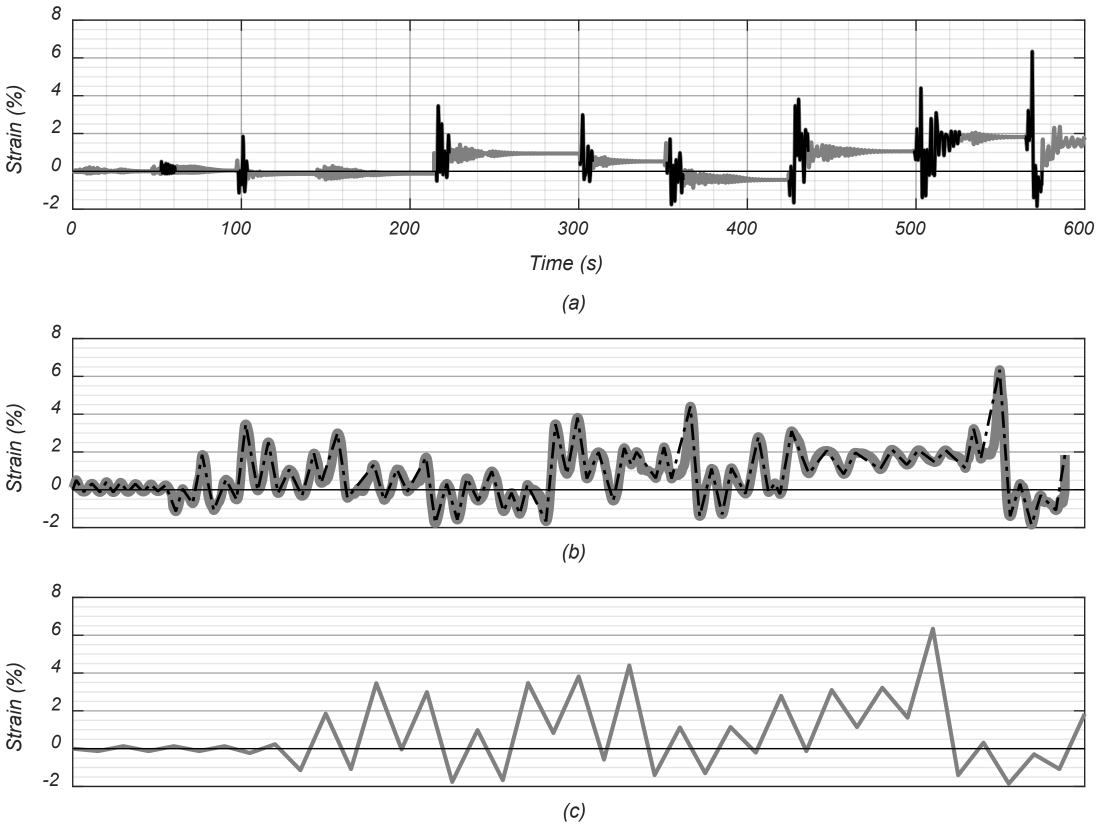

Figure 3.40. Strain history of long. bars from testing of full-scale bridge column: (a) Complete strain history; (b) Condensed strain history; (c) Simplified strain history

3.6.2 Mean Strain History Protocol

A series of constant amplitude tests were also performed for the various aspect ratios used in the experimental work. These tests were performed to establish a relationship between deformation amplitude and the number of cycles to failure, to allow for comparison with current fatigue models. Results from these constant amplitude tests can be compared with results from previous fatigue testing on steel reinforcement. All constant amplitude strain histories began with a series of three elastic cycles with an amplitude equivalent to half the expected yield strain of the bars. After the elastic cycles, constant amplitude cycles with strain amplitudes ranging from 2.8% to 4.5%, were used until fatigue failure of the specimens. The complete histories are shown in Figure 3.41.

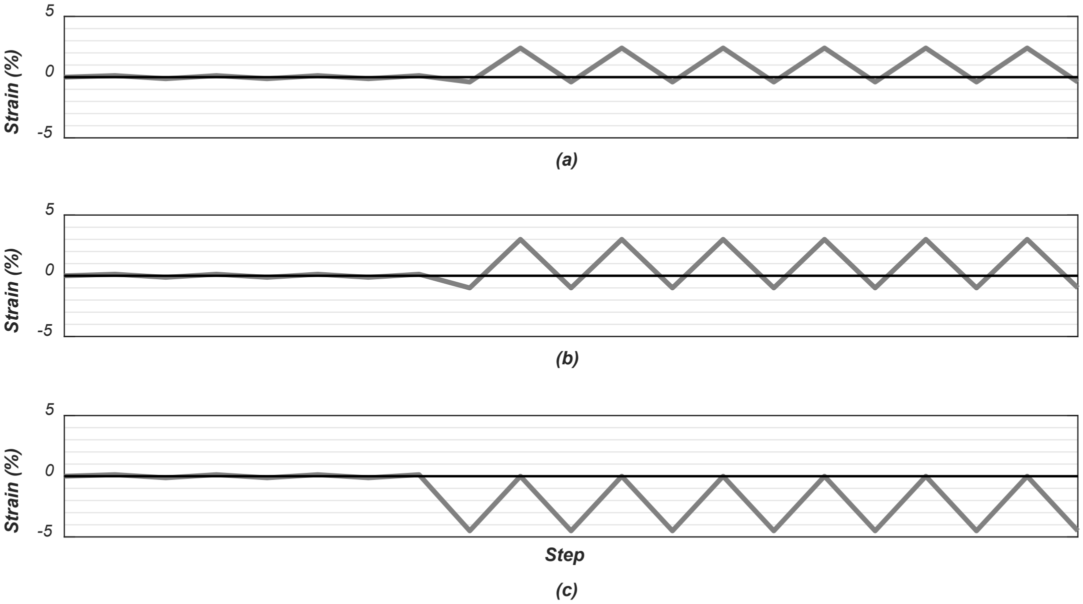

Figure 3.41. Constant amplitude strain histories.

3.7. Test Results

A total of thirty-five tests were performed. Table 3.7 summarizes the aspect ratios, test types, outcome of the tests, as well as notes about each test. Steel reinforcing bars from two different manufactures were used for the experimental work. Specimen01 thru Specimen29 were from the same batch from manufacturer A (MFR-A), while Specimen30 thru Specimen35 were from the same batch from manufacturer B (MFR-B).

Table 3.7. Summary of experimental work.

	Aspect Ratio (s/d_b)	MFR	Test Type	Test Outcome	Notes
SPECIMEN01	8.56	A	Monotonic	Fractured Bar	Strain data from SG
SPECIMEN02	5.56	A	Monotonic	Fractured Bar	Strain data from SG
SPECIMEN03	10.00	A	Cyclic - RH	Fractured Bar	Strain data from SG
SPECIMEN04	7.78	A	Cyclic - RH	Fractured Bar	Strain data from SG
SPECIMEN05	7.78	A	Cyclic - RH	Fractured Bar	Strain data from SG
SPECIMEN06	8.00	A	Cyclic - RH	Fractured Bar	Strain data from vertical SP
SPECIMEN07	7.78	A	Cyclic - RH	Bar Pullout	Strain data from vertical SP
SPECIMEN08	7.89	A	Cyclic - RH	Duct Pullout	Strain data from vertical SP
SPECIMEN09	7.56	A	Cyclic - RH	Bar Pullout	Strain data from vertical SP
SPECIMEN10	8.36	A	Cyclic - RH	Fractured Bar	Strain data from vertical SP
SPECIMEN11	8.00	A	Cyclic - RH	Fractured Bar	Strain data from CG / CG leg slipped on second to last
SPECIMEN12	8.22	A	Cyclic - RH	Bar Pullout	Strain data from (2) CG
SPECIMEN13	8.00	A	Cyclic - RH	Fractured Bar	Strain data from (2) CG
SPECIMEN14	8.06	A	Cyclic - CA	Fractured Bar	Strain data from (2) CG
SPECIMEN15	8.00	A	Cyclic - CA	Fractured Bar	Strain data from (2) CG
SPECIMEN16	8.00	A	Cyclic - CA	Fractured Bar	Strain data from (2) CG
SPECIMEN17	8.11	A	Cyclic - CA	Fractured Bar	Strain data from (2) CG / CG pushed out by buckled
SPECIMEN18	8.00	A	Cyclic - CA	Fractured Bar	Strain data from (4) CG
SPECIMEN19	8.00	A	Cyclic - RH	Fractured Bar	Strain data from (4) CG
SPECIMEN20	6.00	A	Cyclic - CA	Fractured Bar	Strain data from (4) CG
SPECIMEN21	6.00	A	Cyclic - CA	Fractured Bar	Strain data from (4) CG
SPECIMEN22	6.00	A	Cyclic - CA	Fractured Bar	Strain data from (4) CG / No SG at mid-height
SPECIMEN23	6.00	A	Cyclic - CA	Fractured Bar	Strain data from (4) CG
SPECIMEN24	6.00	A	Cyclic - RH	Fractured Bar	Strain data from (4) CG
SPECIMEN25	8.00	A	Cyclic - CA	Fractured Bar	Strain data from (4) CG
SPECIMEN26	8.00	A	Cyclic - CA	Fractured Bar	No instrumentation used
SPECIMEN27	1.67	A	Cyclic - CA	Fractured Bar	Strain data from SG / Bar buckled while embedding -
SPECIMEN28	1.50	A	Cyclic - CA	Bar Pullout	Strain data from SG
SPECIMEN29	1.50	A	Cyclic - CA	Fractured Bar	Strain data from SG / Gages not reliable on last tensile
SPECIMEN30	8.11	B	Cyclic - RH	Fractured Bar	Strain data from (4) CG / CG slipped mid-test
SPECIMEN31	7.89	B	Cyclic - CA	Fractured Bar	Strain data from (4) CG
SPECIMEN32	8.00	B	Cyclic - CA	Fractured Bar	Strain data from (4) CG

* CG – Clip gage; SG – Strain gage; SP – String potentiometer.

The unsupported length of $8d_b$ was chosen from the test results of the full-scale bridge column tested at UC San Diego and sponsored by Caltrans. By visually inspecting the recovered buckled bars from the tested column, it was noticed that the distance between inflection points, d_{POI}, corresponded to about $4d_b$, resulting in an aspect ratio, s/d_b, of 8 between fixed ends for a buckled bar in double curvature. An unsupported length of $6d_b$ was also chosen as it replicates a commonly used spacing for the transverse reinforcement in bridge columns. A total of three tests, specimens 27 to 29, were performed with an aspect ratio equal to 1.5 to remove nonlinear geometrical effects (Restrepo-Posada, 1993).

For the commissioning of the loading apparatus, two monotonic tests were performed first to ensure the test setup was able to properly apply and transfer the loads required to fail a specimen under uniaxial tensile load. After the commissioning tests, a series of random history and constant amplitude tests were performed, with different aspect ratios, to compare the effects of buckling on the fatigue life of the bars. As previously explained, given the initial difficulties with the embedment of the bars and in collecting accurate data from cyclic loading, results from specimens 03 thru 13 are not used for analysis. Axial stress-strain responses and test pictures for all successful tests starting with Specimen14 can be found on Appendix C and Appendix D, respectively.

Figure 3.42 shows a typical axial stress vs strain response under constant amplitude cyclic loading, measured with the clip gage, of +2.4%, -0.4%. From the first three elastic cycles, with an amplitude of half the expected yield strain of the bar, the elastic modulus of elasticity, E_0, can be calculated as 29,200 ksi for this specimen. While the in-house designed clip gages were intended to accurately measure large deformations, the resolution obtained for small measurements is excellent, as proven by the good agreement of the bar's E_0 value with typical values for steel.

The effects of a larger aspect ratio and bar buckling on the fatigue life of the bars are clearly visible when comparing the cyclic response of bars with different aspect ratios tested with the same constant amplitude strain history. Figure 3.42 shows the cyclic response for Specimen16 with an unsupported length of 8d_b, while Figure 3.43 shows the response of Specimen20 with an aspect ratio of 6. While both specimens show a progressive reduction in stress for the same strain target, the strength degradation due to the formation and propagation of fatigue cracks occurs at an earlier stage and at a faster rate for the bar with the larger aspect ratio. This leads to a reduced fatigue life for the bar with the largest aspect ratio, as summarized in Table 3.8. Furthermore, a clear shift in the skeleton curve can be observed after the reversal cycle from the yield plateau in compression, as described by Dodd and Restrepo (1995).

Table 3.8. Summary of constant amplitude tests.

Strain History	$\varepsilon_{\max}$	$\varepsilon_{\min}$	$\varepsilon_a = \frac{\Delta\varepsilon}{2}$	Specimen	Aspect Ratio, s/d_b	MFR	$2N_f$	W_{fT} *(in-kip/in²)*
1	0.030	-0.005	0.0175	Spec14	8	A	13	19.4
2	0.024	-0.004	0.014	Spec15	8	A	29	36.0
				Spec16	8	A	23	24.0
				Spec20	6	A	41	56.6
				Spec22	6	A	37	47.6
3	0.030	-0.01	0.02	Spec18	8	A	9	16.2
				Spec31	8	B	17	23.2
				Spec23	6	A	17	33.1
4	0.000	-0.045	0.0225	Spec25	8	A	5	10.9
				Spec32	8	B	7	12.7
				Spec21	6	A	7	18.0

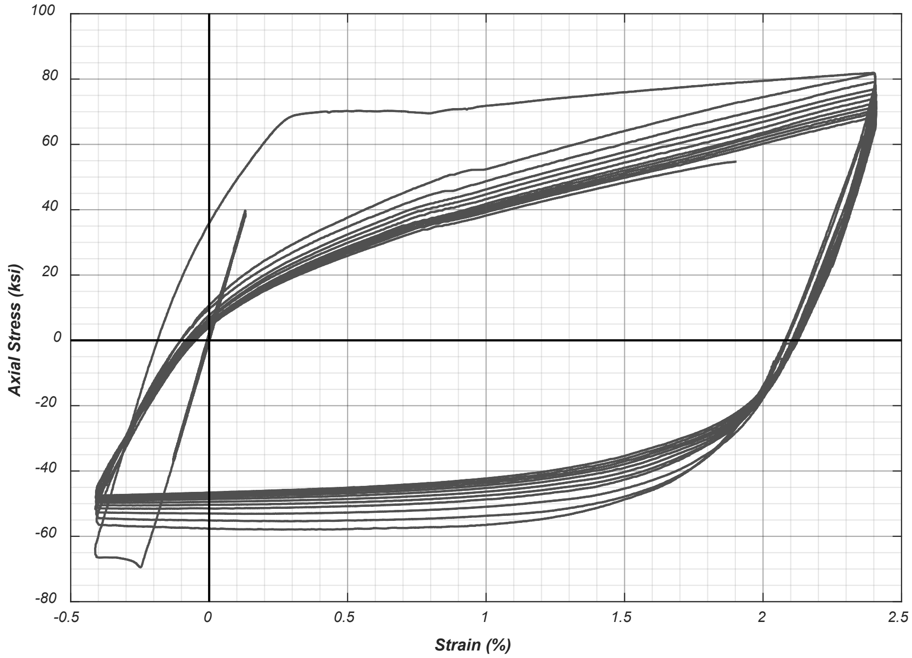

Figure 3.42. Axial stress-strain response of No. 18 bar with unsupported length of 8d_b subjected to constant amplitude cycles of +2.4%, -0.4% (Specimen16).

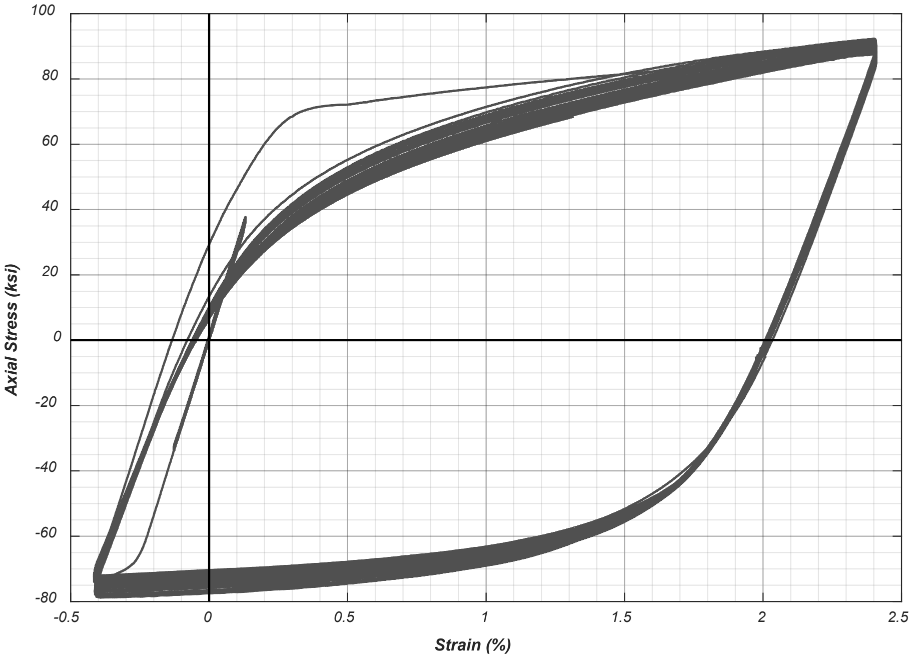

Figure 3.43. Axial stress-strain response of No. 18 bar with unsupported length of 6d_b subjected to constant amplitude cycles of +2.4%, -0.4% (Specimen20).

Strain penetration was visible in all test and must be accounted for when interpreting the results of the experimental work. For instance, as the unsupported length of the bar increases due to strain penetration, the stress at buckling continues to decrease with each successive cycle. While strain penetration is to be expected in a RC column, if buckling occurs at the base of the column, strain penetration will occur only at the base of the bar. In the current experimental work, the effects of strain penetration are exacerbated as the tested bars experience strain penetration at both the top and bottom of the bars. Moreover, while the steel blocks placed around the bars at the surface of the sulfur concrete simulate the restraint provided by the transverse reinforcement in a column and the cone formed at the base of RC columns after cyclic loading, they further intensify the effects of strain penetration. The combined strain penetration (top plus bottom) at the end of testing equaled to 1.6 in. for Specimen19 (8.88% of original unsupported length), 0.9 in. for Specimen20 (6.67% of original unsupported length), and 1.25 in. for Specimen24 (9.26% of original unsupported length).

To ensure that the fatigue life of the bars was not influenced by the surface grinding and placement of strain gages near the critical region of the buckled bars, Specimen22 was tested with the same loading history, and with the same aspect ratio, as Specimen20 but without strain gages at mid-height. Specimen22 failed at 37 half-cycles compared to 41 for Specimen20, leading the authors to believe that the placement of the strain gages has a negligible effect on the fatigue life of the bars. The same behavior is observed when comparing bars with different aspect ratios from the same manufacturer (MFR-A in Table 3.8) and tested with the same strain history, as shown in Figure 3.44 thru Figure 3.47.

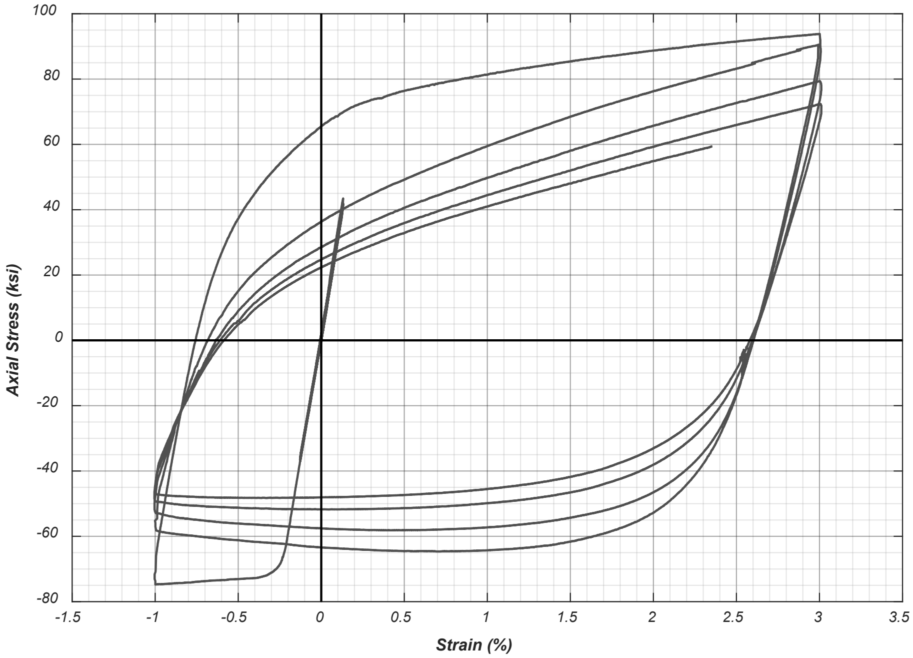

Figure 3.44. Axial stress-strain response of No. 18 bar with unsupported length of 8d_b subjected to constant amplitude cycles of +3.0%, -1.0% (Specimen18).

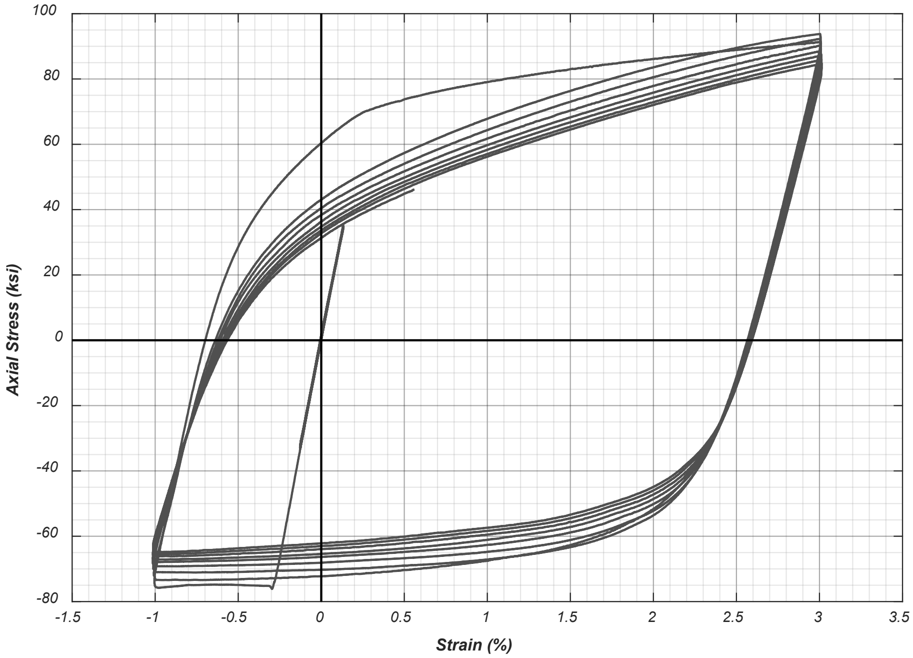

Figure 3.45. Axial stress-strain response of No. 18 bar with unsupported length of 6d_b subjected to constant amplitude cycles of +3.0%, -1.0% (Specimen23).

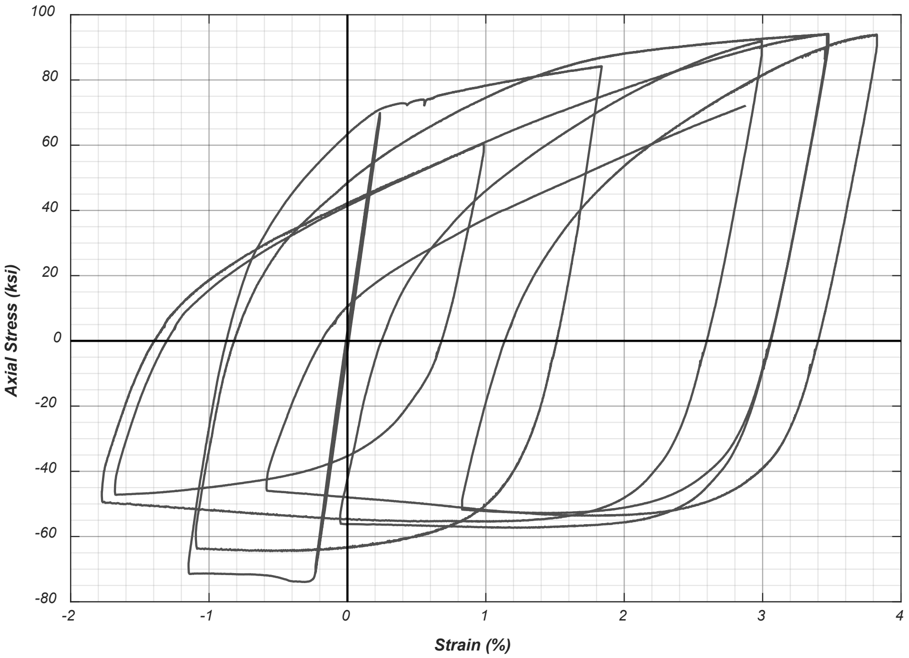

Figure 3.46. Axial stress-strain response of No. 18 bar with unsupported length of 8d_b subjected to random history cycles (Specimen19).

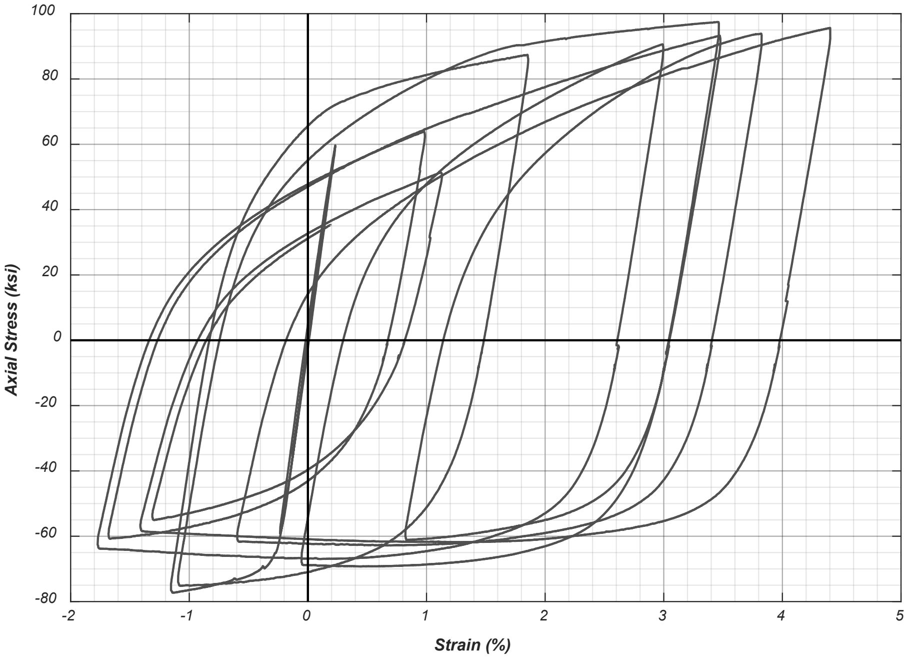

Figure 3.47. Axial stress-strain response of No. 18 bar with unsupported length of 6d_b subjected to random history cycles (Specimen24).

3.8. Typical Modes of Failure

Except for the specimens tested under monotonic tension that exhibited necking prior to failure, the specimens tested under Buckling-Straightening conditions developed one or more cracks on the concave side of the bar. All observed cracks began at the root of the transverse bar deformations and propagated toward the convex side of the bar. This phenomenon is in line with all previous research outlined in Section 2.3.3. These cracks resulted in failure once there was not enough material to transfer the applied loads. No necking was observed prior to failure of these specimens. The following observations were made for the fracture surfaces of the specimens shown in Figure 3.48 and Figure 3.49:

- Specimen 15: Longitudinal ribs in North-East/South-West direction with bar buckling orthogonal to longitudinal ribs. The fatigue crack originated and propagated diagonally along the base of the transverse bar deformation at the location of maximum bending on the concave face of the bar. This stable crack propagation is characterized by a more uniform surface. Once crack became unstable, it started propagating horizontally towards the convex face of the bar in a fan-type pattern. Multiple independent cracks formed at transverse deformations adjacent to failure surface.
- Specimen 16: Longitudinal ribs in North-East/South-West direction with bar buckling orthogonal to longitudinal ribs. Fatigue crack originated and propagated along the base of the transverse bar deformation at the location of maximum bending on the concave face of the bar. Once crack became unstable, it started propagating horizontally towards the convex face of the bar in a fan-type pattern.

- Specimen18: Longitudinal ribs in North/South direction with bar buckling parallel to longitudinal ribs. Crack formed at the intersection of the longitudinal and transverse deformations and propagated mainly horizontally towards the convex face of the bar in a fan-type pattern.
- Specimen19: Longitudinal ribs in North/South direction with bar buckling parallel to longitudinal ribs. Crack formed at the intersection of the longitudinal and transverse deformations and propagated diagonally for a shorter length, compared to Specimens 15 and 16, and continued propagating horizontally towards the convex face of the bar in a fan-type pattern.
- Specimen20: Longitudinal ribs in East/West direction with bar buckling orthogonal to longitudinal ribs. Fatigue crack originated along the base of the transverse bar deformation at the location of maximum bending on the concave face of the bar. However, it mainly propagated horizontally towards the convex face of the bar in a fan-type pattern.
- Specimen23: Longitudinal ribs in East/West direction with bar buckling orthogonal to longitudinal ribs. Fatigue crack originated and propagated along the base of the transverse bar deformation at the location of maximum bending on the concave face of the bar. Once crack became unstable, it started propagating horizontally towards the convex face of the bar in a fan-type pattern. A fatigue crack was observed on the convex face of the bar.
- Specimen24: Longitudinal ribs in East/West direction with bar buckling orthogonal to longitudinal ribs. Crack originated along the base of the transverse bar

deformation at the location of maximum bending on the concave face of the bar. Crack mainly propagated horizontally towards the convex face of the bar in a fan-type pattern.

- Specimen31: Longitudinal ribs in North-East/South-West direction with bar buckling orthogonal to longitudinal ribs. Fatigue crack originated and propagated diagonally along the base of the transverse bar deformation at the location of maximum bending on the concave face of the bar. Once crack became unstable, it started propagating horizontally towards the convex face of the bar in a fan-type pattern. Multiple independent cracks formed at transverse deformations adjacent to failure surface.

(a) (b)

(c) (d)

Figure 3.48. Fracture surfaces due to Plastic Buckling-Straightening Fatigue: (a) Specimen15; (b) Specimen16; (c) Specimen18; (d) Specimen19.

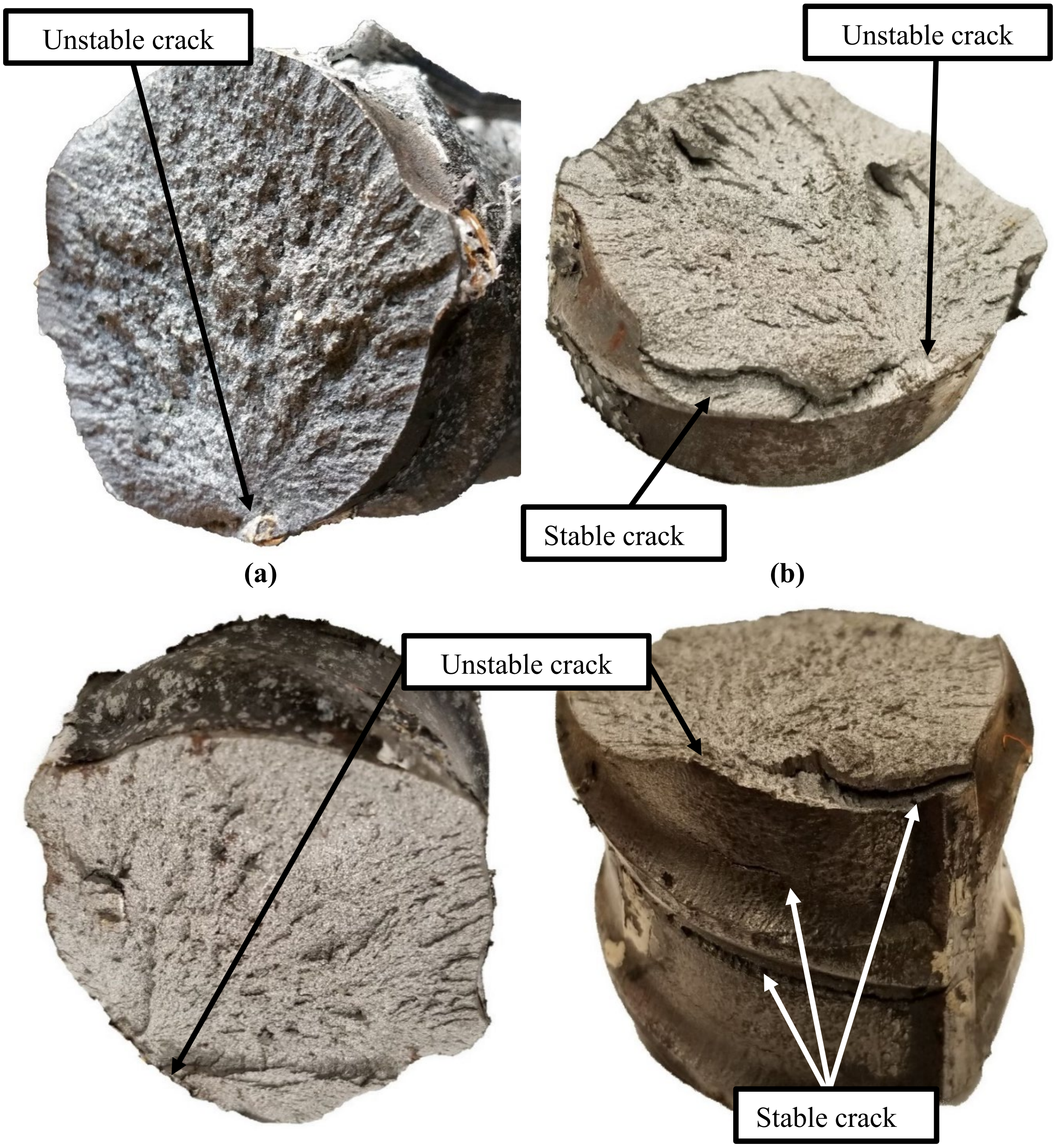

(a) (b)

(c) (d)

Figure 3.49. Fracture surfaces due to Plastic Buckling-Straightening Fatigue: (a) Specimen20; (b) Specimen23; (c) Specimen24; (d) Specimen31.

3.9. Comparison to Existing Low-Cycle Fatigue Models

The trends between aspect ratio, strain amplitude, and fatigue life can be clearly observed when results are plotted on a log-log scale, resulting in the liner relationships shown in Figure 3.50. As shown by Koh and Stephens (1991) and Mander et al. (1994), given the large strain amplitudes, and resulting large plastic strains used in the "low-cycle" fatigue testing of the bars, mean stress effects can be ignored. Moreover, given the difficulty in using plastic-strain amplitude to plot the log-log results for the number of half-cycles to failure due to Bauschinger effects and given that the prediction of fatigue life is not expected to improve (for constant amplitude testing the yield strain is essentially a constant value) the Koh-Stephens fatigue model with total strain amplitude is used to fit the data of the fatigue life of the bars. From Figure 3.50 the following expressions are derived:

$$\varepsilon_a = 0.04(2N_f)^{-0.29} \rightarrow 8d_b \text{ (MFR A)} \qquad R^2 = 0.98$$

Equation 3-2

$$\varepsilon_a = 0.03(2N_f)^{-0.13} \rightarrow 8d_b \text{ (MFR B)} \qquad R^2 = 1.0$$

Equation 3-3

$$\varepsilon_a = 0.04(2N_f)^{-0.27} \rightarrow 6d_b \text{ (MFR A)} \qquad R^2 = 0.92$$

Equation 3-4

While the correlation of the fatigue life expression is very good for both unsupported lengths of $6d_b$ and $8d_b$ for MFR-A, the R^2 value of 1.0 for $8d_b$ (MFR-B) is due having only two data points for that manufacturer, hence the perfect fit. Similarly, given that only one data point is available for $1.5d_b$ (MFR-A), no fatigue life expression can be produced.

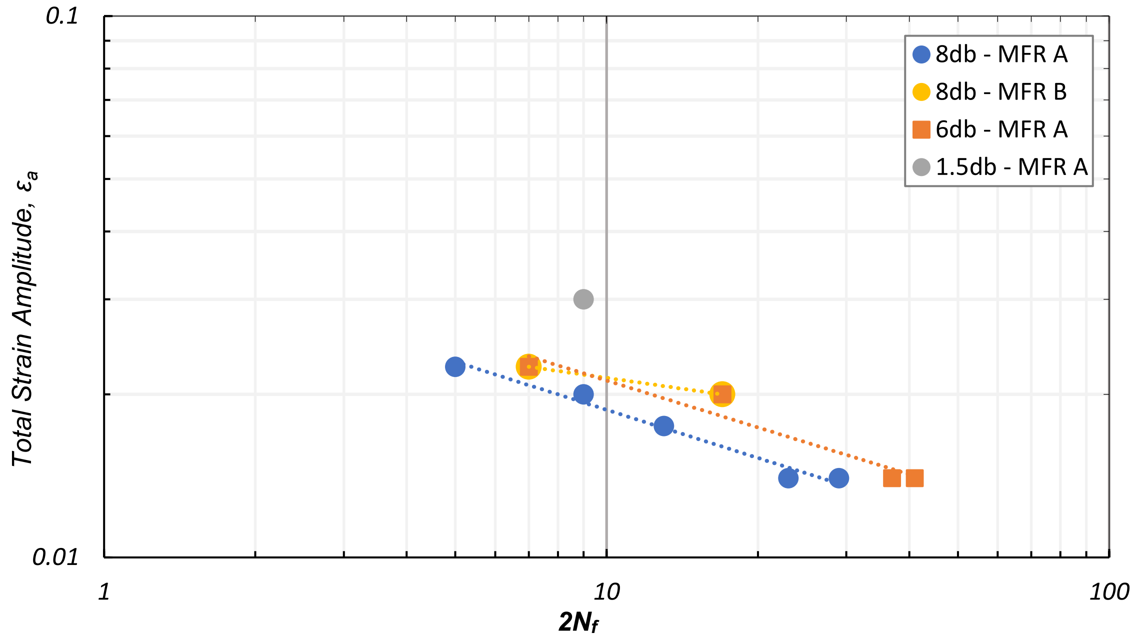

Figure 3.50. Experimental data fit using Koh-Stephens fatigue life model for No. 18 bars with unsupported lengths of 8*d_b*, 6*d_b*, and 1.5*d_b*.

While the effects of inelastic buckling are not directly accounted for in such fatigue model, Figure 3.50 shows the effects the aspect ratio has on the fatigue life of the bar. The greater the aspect ratio, the shorter the expected fatigue life of the bar and vice-versa. The influence of the total strain amplitude, ε_a, is also evident, with a larger strain amplitude resulting in a reduced fatigue life. These results match the trends observed on previous research (Mander et al., 1994; Brown and Kunnath, 2004) as shown in Figure 3.51. Furthermore, as also observed by Brown and Kunnath (2004), bars with larger diameter exhibit longer fatigue life at lower strain amplitudes, while for larger amplitudes, the opposite holds.

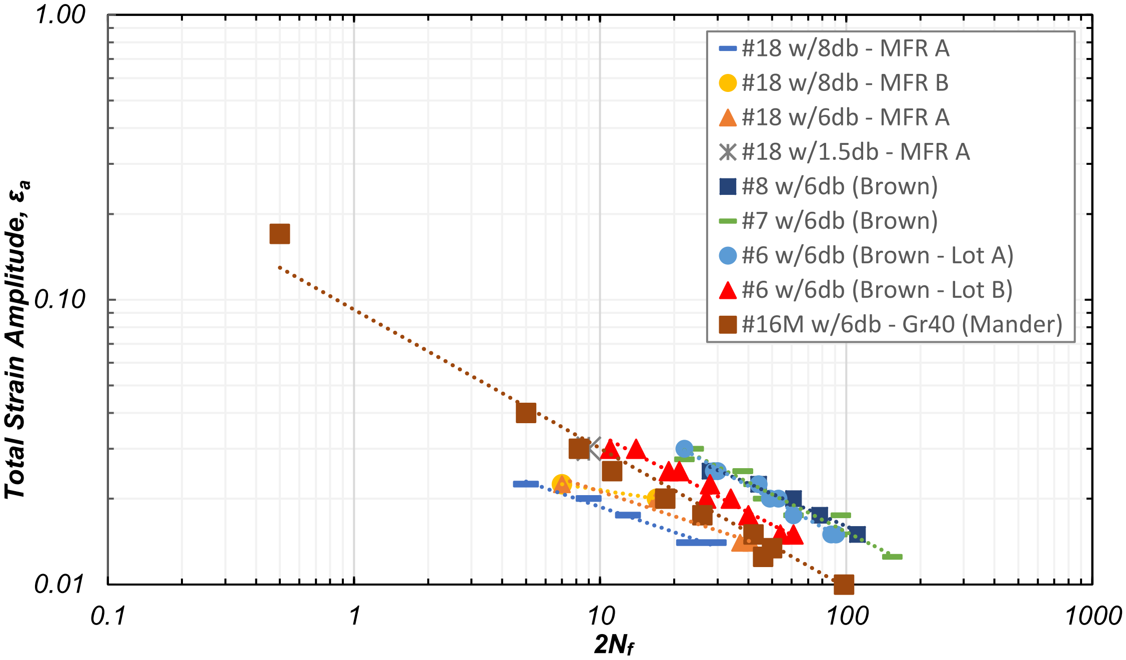

Figure 3.51. Comparison of experimental results with data from Mander et al. (1994) and Brown and Kunnath (2004) using Koh-Stephens fatigue life model.

By comparing the number of half-cycles to failure, a difference in the fatigue life of bars tested with the same aspect ratio and under the same total strain amplitude, but from different manufacturers or different grades of steel, could be observed. Depending on the manufacturing process used, the material properties of the reinforcing steel, such as the yield strength, tensile strength, and toughness, vary (Slavin and Ghannoum, 2015) thus affecting the fatigue life of the bars. By comparing the bars from MFR-A and MFR-B, it is evident that bars from MFR-B, which have a lower yield but a larger tensile-to-yield strength ratio, have a larger toughness and thus a larger fatigue life than the bars from MRF A, suggesting that the manufacturing process might be an important factor when determining the plastic buckling-straightening fatigue life of large-diameter reinforcing steel. Given that these results are only from one batch of bars from each manufacturer, further testing is suggested to confirm this trend.

To calculate the total energy dissipated until failure, W_{fT}, the total area encompassing the hysteresis loops for each specimen was numerically integrated via the trapezoidal method with a unit spacing. The total energy dissipated is equal to the modulus of toughness of the bars and is shown in Table 3.8. Figure 3.52 plots the normalized total energy, were the elastic energy, W_y, corresponds to the average elastic energy for each MFR, from the monotonic tensile tests, see Section 3.5.2. The previously identified trends related to the fatigue life of the bars, the aspect ratio, and the total strain amplitude can also be deducted from Figure 3.52. The modulus of toughness for MFR-B bars is higher than that of MFR-A bars, and so is the fatigue life under the same strain history, see Table 3.8. The results are plotted in Figure 3.53 for the energy-based fatigue life model proposed by Tong et al. (1989), relating the total energy dissipated to the number of half-cycles.

Figure 3.54 fits the experimental results based on the Mander et al. (1994) energy-based fatigue life expression as follows:

$$\varepsilon_a = 0.07(W_{fT})^{-0.46} \rightarrow 8d_b \text{ (MFR A)} \qquad R^2 = 0.91$$

Equation 3-5

$$\varepsilon_a = 0.04(W_{fT})^{-0.20} \rightarrow 8d_b \text{ (MFR B)} \qquad R^2 = 1.0$$

Equation 3-6

$$\varepsilon_a = 0.08(W_{fT})^{-0.43} \rightarrow 6d_b \text{ (MFR A)} \qquad R^2 = 0.88$$

Equation 3-7

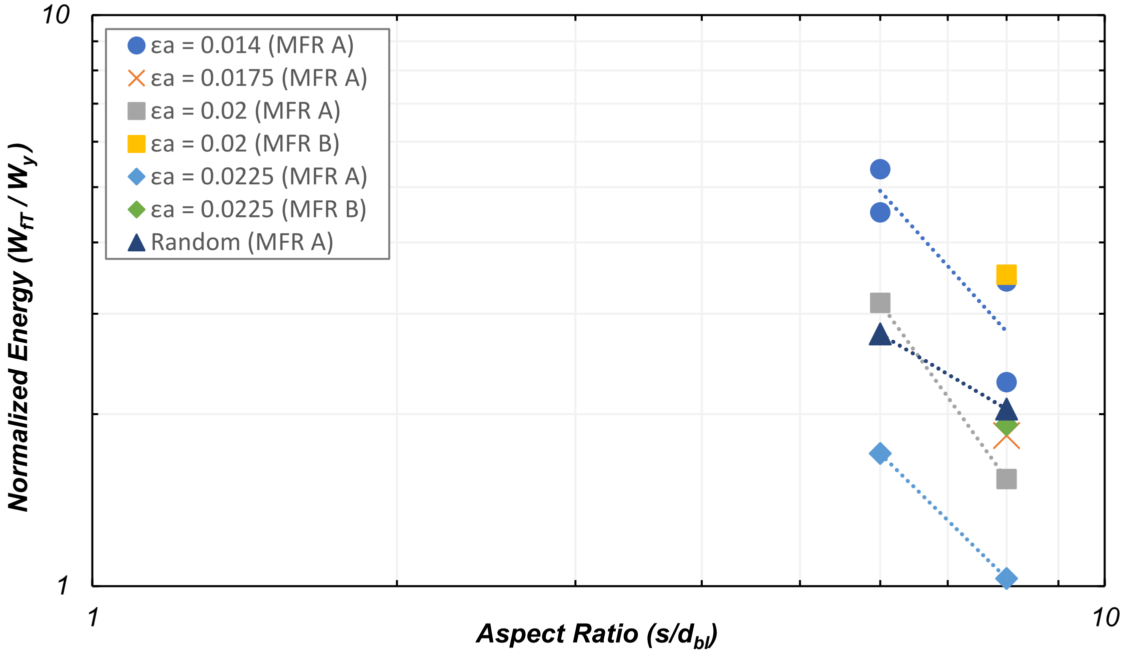

Figure 3.52. Normalized total dissipated energy to failure.

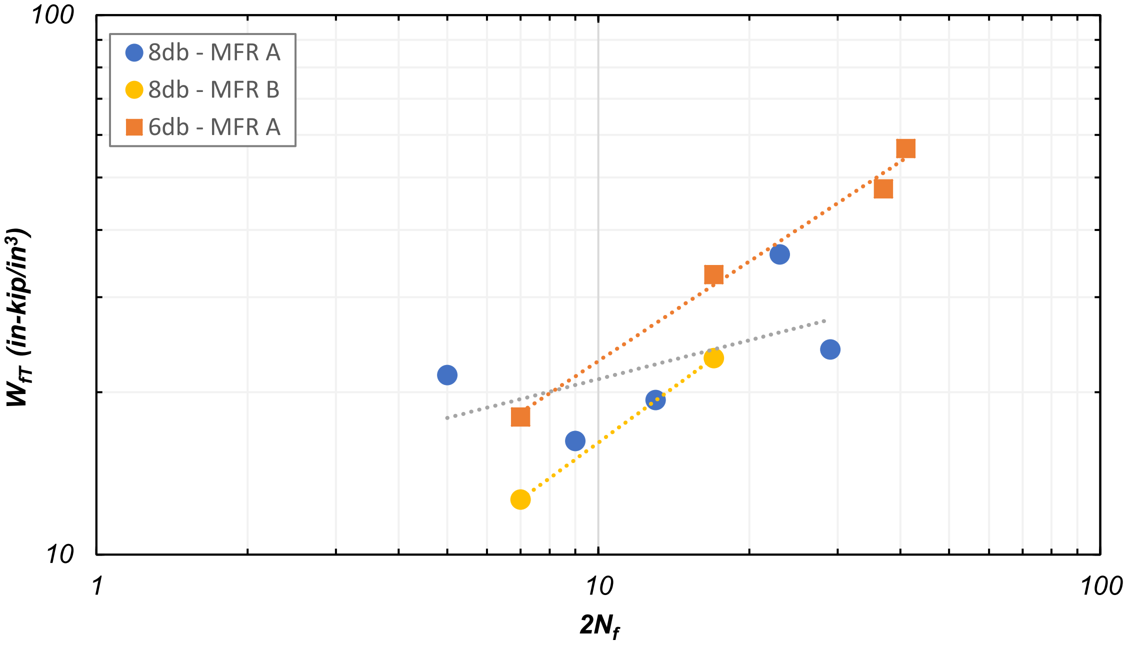

Figure 3.53. Experimental data fit using energy-based Tong et al.(1989) fatigue life model for total energy for No. 18 bars with unsupported lengths of 8d_b and 6d_b.

By comparing the R^2 values obtained from the energy-based fatigue life expressions in Equation 3-5 and Equation 3-7 with those obtained from the fatigue-life model (Equation 3-2 and Equation 3-4) based on the number of half-cycles to failure, $2N_f$, the energy-based model is less accurate. Similar results were reported by Brown and Kunnath (2004). Results from Mander et al., 1994 and Brown and Kunnath, 2004 are plotted along the experimental results for the No. 18 bars in Figure 3.55.The very significant trends observed in Figure 3.51 and Figure 3.55 conclusively indicate that Coffin-Mason models are specific to a bar type (i.e. chemical composition, manufacturing process, bar deformation geometry and radii) and aspect ratio. It is likely temperature below the transition temperature plays an important role too. For these reasons, a unique and simple formulation cannot be established.

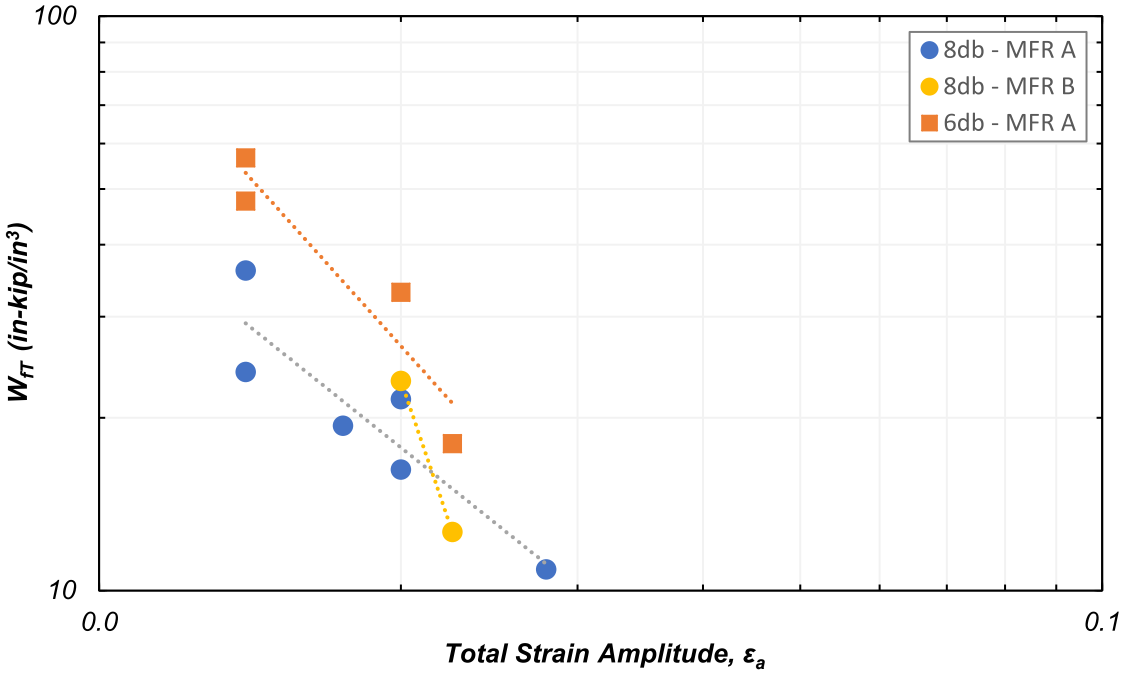

Figure 3.54. Experimental data fit using energy-based Mander et al. (1994) fatigue life model for total strain for No. 18 bars with unsupported lengths of 8d_b and 6d_b.

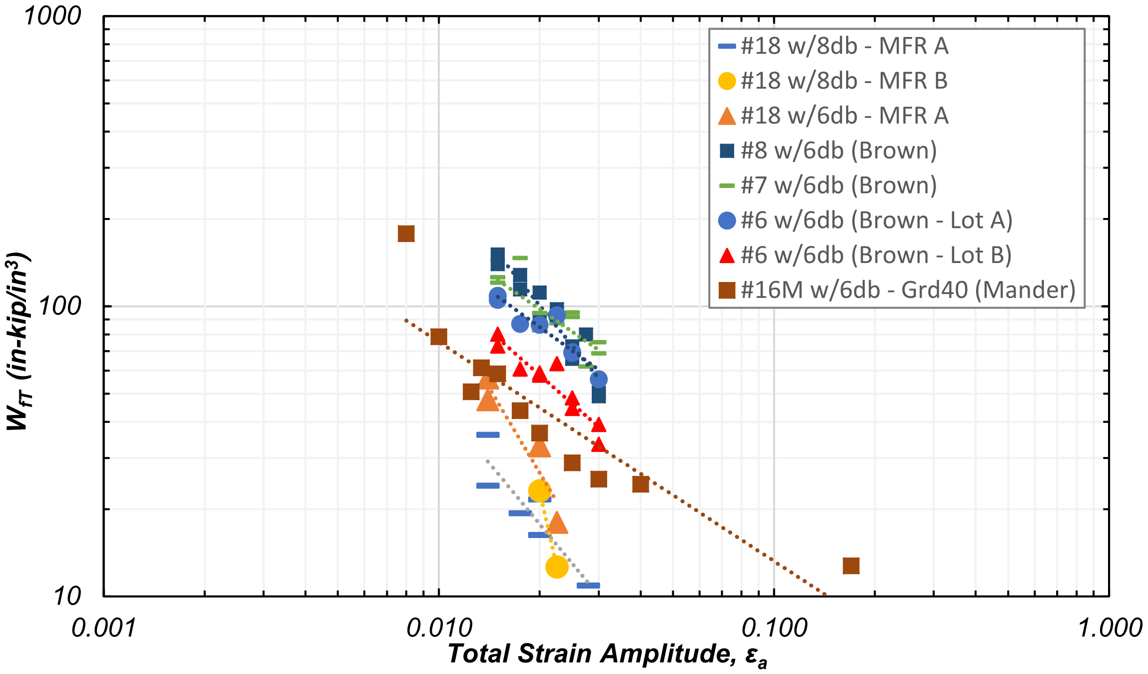

Figure 3.55. Comparison of experimental results with data from Mander et al. (1994) and Brown and Kunnath (2004) using energy-based fatigue life model for total strain.

3.10. Summary

Through the innovative use of sulfur concrete as part of a loading apparatus, the cyclical testing of large diameter reinforcing steel bars under large strain amplitudes was successfully achieved after multiple unsuccessful attempts by others. These tests allowed to obtain the missing characterization of the plastic buckling-straightening fatigue life of large diameter bars. Results from relevant experimental work were used to derive a random strain history to test the bars in the bar buckling test apparatus. A series of constant amplitude tests were also performed to establish a relationship between deformation amplitude and the number of cycles to failure, for comparison with current fatigue models. Smear strains for all tests were measured using in-house designed clip gages with a fixed gage length equal to half the bar’s unsupported lengths. The smeared strains calculated from these displacement sensors more closely approximate the strains assumed in design. Unsupported lengths equivalent to $1.5d_b$, $6d_b$, and $8d_b$ were used for the experimental work. Results from these tests show strength degradation of the bars due to the formation and propagation of fatigue cracks, which occur at an earlier stage and at a faster rate for bars with larger aspect ratios. As a result, bars with larger unsupported lengths tend to have a reduced plastic buckling-straightening fatigue life. The influence of the total strain amplitude, ε_a, on the fatigue life of the bars was also evident. A larger strain amplitude resulted in a reduced fatigue life of the bars. These results match the trends observed by previous research. Finally, from comparing the results of the fatigue life of bars from different manufacturers, the manufacturing process might be an important factor when determining the plastic buckling-straightening fatigue life of large-diameter reinforcing steel bars. This characteristic along with the chemical composition, bar deformation geometry and radii, and aspect ratio of different bars make a unique and simple formulation for the plastic buckling-straightening fatigue life of steel reinforcing steel unattainable.

Chapter 3, in part, is a reprint of the material as it appears in *SSRP Report 17/10: Plastic buckling-straightening fatigue of large diameter reinforcing steel bars*, 2018. Duck, D. E.; Carreño, R.; and Restrepo, J. I. The dissertation author was the primary investigator and author of this report.

Chapters 3, in part, is currently being prepared for submission for publication of the material. Duck, D. E. & Restrepo, J. I. The dissertation author was the primary investigator and author of this material.

Chapters 3, in part, is currently being prepared for submission for publication of the material. Duck, D. E., Restrepo, J. I, & Carreño, R. The dissertation author was the primary investigator and author of this material.

CHAPTER 4.

DAMAGE INDEX FOR BARS SUBJECTED TO PLASTIC BUCKLING-STRAIGHTENING CYCLES

4.1. General

Results of the experiments carried out in this project showed significant differences in the plastic buckling-straightening fatigue life of #18 bars from two different manufacturers. Additionally, the test program confirmed the observations made by Brown and Kunnath (2004) and Slavin and Ghannoum (2015) that half-cycle versus strain amplitude relationships and other “low-cycle fatigue” formulations vary significantly between reinforcing bars because of dependence on multiple variables the design engineer cannot control. From the point of view of seismic design these empirical “low-cycle” fatigue relationships, even if these were uniquely defined or vary narrowly, are troublesome. On one hand, the method of converting earthquake induced axial strain cycles into equivalent half-cycles has several difficulties that will most likely introduce an unquantifiable bias. On the other hand, it is difficult to understand the meaning of number of half-cycles to failure, as after a few cycles crack propagation in a buckled/straightened reinforcing bar results in a reduction of the axial tensile load capacity. This raises the following question, what is the meaning in seismic design to know that a buckle/straightened bar can sustain ten further cycles at a given strain amplitude before it finally fractures, if after ten half-cycles, the bar has lost forty percent of the capacity? That is, the number of half-cycles to fracture at a given strain amplitude and at a given temperature is, in the opinion of the authors, a meaningless metric for use in seismic design. This is aggravated by the fact that crack propagation in many metals is sensitive to temperature (Petch, 1958).

Chapter 4 describes a different methodology to quantify the fatigue life of a reinforcing steel bar. The proposed mechanics-based approach stems from the observations made by Dodd and Restrepo (1995) during the testing of small-aspect ratio reinforcing steel coupons that the axial strain at the tensile point minus the minimum plastic compressive axial strain imposed to the bar is a constant, where the strains above are natural strains, see Section 2.3.1. In this chapter, the Dodd-Restrepo method is extended below to bars deforming in axial and bending (i.e. undergoing plastic buckling and straightening cycles). The method can also be used as a cumulative strain damage approach within a cyclic pushover analysis, and also within a nonlinear time-history analysis, but such implementation is outside the scope of this experimental work.

4.2. Damage Index

The observation made by Dodd Restrepo (1995) that the strain at the peak tensile load computed as a natural strain is a constant, indicates that the tensile strain where localization in a bar occurs will decrease if the bar is ever subjected to a plastic compressive strain, see Figure 2.32. In a bar subjected to axial strains, such localization will be manifested as necking. An extension of this observation is made here:

Localization in a bar subjected to reversed cyclic loading, involving plastic buckling and straightening, occurs when the plastic strain amplitude (i.e. tensile minus compressive, in natural strains) in the extreme fiber in the concave side of the bar equals the uniform natural strain. Depending on a few variables, including the chemical composition of the steel, temperature and bar deformation geometry, further plastic strain demands will result in the propagation of necking or cracking, and ultimately, in bar fracture.

The observation made by Dodd Restrepo is not an attempt to predict the bar deformation at fracture, but to predict the strain where necking occurs. Similarly, the extension of the concept presented here will not predict the deformation or number of cycles at fracture, but intends to predict the onset of localization. This observation can be expressed in terms of a damage index (DI) calculated for the extreme fiber in the concave side of the plastic hinge in a buckled bar, see Figure 4.1. The DI is defined in Equation 4-1 as follows:

$$DI=\frac{\varepsilon'_{peak,tens}-\varepsilon'_{peak,comp}}{\varepsilon'_{su}}$$ **Equation 4-1**

where $\varepsilon'_{peak,tens}$, $\varepsilon'_{peak,comp}$ are the buckled bar plastic-hinge concave side extreme fiber maximum natural tensile and minimum compressive strains, respectively. ε'_{su} is the uniform natural strain at tensile load obtained from a monotonic test.

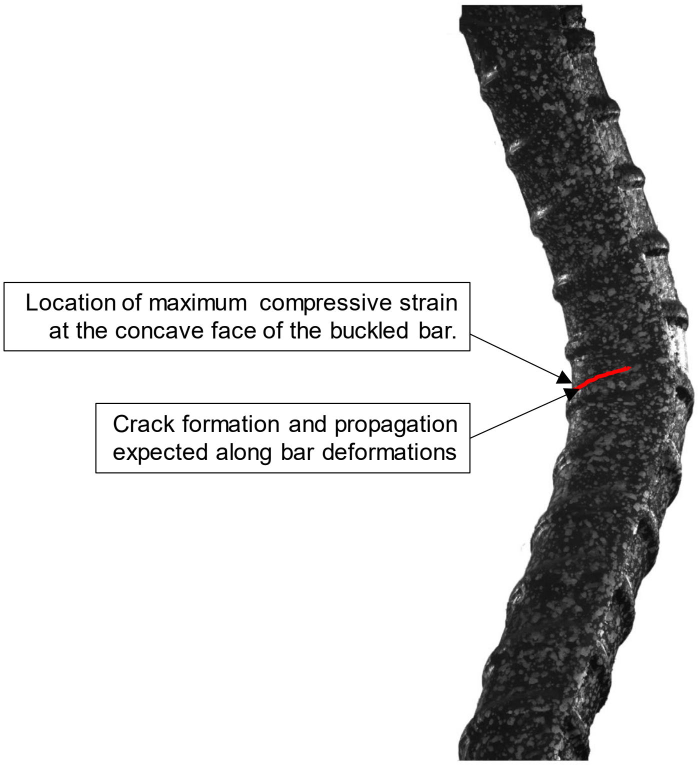

Figure 4.1. Shape of buckled bar with expected location of crack formation taken using DIC camera setup.

4.3. Damage Index Results

The maximum tensile and minimum compressive engineering strains corresponding to the concave and convex faces in the plastic hinge of a buckled bar as well as the curvature at the mid-section of the tested specimens were computed from a least-squares solution based on strain gauge records collected during each test.

Under the assumption that plane sections remain plane, finding the axial strain and curvature of a deformed section is equivalent to computing the parameters of the plane containing the deformed section. Assuming all points in the original configuration are in a horizontal plane (Z = 0) and deformations occurring only in the Z direction, the equation of the deformed plane becomes:

$$c_0 + c_1 \cdot x + c_2 \cdot y = \varepsilon_z$$

Equation 4-2

where c_0, c_1, and c_2 are the parameters of the plane and ε_z the strain in the Z direction of the point with original coordinates (x, y, 0).

If the coordinates of only three points are known, the parameters of the plane equation are solved from a simple linear system with equal number of equations and unknowns. If the coordinates of more than three points in the plane are known, however, no unique plane will contain all the points (considering the noise from the strain gauge records), and therefore an optimal plane must be found. This optimal plane is defined as the one with the least sum of square errors between the measured and predicted value of the z coordinate, see Equation 4-3.

$$\min \sum_{i=1}^{n} \left(\varepsilon_{z,i} - c_0 - c_1 \cdot x_i - c_2 \cdot y_i \right)^2$$

Equation 4-3

where $\varepsilon_{z,i}$ is the measured strain at point i, with initial coordinates $(x_i, y_i, 0)$.

Solving the optimization problem, the following system of equations is obtained:

$$\begin{bmatrix} 1 & \overline{x} & \overline{y} \\ \overline{x} & \frac{1}{n}\sum_{i=1}^{n} x_i^2 & \frac{1}{n}\sum_{i=1}^{n} x_i \cdot y_i \\ \overline{y} & \frac{1}{n}\sum_{i=1}^{n} x_i \cdot y_i & \frac{1}{n}\sum_{i=1}^{n} y_i^2 \end{bmatrix} \times \begin{bmatrix} c_0 \\ c_1 \\ c_2 \end{bmatrix} = \begin{bmatrix} \overline{\varepsilon} \\ \frac{1}{n}\sum_{i=1}^{n} \varepsilon_i \cdot x_i \\ \frac{1}{n}\sum_{i=1}^{n} \varepsilon_i \cdot y_i \end{bmatrix}$$

Equation 4-4

Once the parameters of the plane equation are found, the axial strain, defined for our purposes as the strain at the origin, is computed as $\varepsilon_{ave} = c_0$.

The curvature values are calculated from the rotation between the normal unit vectors of the initial and deformed planes, corresponding to $\hat{n}_0 = (0,0,1)^T$ and $\hat{n} = (-c_1, -c_2, 1)^T \Big/ \sqrt{1 + c_1^2 + c_2^2}$ respectively. Given the small magnitude of the plane rotations, the amplitude of curvature (ϕ) can be easily computed from the dot product of $\hat{n}_0$ and $\hat{n}$, Equation 4-5.

$$\phi = \cos^{-1}\left(\hat{n}_0 \cdot \hat{n}\right)$$

Equation 4-5

The directional component of the curvature is represented by the angle between the axis of rotation (computed from the cross product of $\hat{n}_0$ and $\hat{n}$) and the x axis in the horizontal plane (θ), see Equation 4-6.

$$\theta = \hat{n}_0 \times \hat{n}$$

$$\theta = \tan^{-1}\left(\frac{\theta_x}{\theta_y}\right)$$

Equation 4-6

In all the cyclic tests performed for this study, between three and five strain gauges were installed around the perimeter of the section of interest.

Figure 4.2 plots (a) the natural strain history applied to Specimen 16 using the clip gages, which smeared the strain over the theoretical points of inflection spaced at 8d_b; (b) the local natural strain history on the extreme fiber on the concave side at the bar mid-height where the plastic hinge developed upon buckling; (c) the local natural strain history on the extreme fiber on the convex side at the bar mid-height where the plastic hinge developed upon buckling; and (d) the damage index DI computed for this specimen. In the latter plot, green dots are used for DI <= 1, small crosses are used when DI > 1 and the maximum tensile load measured in these loading cycles ranges between (1, 0.95) of the maximum tensile load recorded in the test, and large crosses are used when the DI > 1 and the maximum tensile load measured in these loading cycles is smaller than 0.95 of the maximum tensile load recorded in the test.

In Specimen 16, the loading history consisted of three cycles of strain reversals within the elastic limit, followed by a series of reverse strain cycles ranging from +2.37% and -0.4% (natural strains) as measured with the clip gage. Whereas the peak strains and strain range measured by the clip gage remains constant in the second phase of the test, the local strains in the bar plastic hinge exhibit a clear ratcheting phenomenon. Ratcheting of the strains is believed to be partly caused by bond slip of the bar in the sulfur concrete, similar to the bar slip a reinforcing bar would experience in a plastic hinge developing at a column end. At the peak of every cycle where the bar yields or hardens in tension, bar bond slip (i.e. strain penetration) results in a small increase of the bar's free length and causes the bar to buckle at a smaller compressive stress in a subsequent cycle. The main difference between the bar bond slip in a column and in the specimens tested in this loading apparatus is that bond slip occurs at both ends of the bar, whereas in a column occurs at only one end, except for bars in jacketed columns and bars in flared columns. It is noted that because of the hydraulic gripping systems, the bond slip in bars tested in universal testing machines is negligible and ratcheting may not be as pronounced.

Figure 4.3 depicts the axial load history recorded for Specimen 16. Two horizontal lines indicating the 90 and 95% of the maximum tensile force recorded in the test are also plotted in this figure. In this test, a gradual decrease in the axial tensile force occurs in the bar when subjected to the same smear tensile strain of 2.4% after the DI exceeds one. Such degradation is likely to be caused by crack propagation in the critical region in the plastic hinge that developed at the bar mid-height. We speculate that the decrease could be more pronounced had the bar been tested at a temperature lower than the transition temperature, and the number of cycles to fracture would have also decreased.

The same procedure to obtain the damage index was performed using the random strain history described in Section 3.6.1. The partial response of Specimen19 is shown in Figure 4.4, up to the point at which data from the strain gages is available to calculate the natural strain at the concave and convex faces of the buckled bar. Given that the loading history is random, see Figure 4.5, cyclic softening or ratcheting cannot be assessed and all damage index markers are shown as green circles in Figure 4.5d. The bar was able to resist three more cycles of random loading after the last available damage index corresponding to 1.04 before fracture occurred.

The loading history applied to Specimen25, see Figure 4.6, of strain cycles between 0.0% and -4.6% (smeared natural strains measured with the clip gage over $8d_b$), though not realistic for a bar in a reinforced concrete element, shows the applicability of the proposed DI in extreme strain conditions. In the first strain excursion to a smear natural strain of -4.6%, the natural strain in the extreme fiber in the concave side of the bar reached -18.4%. Since Specimen 25 had not been subjected to a plastic tensile strain yet, a DI = (0.129%-

18.4%) / 11.7% = 1.58 was reached in this excursion alone. That is, under the proposed DI, Specimen25 was expected to fracture while being straightened after it buckled the first time. Specimen25 did not fracture as indicated by the DI and reached a tensile force of 313 kip. This specimen was able to resist one more complete cycle. The tensile force of 295 kip measured in the second plastic cycle was 94.4% of the force measured in the first cycle, that is, this specimen exhibited strength degradation, which is likely due to crack propagation. This specimen fractured half-way into the third cycle. Once more, we speculate that had we performed this test on bar at temperature lower than the transition temperature, the bar could have fractured upon straightening for the first time.

Appendix E replicate Figure 4.2 and Figure 4.3 for Specimens 14 through 25.

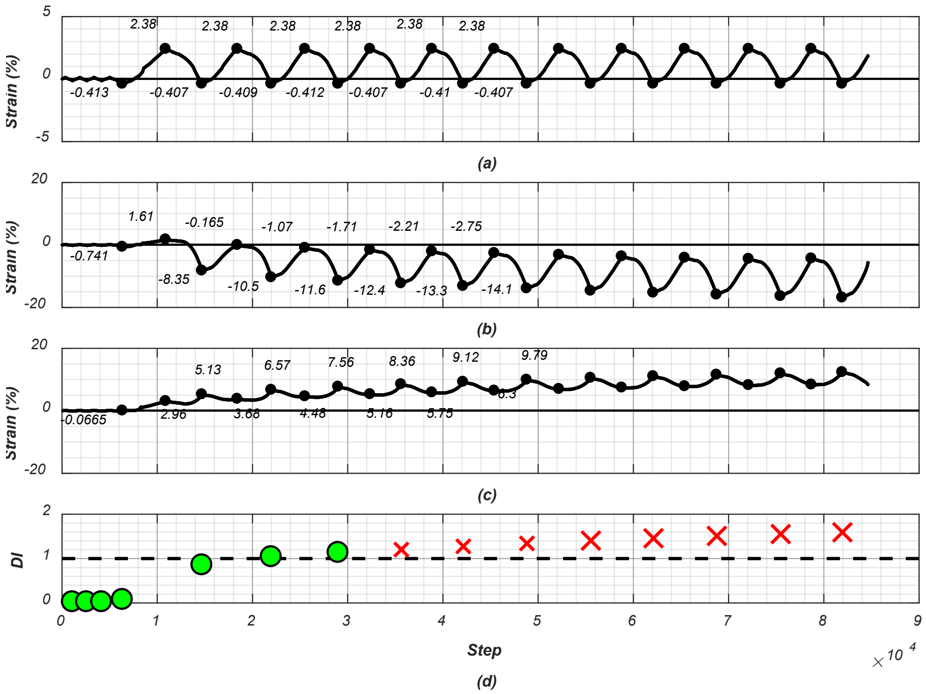

Figure 4.2. Specimen16: (a) Average natural strain between theoretical POI; (b) Natural strain history on concave side of bar at mid-height; (c) Natural strain history on concave side of bar at mid-height; (d) Damage index.

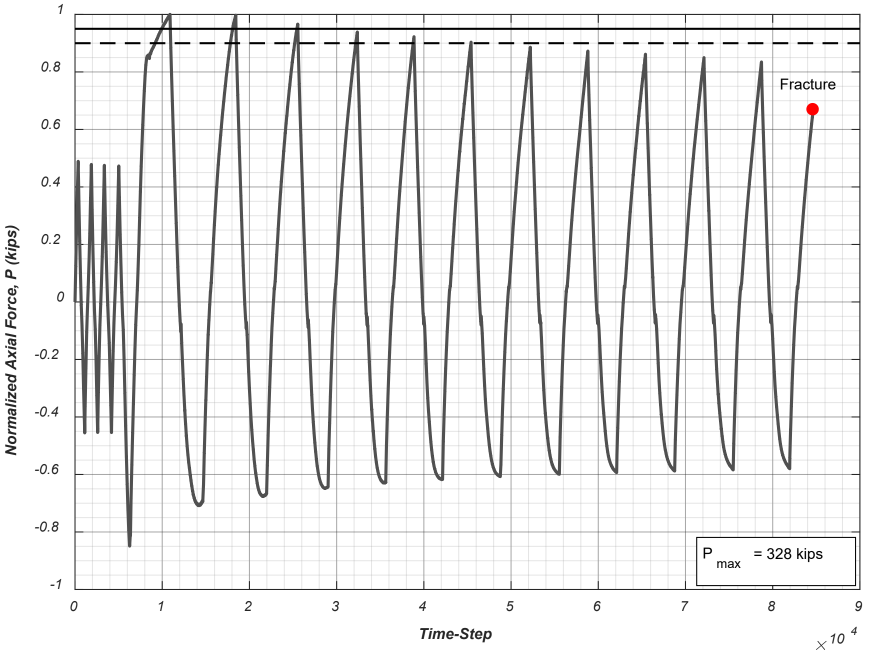

Figure 4.3. Axial load history with horizontal lines indicating 90% and 95% of the maximum tensile force (Specimen16).

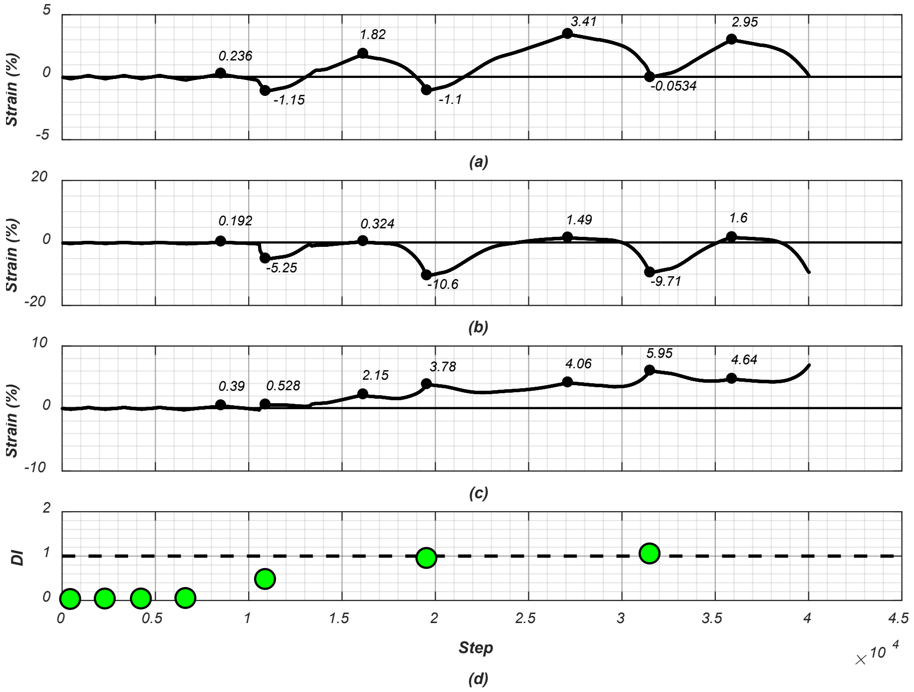

Figure 4.4. Specimen 19: (a) Average natural strain between theoretical POI; (b) Natural strain history on concave side of bar at mid-height; (c) Natural strain history on concave side of bar at mid-height; (d) Damage index.

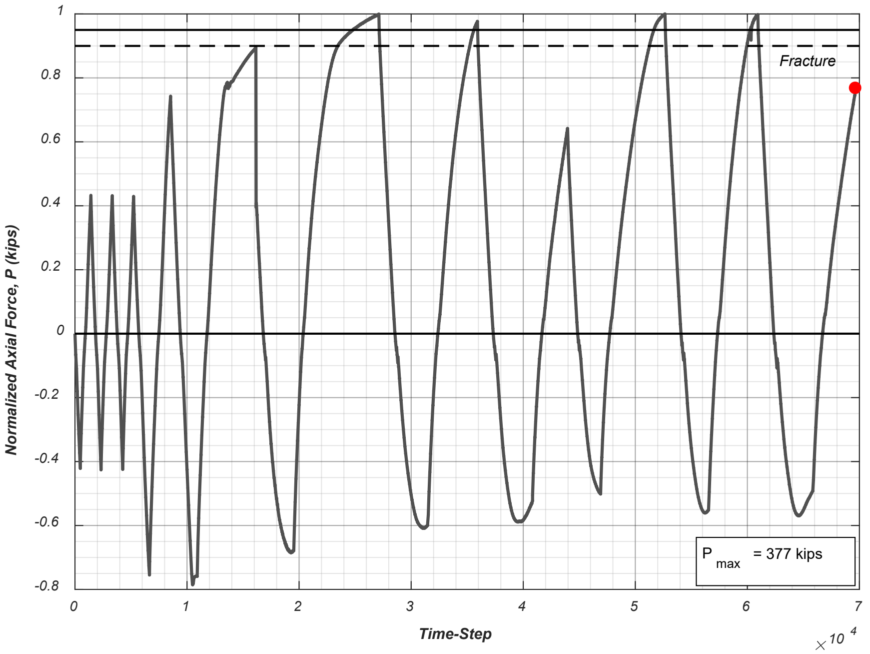

Figure 4.5. Axial load history with horizontal lines indicating 90% and 95% of the maximum tensile force (Specimen19).

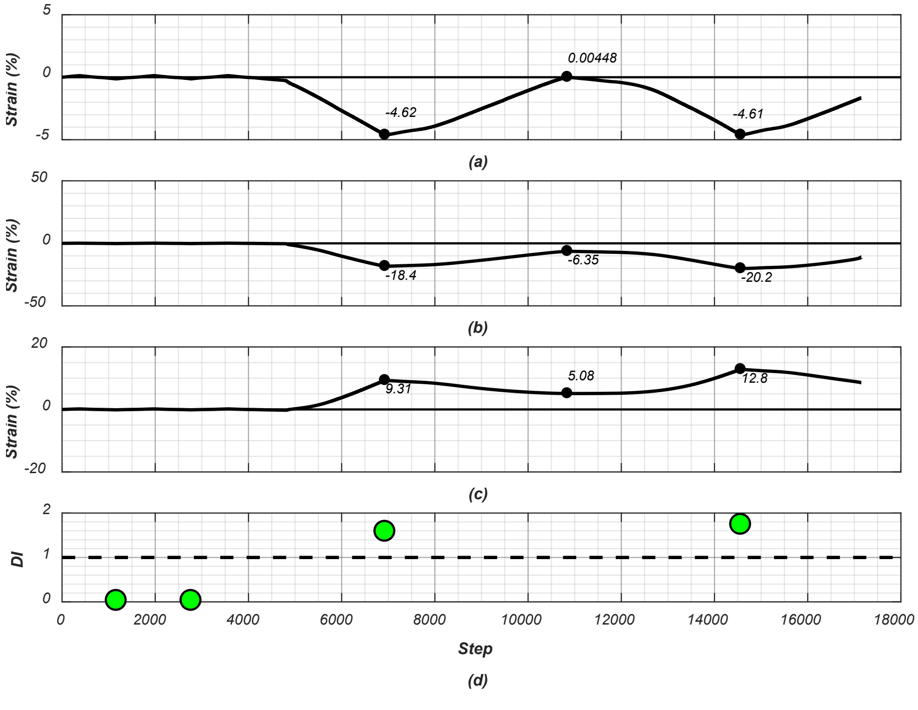

Figure 4.6. Specimen25: (a) Average natural strain between theoretical POI; (b) Natural strain history on concave side of bar at mid-height; (c) Natural strain history on concave side of bar at mid-height; (d) Damage index.

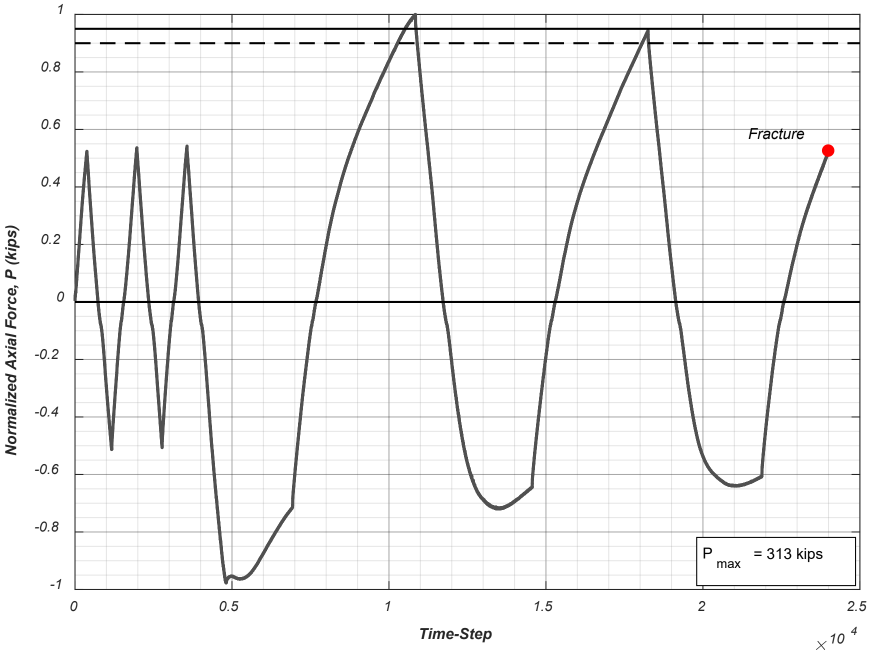

Figure 4.7. Axial load history with horizontal lines indicating 90% and 95% of the maximum tensile force (Specimen25).

4.4. Damage Index Base on DIC Results

Using the DIC setup discussed in Section 3.3, high-resolution images were taken of all test bars and post-processed using a commercially available software. While mechanical instrumentation, such as the in-house designed clip gage and strain gages, provide excellent data, it is susceptible to damage during testing. This was the case with the strain gages placed at mid-height of the test bars, which got damaged after large deformations on the concave face of the buckled bar. One of the advantages of using DIC technology is that it is not susceptible to damage during testing. Nonetheless, it is still susceptible to "damage" in the form of obstructions during testing that may cover regions of the bar. This, however, can be overcome by taking footage from different angles, as was done in this experimental work. Figure 4.8 and Figure 4.9 plot the Damage Index and load history for specimen 26, which was not instrumented, based on the data provided by DIC. While the compressive smeared strain obtained from the DIC analysis was 21.3% prior to fracture of the test bar, a compressive strain upwards of 59% was captured by DIC processing on the concave side of the test bar, see Figure 4.8b. Furthermore, as shown in Figure 4.10, this technology provides data that would be almost impossible to attain using mechanical instrumentation, such as the strain profiles at various stages of testing. The deformed bar stages shown in Figure 4.10 correspond to points A-F shown in Figure 4.9. These strain profiles clearly show stress concentrations at the base of the bar deformations as previously reported. Figure 4.11 shows the peculiar fracture of test bar after PBSF testing. This fracture surface was unique to this specimen and is believed to be due to the extreme loading at the last cycle which caused a rapid crack propagation.

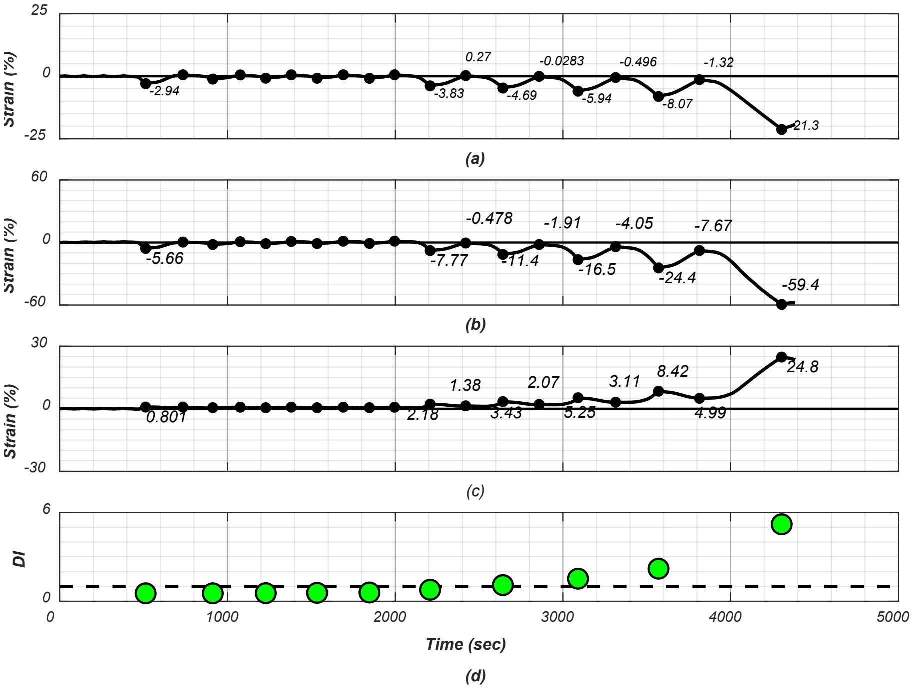

Figure 4.8. Specimen26: (a) Average natural strain between theoretical POI; (b) Natural strain history on concave side of bar at mid-height; (c) Natural strain history on concave side of bar at mid-height; (d) Damage index.

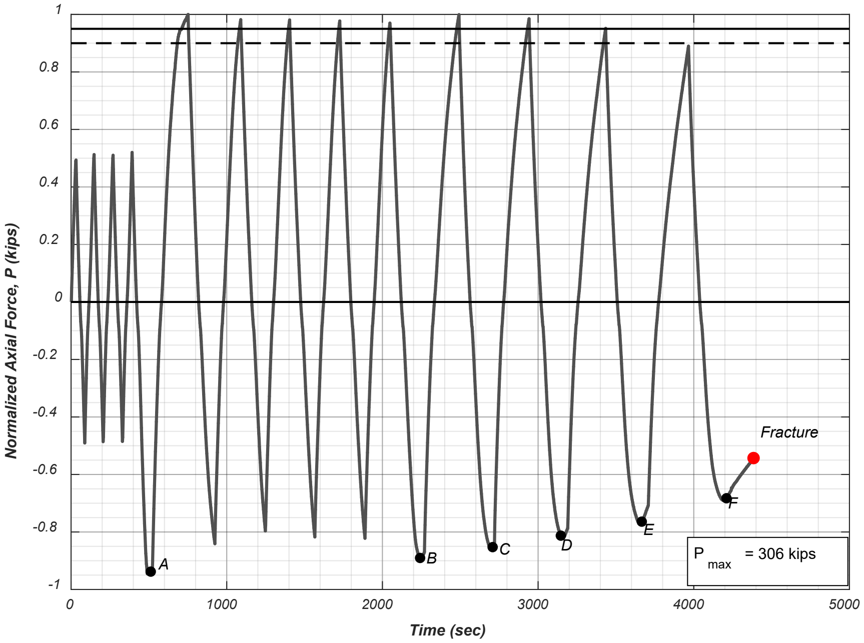

Figure 4.9. Axial load history with horizontal lines indicating 90% and 95% of the maximum tensile force (Specimen26).

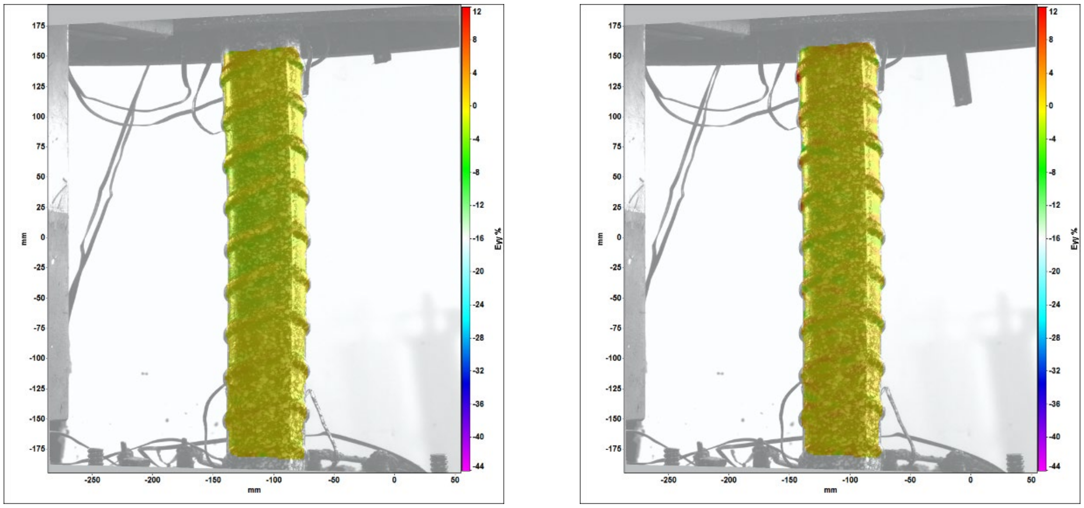

(a) Point A **(b) Point B**

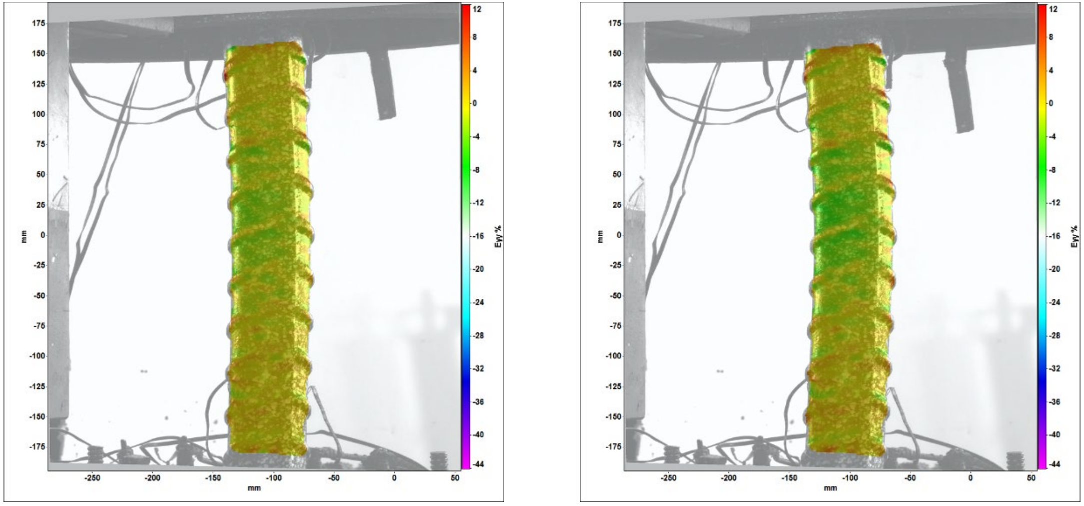

(c) Point C **(d) Point D**

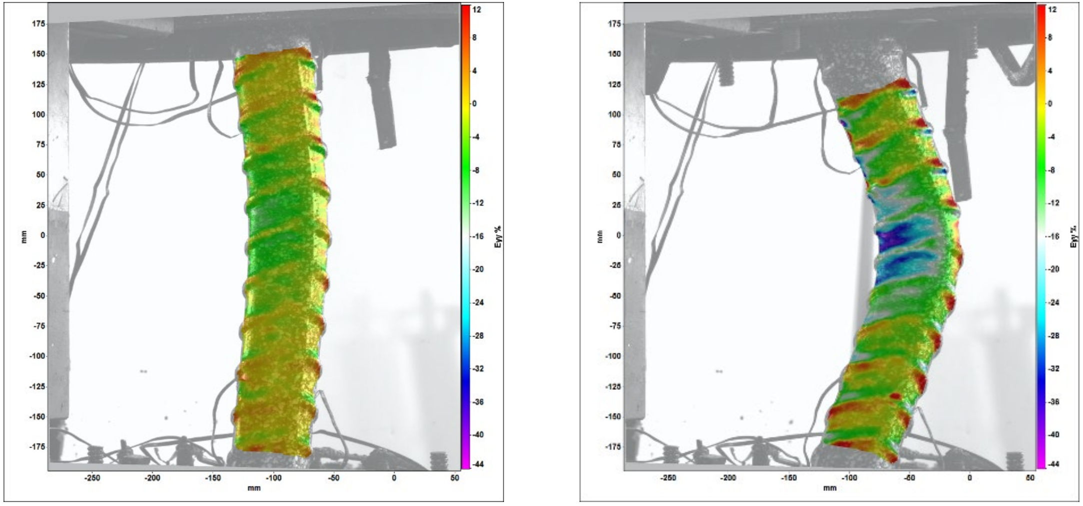

(e) Point E **(f) Point F**

Figure 4.10. Strain profiles at various stages of loading per Figure 4.9.

(a)

(b)

Figure 4.11. Specimen26: (a) Fractured bar after PBSF testing; (b) Fracture surface.

4.5. Summary

This chapter described a strain-based Damage Index that is used to calculate the onset of localization (either onset of necking or of crack propagation) in a steel bar subjected to plastic buckling / straightening cycles. The proposed Damage Index stems from the observation made by Dodd and Restrepo (1995) that in straight steel bars, the strain at the onset of necking decreases with applied compressive plastic strain. Damage Indices were computed for Specimens 9 to 25, which excellent results. This chapter highlights the results of three of these tests. It is important to note that the Damage Index does not intend to predict the deformation or number of cycles at which a reinforcing bar will fail, but the strain at which localization is likely to occur. The use of DIC technology was highlighted as a way of obtaining data not easily attained through mechanical instrumentation.

Chapter 4, in part, is a reprint of the material as it appears in *SSRP Report 17/10: Plastic buckling-straightening fatigue of large diameter reinforcing steel bars*, 2018. Duck, D. E.; Carreño, R.; and Restrepo, J. I. The dissertation author was the primary investigator and author of this report.

Chapters 4, in part, is currently being prepared for submission for publication of the material. Duck, D. E. & Restrepo, J. I. The dissertation author was the primary investigator and author of this material.

Chapters 4, in part, is currently being prepared for submission for publication of the material. Duck, D. E., Restrepo, J. I, & Carreño, R. The dissertation author was the primary investigator and author of this material.

REFERENCES

AASHTO. 2014. *American Association of State Highway and Transportation Officials (AASHTO), LRFD Bridge Design Specifications*. https://www.worldcat.org/title/aashto-lrfd-bridge-design-specifications-si-units/oclc/30836884?referer=di&ht=edition.

ACI Committee 215, Fatigue of Concrete. 1992. *Considerations for Design of Concrete Structures Subjected to Fatigue Loading (ACI 215R-74, 1997, Revised 1992). American Concrete Institute*.

ACI Committee 548. 1993. "ACI 548.2R Guide for Mixing and Placing Sulfur Concrete in Construction." Reapproved 1998.

Apostolopoulos, Ch Alk. 2007. "Mechanical Behavior of Corroded Reinforcing Steel Bars S500s Tempcore under Low Cycle Fatigue." *Construction and Building Materials* 21 (7): 1447–1456.

ASTM C386. 2012. *C386−93: Standard Practice for Use of Chemical-Resistant Sulfur Mortar*. https://doi.org/10.1520/C0386-93R12.

ASTM E8. 2016. *E8/E8M-16a: Standard Test Methods for Tension Testing of Metallic Materials*. https://doi.org/10.1520/E0008_E0008M-16A.

Bae, Sungjin, Alexa M. Mieses, and Oguzhan Bayrak. 2005. "Inelastic Buckling of Reinforcing Bars." *Journal of Structural Engineering* 131 (2): 314–321. https://doi.org/10.1061/(ASCE)0733-9445(2005)131:2(314).

Basquin, OH. 1910. "The Exponential Law of Endurance Tests." In *Proc. ASTM*, 10:625.

Bayrak, Oguzhan, and Shamim A Sheikh. 2001. "Plastic Hinge Analysis." *Journal of Structural Engineering* 127 (9): 1092–1100.

Berry, Michael P. 2003. "Estimating Flexural Damage in Reinforced Concrete Columns. Master Thesis." Master Thesis, Dept. of Civil and Environmental Engineering, University of Washington.

Berry, Michael P, and Marc O Eberhard. 2005. "Practical Performance Model for Bar Buckling." *Journal of Structural Engineering* 131 (7): 1060–1070.

Bresler, B, and PH Gilbert. 1961. "Tie Requirements for Reinforced Concrete Columns." In *Journal Proceedings*, 58:555–570.

Bretz Jr., Thomas E. 1979. "Properties of Sulfur Concrete." PhD Thesis.

Brown, J., and S. K. Kunnath. 2004. "Low-Cycle Fatigue Failure of Reinforcing Steel Bars." *ACI Materials Journal* 101 (6): 457–466.

Burton, Kenneth T. 1965. "Fatigue Tests of Reinforcing Bars." *PCA Research and Development Laboratories* 7 (3): 13–23.

Caltrans. 2013. *Caltrans Method of Tests for Steel Reinforcing Bar Butt Splices: California Test 670 (CT_670)*. Department of Transportation.

Caltrans, SDC. 2019. "Caltrans Seismic Design Criteria Version 2.0." *California Department of Transportation, Sacramento*.

Chen, W. F., and E. M. Lui. 1987. "Structural Stability: Theory and Implementation." *Elsevier New York*.

Coffin, L F., Jr. 1954. "A Study of the Effects of Cyclic Thermal Stresses on a Ductile Metal." *American Society of Mechanical Engineers* Vol. 76: 931–50.

Considere, A. 1891. "Résistance Des Pièces Comprimées." *Annexe Au Compte Rendu Du Congrès International Des Procédés de Construction. Paris*.

Cosenza, Edoardo, and Andrea Prota. 2006. "Experimental Behaviour and Numerical Modelling of Smooth Steel Bars under Compression." *Journal of Earthquake Engineering* 10 (03): 313–329.

Czarnecki, B, and JE Gillott. 1989. "Effect of Different Admixtures on the Strength of Sulphur Concrete." *Cement, Concrete and Aggregates* 11 (2): 109. https://doi.org/10.1520/CCA10111J.

Czarnecki, B, and JE Gillott. 1990. "The Effect of Mix Design on the Properties of Sulfur Concrete." *Cement, Concrete and Aggregates* 12 (2): 79.

Dhakal, Rajesh Prasad, and Koichi Maekawa. 2002. "Modeling for Postyield Buckling of Reinforcement." *Journal of Structural Engineering* 128 (9): 1139–1147.

Dodd, LL, and JI Restrepo-Posada. 1995. "Model for Predicting Cyclic Behavior of Reinforcing Steel." *Journal of Structural Engineering* 121 (3): 433–445.

Duck, David E, Rodrigo Carreno, and José I Restrepo. 2018. "Plastic Buckling-Straightening Fatigue of Large Diameter Reinforcing Steel Bars." January. La Jolla: University of California, San Diego.

El-Bahy, Ashraf, Sashi K Kunnath, William C Stone, and Andrew W Taylor. 1999. "Cumulative Seismic Damage of Circular Bridge Columns: Benchmark and Low-Cycle Fatigue Tests." *ACI Structural Journal* 96: 633–641.

Engesser, Friedrich. 1889. *Die Knickfestigkeit Gerader Stäbe*. W. Ernst & Sohn.

Fei, Jun, and David Darwin. 1999. "Fatigue of High Relative Rib Area Reinforcing Bars." University of Kansas Center for Research, Inc.

Feng, Yuhao, Mervyn J Kowalsky, and James M Nau. 2014. "Finite-Element Method to Predict Reinforcing Bar Buckling in RC Structures." *Journal of Structural Engineering* 141 (5): 04014147.

Fragiadakis, Michalis, Rui Pinho, and Stelios Antoniou. 2008. "Modelling Inelastic Buckling of Reinforcing Bars under Earthquake Loading." *Computational Structural Dynamics and Earthquake Engineering: Structures and Infrastructures Book Series* 2: 347.

Gebman, M.J, S.A. Ashford, and J.I. Restrepo. 2006. "Axial Force Transfer Mechanisms within Cast-In-Steel Shell Piles." Techreport Report SSRP 06/16. Department of Structural Engineering, University of California at San Diego.

Gomes, Augusto, and Júlio Appleton. 1997. "Nonlinear Cyclic Stress-Strain Relationship of Reinforcing Bars Including Buckling." *Engineering Structures* 19 (10): 822–826.

Gracia, Violeta, Enric Vazquez, and Sergio Carmona. 2004. "Utilization of By-Produced Sulfur for the Manufacture of Unmodified Sulfur Concrete." *International RILEM Conference on the Use of Recycled Materials in Building and Structures*, no. 1: 1051–1063.

GREGOR, R., and A. HACKL. 1978. "A New Approach to Sulfur Concrete." In , 54–78. https://doi.org/10.1021/ba-1978-0165.ch004.

Hanson, J. M., K. T. Burton, and E. Hognestad. 1968. "Fatigue Tests of Reinforcing Bars Effect of Deformation Pattern." *PCA Research and Development Laboratories* 10 (3): 2–13.

Hanson, John M, MF Somes, and T Helagson. 1974. "Investigation of Design Factors Affecting Fatigue Strength of Reinforcing Bars-Test Program." *Special Publication* 41: 71–106.

Hawileh, RA, JA Abdalla, F Oudah, and K Abdelrahman. 2010. "Low-Cycle Fatigue Life Behaviour of BS 460B and BS B500B Steel Reinforcing Bars." *Fatigue & Fracture of Engineering Materials & Structures* 33 (7): 397–407.

Helgason, Thorsteinn, JM Hanson, NF Somes, WG Corley, and Eivind Hognestad. 1976. "Fatigue Strength of High-Yield Reinforcing Bars." *Nchrp Report*, no. 164.

J.Brown, and S.K.Kunnath. 2000. "Low-Cycle Fatigue Behavior of Longitudinal Reinforcement in Reinforced Concrete Bridge Columns," 126.

Jhamb, IC, and JG Mac Gregor. 1974. “Effect of Surface Characteristics on Fatigue Strength of Reinforcing Steel.” *Special Publication* 41: 139–168.

Jhamb, IC, and JG MacGregor. 1974. “Stress Concentrations Caused by Reinforcing Bar Deformations.” *Special Publication* 41: 169–182.

Kármán, Theodor von. 1910. “Untersuchungen Über Knickfestigkeit.” In *Mitteilungen Über Forschungsarbeiten Auf Dem Gebiete Des Ingenieurwesens Insbesondere Aus Den Laboratorien Der Technischen Hochschulen*, 1–44. Springer Berlin Heidelberg. https://doi.org/10.1007/978-3-662-01994-8_1.

Kashani, Mohammad M. 2017. “Size Effect on Inelastic Buckling Behavior of Accelerated Pitted Corroded Bars in Porous Media.” *Journal of Materials in Civil Engineering* 29 (7): 04017022. https://doi.org/10.1061/(ASCE)MT.1943-5533.0001853.

Kashani, Mohammad M, Peyman Alagheband, Rafid Khan, and Sean Davis. 2015. “Impact of Corrosion on Low-Cycle Fatigue Degradation of Reinforcing Bars with the Effect of Inelastic Buckling.” *International Journal of Fatigue* 77: 174–185.

Kashani, Mohammad M, Aneeka K Barmi, and Viktoria S Malinova. 2015. “Influence of Inelastic Buckling on Low-Cycle Fatigue Degradation of Reinforcing Bars.” *Construction and Building Materials* 94: 644–655.

Kashani, Mohammad M., Shunyao Cai, Sean A. Davis, and Paul J. Vardanega. 2019. “Influence of Bar Diameter on Low-Cycle Fatigue Degradation of Reinforcing Bars.” *Journal of Materials in Civil Engineering* 31 (4): 06019002. https://doi.org/10.1061/(ASCE)MT.1943-5533.0002637.

Kashani, Mohammad M., Adam J. Crewe, and Nicholas A. Alexander. 2013. “Nonlinear Cyclic Response of Corrosion-Damaged Reinforcing Bars with the Effect of Buckling.” *Construction and Building Materials* 41 (April): 388–400. https://doi.org/10.1016/j.conbuildmat.2012.12.011.

Koh, SK, and RI Stephens. 1991. “Mean Stress Effects on Low Cycle Fatigue for a High Strength Steel.” *Fatigue & Fracture of Engineering Materials & Structures* 14 (4): 413–428.

Kokubu, Masatane, and Hajime Okamura. 1969. “Fatigue Behavior of High Strength Deformed Bars in Reinforced Concrete Bridges.”

Kunnath, Sashi, Amit Kanvinde, Guowei Zhang, and Yan Xiao. 2009. “Effects of Buckling and Low Cycle Fatigue on Seismic Performance of Reinforcing Bars and Mechanical Couplers for Critical Structural Members.” Davis: University of California, Davis.

MacGregor, James G, IC Jhamb, and N Nuttall. 1971. “Fatigue Strength of Hot Rolled Deformed Reinforcing Bars.” In *Journal Proceedings*, 68:169–179.

Madsen, I. 1941. *Report of Crane Girder Tests*.

Mander, JB, FD Panthaki, and A Kasalanati. 1994. "Low-Cycle Fatigue Behavior of Reinforcing Steel." *Journal of Materials in Civil Engineering* 6 (4): 453–468.

Mander, John Barrie. 1983. "Seismic Design of Bridge Piers." PhD Thesis.

Manson, S. S. 1953. "Behavior of Materials under Conditions of Thermal Stress." In *Heat Transfer Symposium, University of Michigan Engineering Research Institute, Ann Arbor, Mich*, 9–75.

Massone, Leonardo M., and Daniel Moroder. 2009. "Buckling Modeling of Reinforcing Bars with Imperfections." *Engineering Structures* 31 (3): 758–767. https://doi.org/10.1016/j.engstruct.2008.11.019.

Mattock, Alan H. 1967. "Rotation Capacity of Reinforced Concrete Beams." *Journal of Structual Division ASCE* 93: 519–522.

Mau, ST, and Mounir El-Mabsout. 1989. "Inelastic Buckling of Reinforcing Bars." *Journal of Engineering Mechanics* 115 (1): 1–17.

McBee, W. C., T. A. Sullivan, and H. L. Fike. 1985. "Sulfur Construction Materials." United States Department of the Interior - Bureau of Mines.

Menegotto, M, and P Pinto. 1973. "Method of Analysis for Cyclically Loaded Reinforced Concrete Plane Frames Including Changes in Geometry and Non-Elastic Behavior of Elements Under Combined Normal Force and Bending." *Proceedings. IABSE Symposium on Resistance and Ultimate Deformability of Structures Acted on by Well-Defined Repeated Loads*.

Meyers, Marc A, and Krishan Kumar Chawla. 2009. *Mechanical Behavior of Materials*. Vol. 2. Cambridge University Press Cambridge.

Miner, MA. 1945. "Cumulative Fatigue Damage." *Journal of Applied Mechanics* 12 (3): A159–A164.

Monti, Giorgio, and Camillo Nuti. 1992. "Nonlinear Cyclic Behavior of Reinforcing Bars Including Buckling." *Journal of Structural Engineering* 118 (12): 3268–3284. https://doi.org/10.1061/(asce)0733-9445(1992)118:12(3268).

Moyer, Matthew J, and Mervyn J Kowalsky. 2003. "Influence of Tension Strain on Buckling of Reinforcement in Concrete Columns." *ACI Structural Journal* 100 (1): 75–85.

Muir, D. R. 1982. "New Product Opportunities for Sulfur." In *American Chemical Society*, 127–136. https://doi.org/10.1021/bk-1982-0183.ch009.

Murakami, Y, and KJ Miller. 2005. “What Is Fatigue Damage? A View Point from the Observation of Low Cycle Fatigue Process.” *International Journal of Fatigue* 27 (8): 991–1005.

Murcia-Delso, Juan, and P. Benson Shing. 2015. “Bond-Slip Model for Detailed Finite-Element Analysis of Reinforced Concrete Structures.” *Journal of Structural Engineering* 141 (4): 04014125. https://doi.org/10.1061/(ASCE)ST.1943-541X.0001070.

Nakamura, H, and T Higai. 2002. “Modeling of Nonlinear Cyclic Behavior of Reinforcing Bars.” *Special Publication* 205: 273–292.

Nojavan, Alireza, Arturo E. Schultz, and Shih-Ho Chao. 2017. “Analytical Study of In-Plane Buckling of Longitudinal Bars in Reinforced Concrete Columns under Extreme Earthquake Loading.” *Engineering Structures* 134 (March): 48–60. https://doi.org/10.1016/j.engstruct.2016.12.003.

Nonaka, Taijiro. 1973. “An Elastic-Plastic Analysis of a Bar under Repeated Axial Loading.” *International Journal of Solids and Structures* 9 (5): 569–580.

Oldfather, W A, C A Ellis, and D M Brown. 1933. “Leonhard Euler’s Elastic Curves.” *Isis* 20 (1): 72–160.

Osgood, W R. 1951. “The Effect of Residual Stress on Column Strength.” In *Proc. 1st US Nat. Cong. Appl. Mech*, 415.

Papadrakakis, Manolis, and Kostas Loukakis. 1988. “Inelastic Cyclic Response of Restrained Imperfect Columns.” *Journal of Engineering Mechanics* 114 (2): 295–313.

Papia, Maurizio, Gaetano Russo, and Gaetano Zingone. 1988. “Instability of Longitudinal Bars in RC Columns.” *Journal of Structural Engineering* 114 (2): 445–461.

Paulay, Thomas, and MJ Nigel Priestley. 1992. “Seismic Design of Reinforced Concrete and Masonry Buildings.”

Paulson, Conrad, and JM Hanson. 1991. *Fatigue Behavior of Welded and Mechanical Splices in Reinforcing Steel*. Wiss, Janney, Elstner Associates.

Petch, NJ. 1958. “The Ductile-Brittle Transition in the Fracture of α-Iron: I.” *Philosophical Magazine* 3 (34): 1089–1097.

Priestley, MJ Nigel. 2003. *Myths and Fallacies in Earthquake Engineering, Revisited*. IUSS press.

Prota, Andrea, Fiorenzo De Cicco, and Edoardo Cosenza. 2009. “Cyclic Behavior of Smooth

Steel Reinforcing Bars: Experimental Analysis and Modeling Issues." *Journal of Earthquake Engineering* 13 (4): 500–519.

Qiu, Jianlei, Jinxin Gong, Qin Zhang, and Zhibin Feng. 2018. "Modelling for Compressive Buckling of Reinforcing Bars." *Proceedings of the Institution of Civil Engineers - Structures and Buildings*, October, 1–17. https://doi.org/10.1680/jstbu.17.00208.

Raynor, Dan J., Dawn E. Lehman, and John F. Stanton. 2002. "Bond-Slip Response of Reinforcing Bars Grouted in Ducts." *ACI Structural Journal* 99 (5): 568–576.

Restrepo, J I, F Seible, B Stephan, and M J Schoettler. 2006. "Seismic Testing of Bridge Columns Incorporating High-Performance Materials." *ACI Materials Journal* 103 (4): 496.

Restrepo, J.I. 2007. "Advanced Seismic Design Course Notes." Department of Structural Engineering, University of California, San Diego.

Restrepo-Posada, José I. 1993. "Seismic Behaviour of Connections between Precast Concrete Elements." PhD Thesis.

Rodriguez, Mario E., Juan C Botero, and Jaime Villa. 1999. "Cyclic Stress-Strain Behavior of Reinforcing Steel Including Effect of Buckling." *Journal of Structural Engineering* 125 (6): 605–612. https://doi.org/10.1061/(ASCE)0733-9445(1999)125:6(605).

Samarai, M. A., M. Laquerbe, and A. Al-Hadithi. 1985. "Sulphur Sand Mixes as Building Material." *Materials and Structures* 18: 57–65.

Sanchez, Roberto J. 2001. "Large Diameter Rebar Testing (Low-Cycle, 'High-Frequency' Fatigue Testing of Large Diameter Rebar)." Livermore: University of California.

Schoettler, Matthew J., Jose I. Restrepo, Gabriele Guerrini, David E. Duck, and Francesco Carrea. 2015. "A Full-Scale, Single-Column Bridge Bent Tested by Shake-Table Excitation." *PEER Report* 11 (3): 555–565. https://doi.org/10.1002/eqe.

Shanley, FR. 1946. "The Column Paradox." *Journal of the Aeronautical Sciences*.

Shanley, Francis R. 1947. "Inelastic Column Theory." *Journal of the Aeronautical Sciences*.

Slavin, C.M., and W.M. Ghannoum. 2015. "Defining Structurally Acceptable Properties of High-Strength Steel Bars through Material and Column Testing, PART I: MATERIAL TESTING REPORT." Techreport 05–14. University of Texas at Austin.

Steuck, Kyle P., Marc O. Eberhard, and John F. Stanton. 2009. "Anchorage of Large-Diameter Reinforcing Bars in Ducts." *ACI Structural Journal* 106 (4): 506–513.

Tanaka, Hitoshi. 1990. “Effect of Lateral Confining Reinforcement on the Ductile Behaviour of Reinforced Concrete Columns.”

Templin, RL, RG Sturm, EC Hartmann, and M Holt. 1938. “Column Strength of Various Aluminum Alloys.” *Tech. Paper* 1.

Tong, Xiao-yan, De-jun Wang, and Hao Xu. 1989. “Investigation of Cyclic Hysteresis Energy in Fatigue Failure Process.” *International Journal of Fatigue* 11 (5): 353–359.

Tripathi, Mayank, Rajesh P. Dhakal, Farhad Dashti, and Leonardo M. Massone. 2018. “Low-Cycle Fatigue Behaviour of Reinforcing Bars Including the Effect of Inelastic Buckling.” *Construction and Building Materials* 190 (November): 1226–35. https://doi.org/10.1016/j.conbuildmat.2018.09.192.

Wang, YC, and José Ignacio Restrepo. 1996. *Strength Enhancement of Concentrically Loaded Reinforced Concrete Columns Using TYFO S Fibrwrap Jackets*. Department of Civil Engineering, University of Canterbury.

Weber, Harold H. 1993. “New Applications and Expanding Markets for Sulphur Polymer Cement Concrete.” The Sulphur Institute.

Wetzel, R., and L. Coffin. 1969. *ASTM Manual on Low Cycle Fatigue Testing*. https://doi.org/10.1520/STP465-EB.

Yang, Hong, Yuntian Wu, Pengcheng Mo, and Jinke Chen. 2016. “Improved Nonlinear Cyclic Stress–Strain Model for Reinforcing Bars Including Buckling Effect and Experimental Verification.” *International Journal of Structural Stability and Dynamics* 16 (01): 1640005.

Yang, Xianjie. 2005. “Low Cycle Fatigue and Cyclic Stress Ratcheting Failure Behavior of Carbon Steel 45 under Uniaxial Cyclic Loading.” *International Journal of Fatigue* 27 (9): 1124–1132.

Zahn, Franz August. 1985. “Design of Reinforced Concrete Bridge Columns for Strength and Ductility.”

Zong, Zhiyu. 2010. *Uniaxial Material Model Incorporating Buckling for Reinforcing Bars in Concrete Structures Subjected to Seismic Loads*. University of California, Davis.

Zong, Zhiyu, Sashi Kunnath, and Giorgio Monti. 2013. “Material Model Incorporating Buckling of Reinforcing Bars in RC Columns.” *Journal of Structural Engineering* 140 (1): 04013032.

APPENDIX A

Table A.1. Sulfur concrete mix designs and material properties.

Mix Design	Sulfur (% weight)	Crushed Aggregate (% Weight)	Smooth Aggregate (% weight)	Density (lb/ft^3)	f'_c (ksi)	Age (Days)
SU01	100.0	0.0	0.0	138.0	4.23	4
SU02	100.0	0.0	0.0	138.0	3.03	4
CA01	33.8	66.2	0.0	138.0	6.84	3
CA02	34.3	65.7	0.0	139.0	5.74	3
CA03	44.1	55.9	0.0	146.0	8.52	10
CA04	35.8	64.2	0.0	143.0	6.45	1
CA05	36.2	63.8	0.0	146.0	2.41	1
CA06	37.3	62.7	0.0	142.0	4.29	6
CA07	39.5	60.5	0.0	138.0	1.45	5
SA01	31.3	0.0	68.7	157.0	3.75	1
SA02	31.2	0.0	68.8	157.0	4.25	1
SA03	31.2	0.0	68.8	158.0	4.38	1
SA04	31.1	0.0	68.9	158.0	4.04	1
SA05	31.0	0.0	69.0	158.0	3.46	11
SA06	31.2	0.0	68.8	158.0	4.03	11
SA07	31.3	0.0	68.7	158.0	3.93	18
SA08	38.1	0.0	61.9	150.0	2.67	9
SA09	37.9	0.0	62.1	149.0	2.50	6
MA01	31.0	32.5	36.5	151.0	5.81	2
MA02	33.5	33.8	35.7	157.0	6.29	2
MA03	34.2	34.8	32.3	154.0	4.93	2
MA04	34.7	39.8	26.8	152.0	5.26	1
MA05	34.3	39.2	26.5	154.0	4.86	1
MA06	34.7	39.8	26.8	152.0	1.68	1
MA07	37.0	31.5	37.4	143.0	3.12	6
MA08	36.0	30.6	36.4	148.0	3.69	6

APPENDIX B

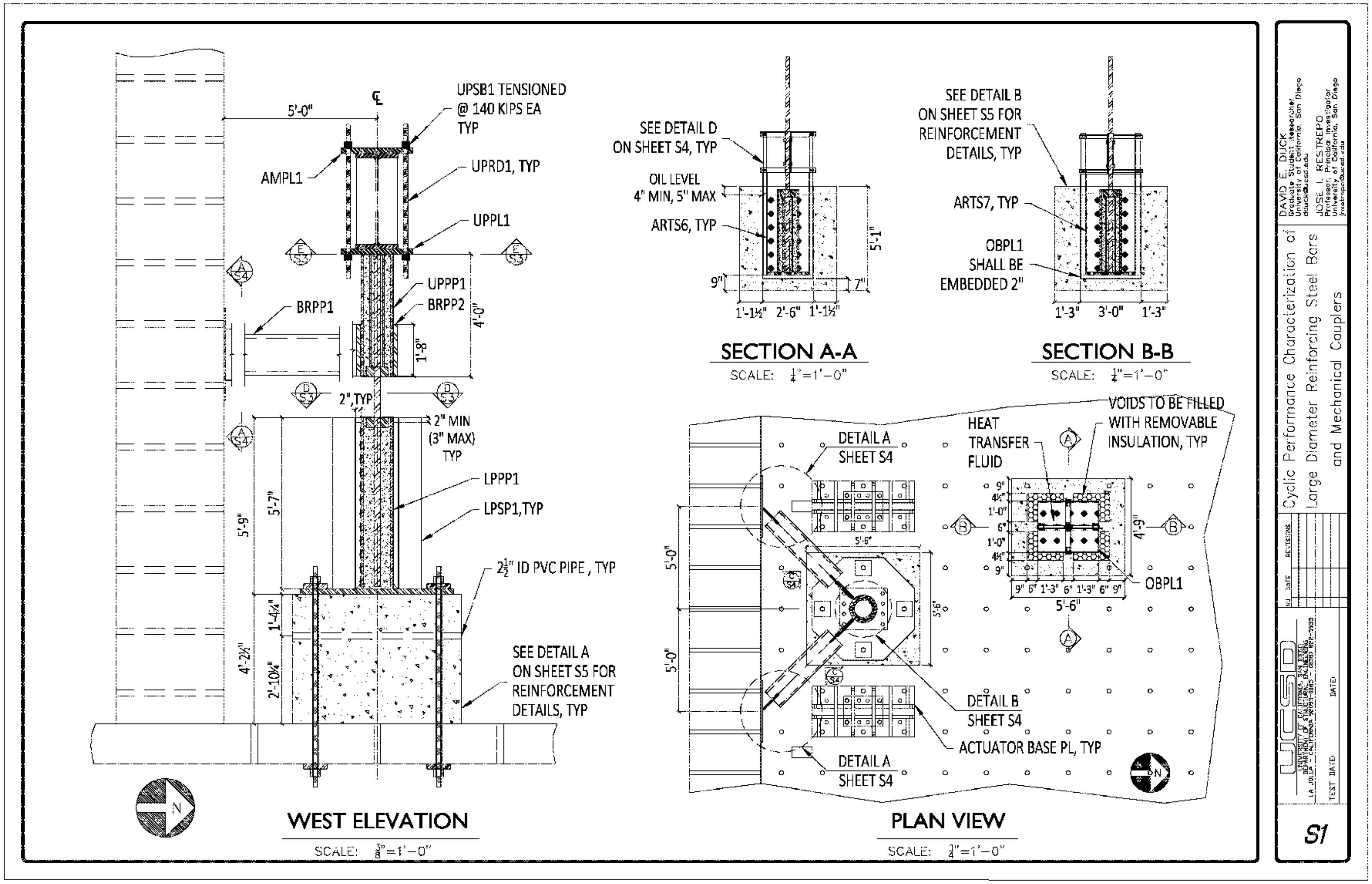

Figure B.1. Loading frame apparatus fabrication drawings.

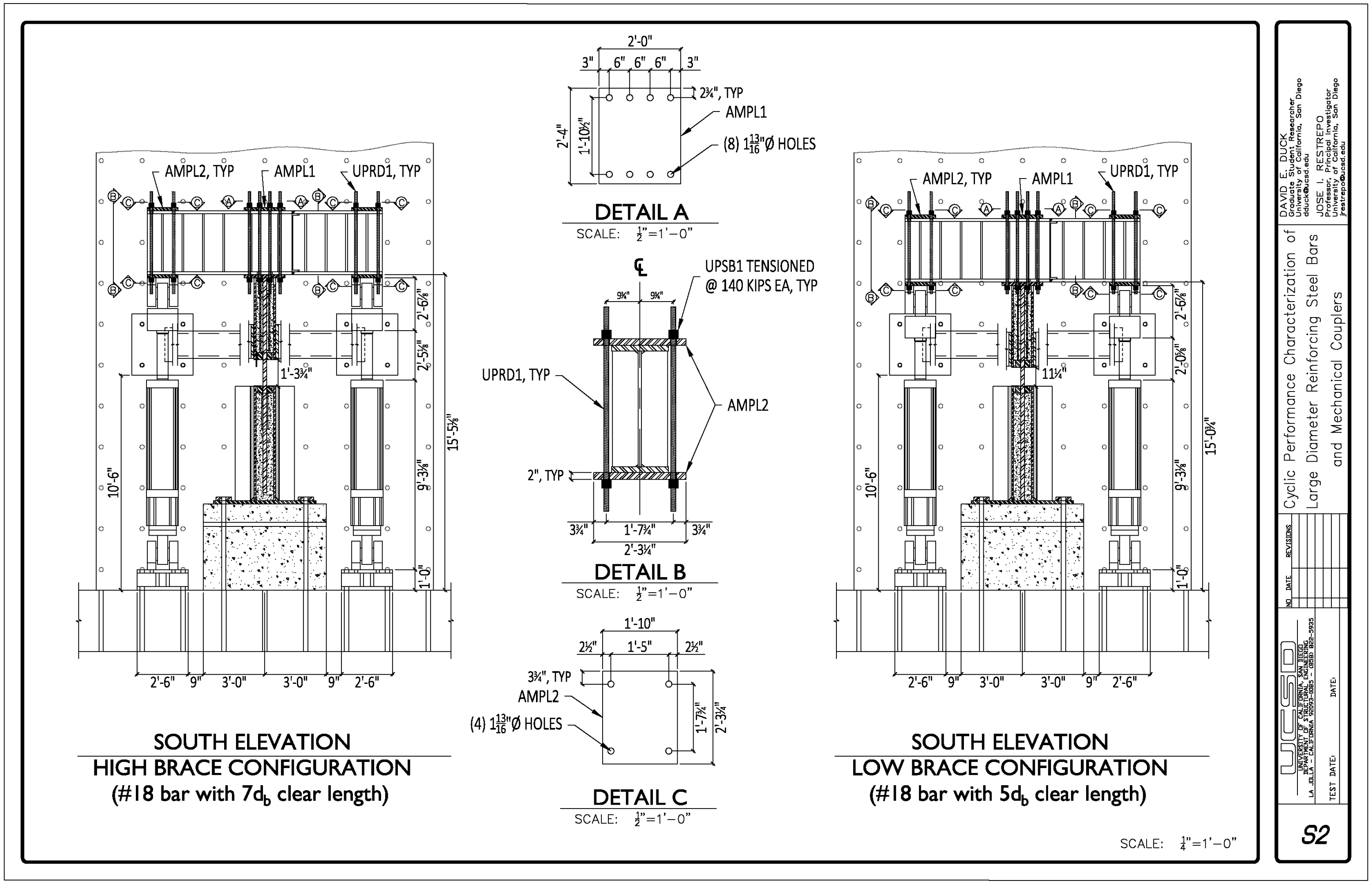

Figure B.2. Loading frame apparatus fabrication drawings.

APPENDIX C

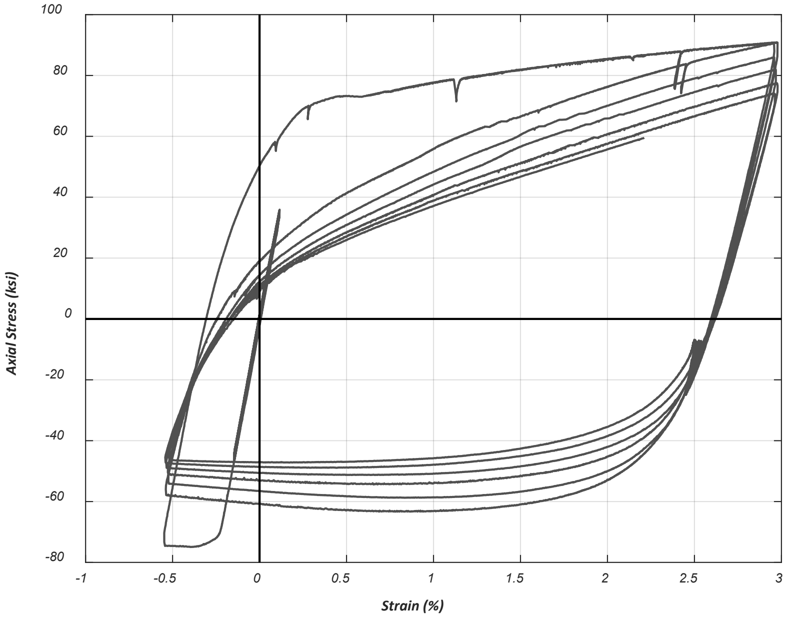

Figure C.1. Axial stress-strain response of No. 18 bar with 8.06*d_b* aspect ratio subjected to constant amplitude cycles of +3.0%, -0.5% (Specimen14).

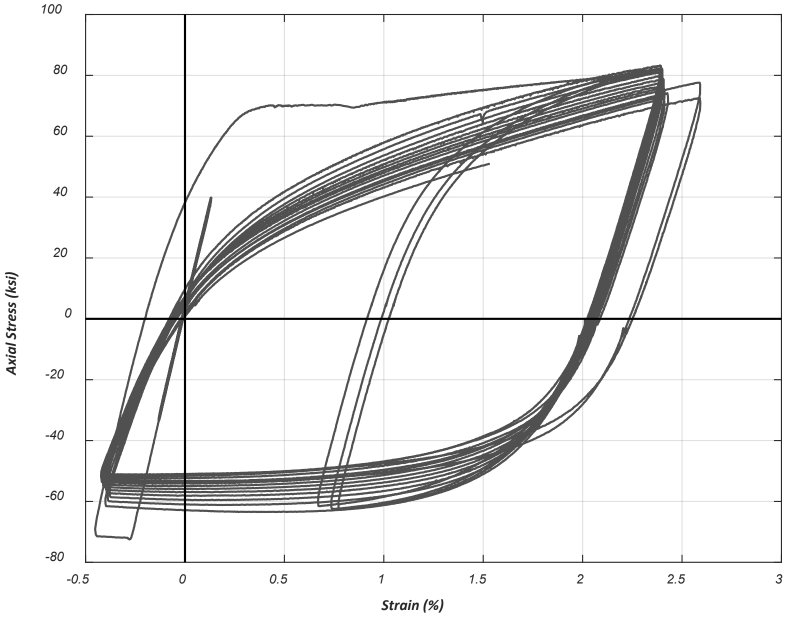

Figure C.2. Axial stress-strain response of No. 18 bar with 8*d_b* aspect ratio subjected to constant amplitude cycles of +2.4%, -0.45% (Specimen15).

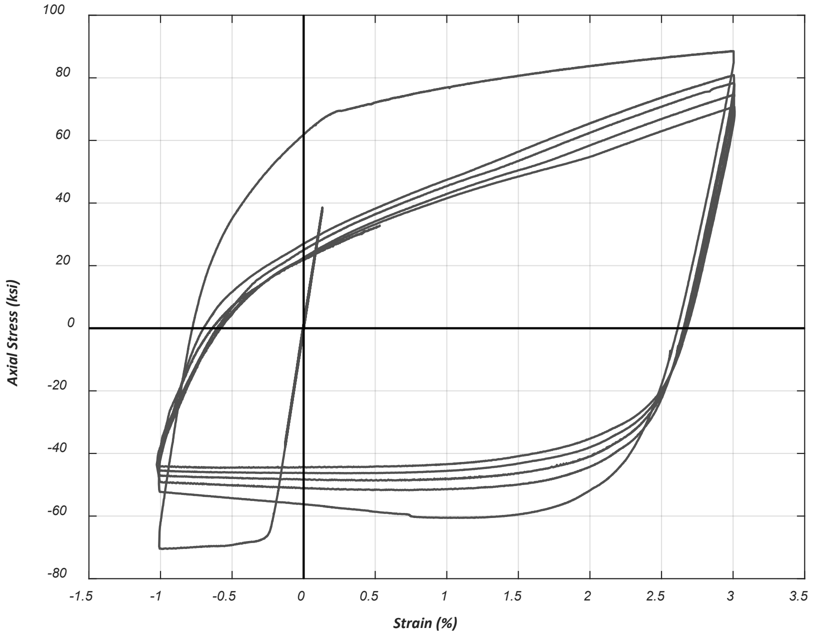

Figure C.3. Axial stress-strain response of No. 18 bar with 8.11d_b aspect ratio subjected to constant amplitude cycles of +3.0%, -1.0% (Specimen17).

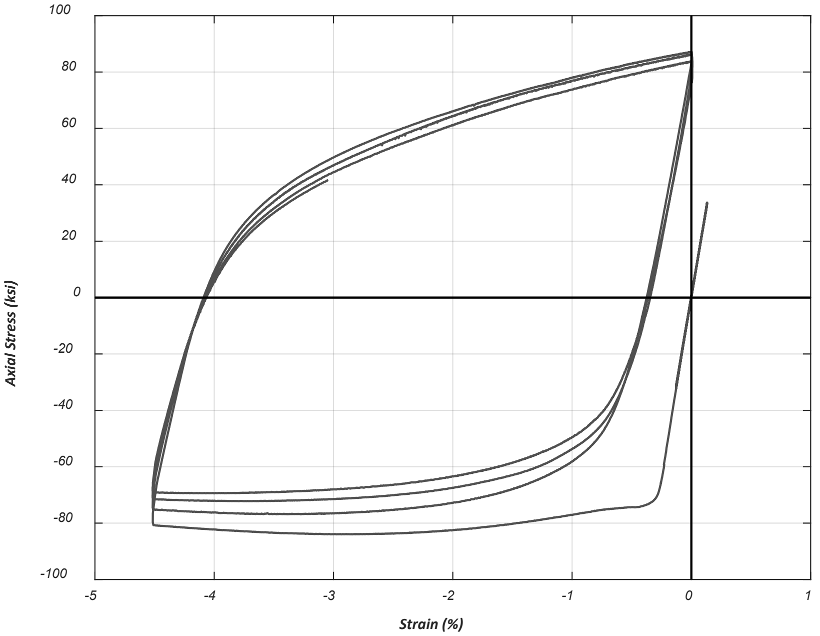

Figure C.4. Axial stress-strain response of No. 18 bar with 6d_b aspect ratio subjected to constant amplitude cycles of +0.0%, -4.5% (Specimen21).

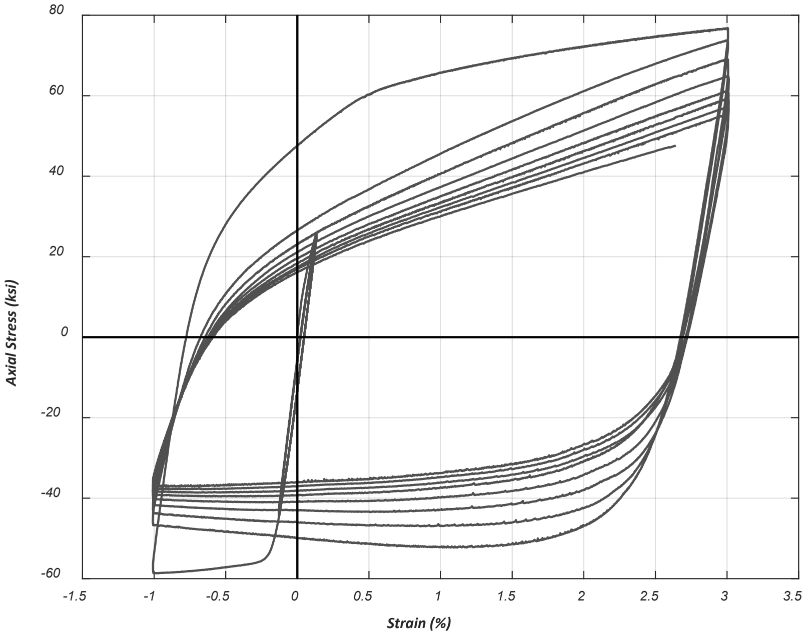

Figure C.5. Axial stress-strain response of No. 18 bar with 7.89d_b aspect ratio subjected to constant amplitude cycles of +3.0%, -1.0% (Specimen31).

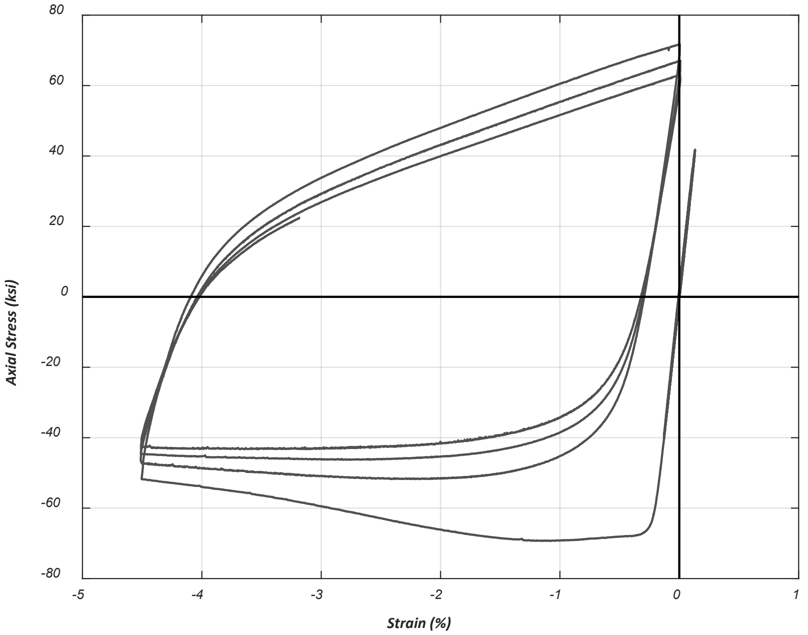

Figure C.6. Axial stress-strain response of No. 18 bar with 8d_b aspect ratio subjected to constant amplitude cycles of +0.0%, -4.5% (Specimen32).

APPENDIX D

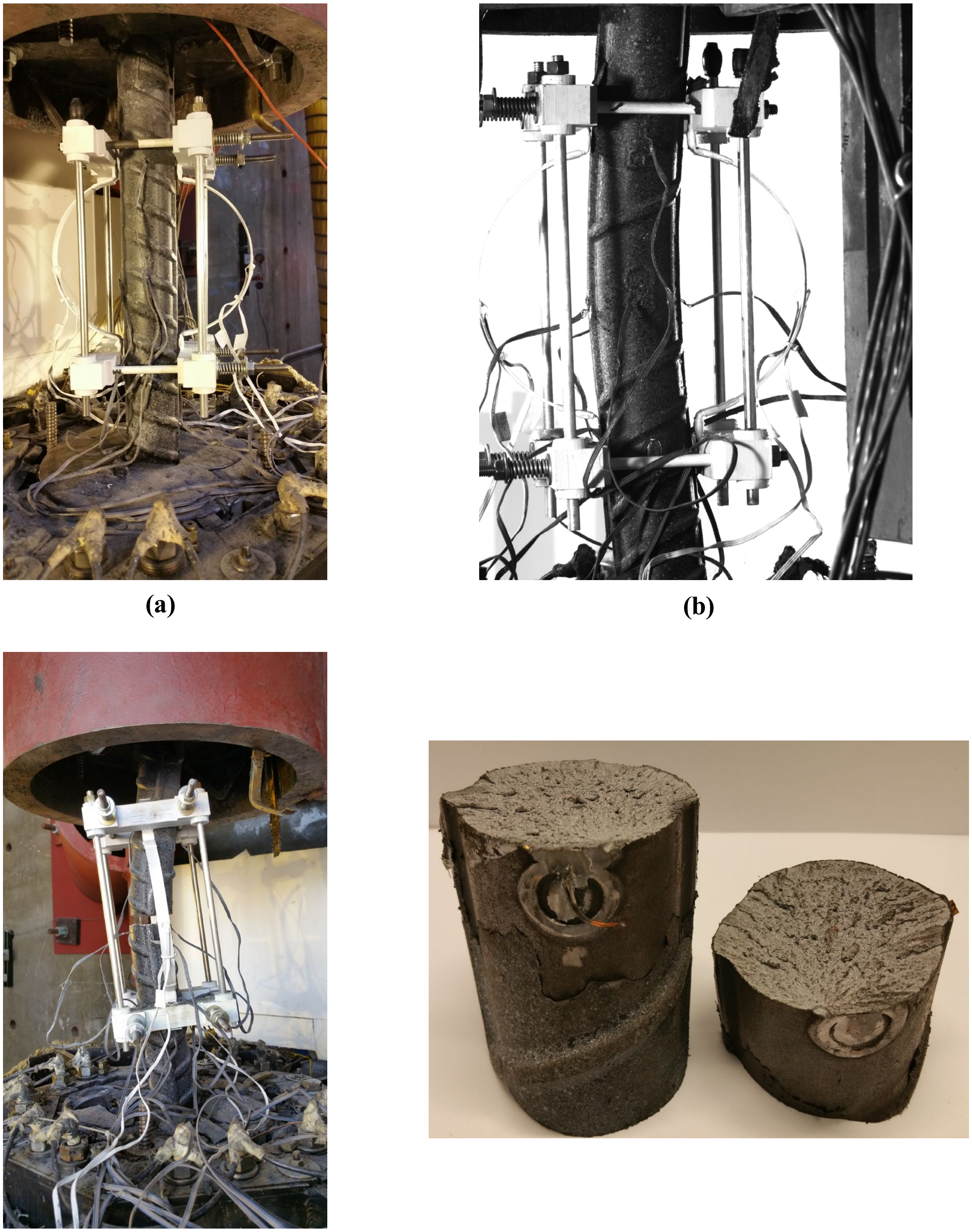

(a)

(b)

(c)

(d)

Figure D.1. Specimen14: (a) Instrumented bar; (b) Buckled bar; (c) Fractured bar; (d) Fracture surface and micro-cracks.

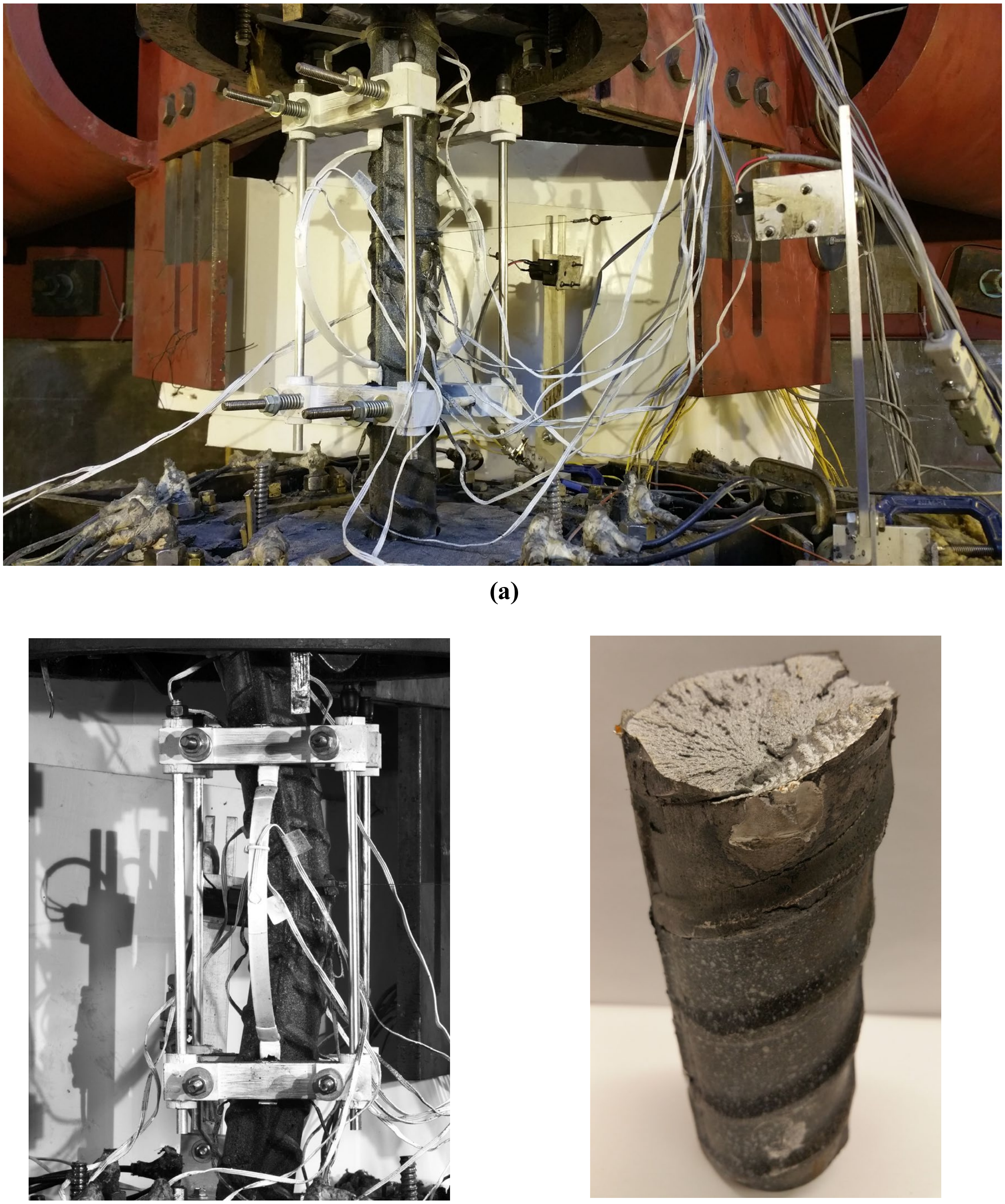

(a)

(b)

(c)

Figure D.2. Specimen15: (a) Instrumented bar; (b) Buckled bar; (c) Fracture surface and micro-cracks.

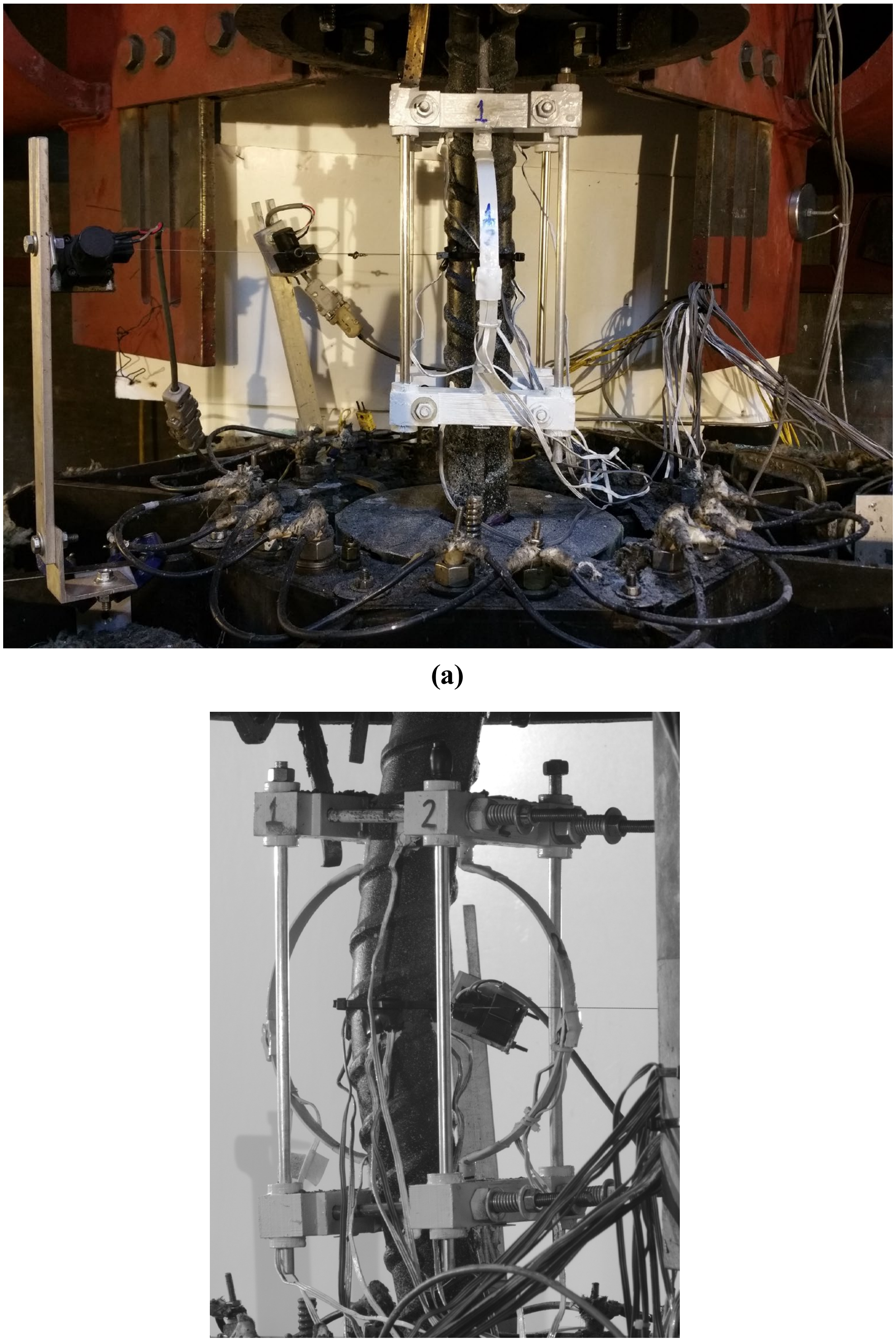

(a)

(b)

Figure D.3. Specimen16: (a) Instrumented bar; (b) Buckled bar.

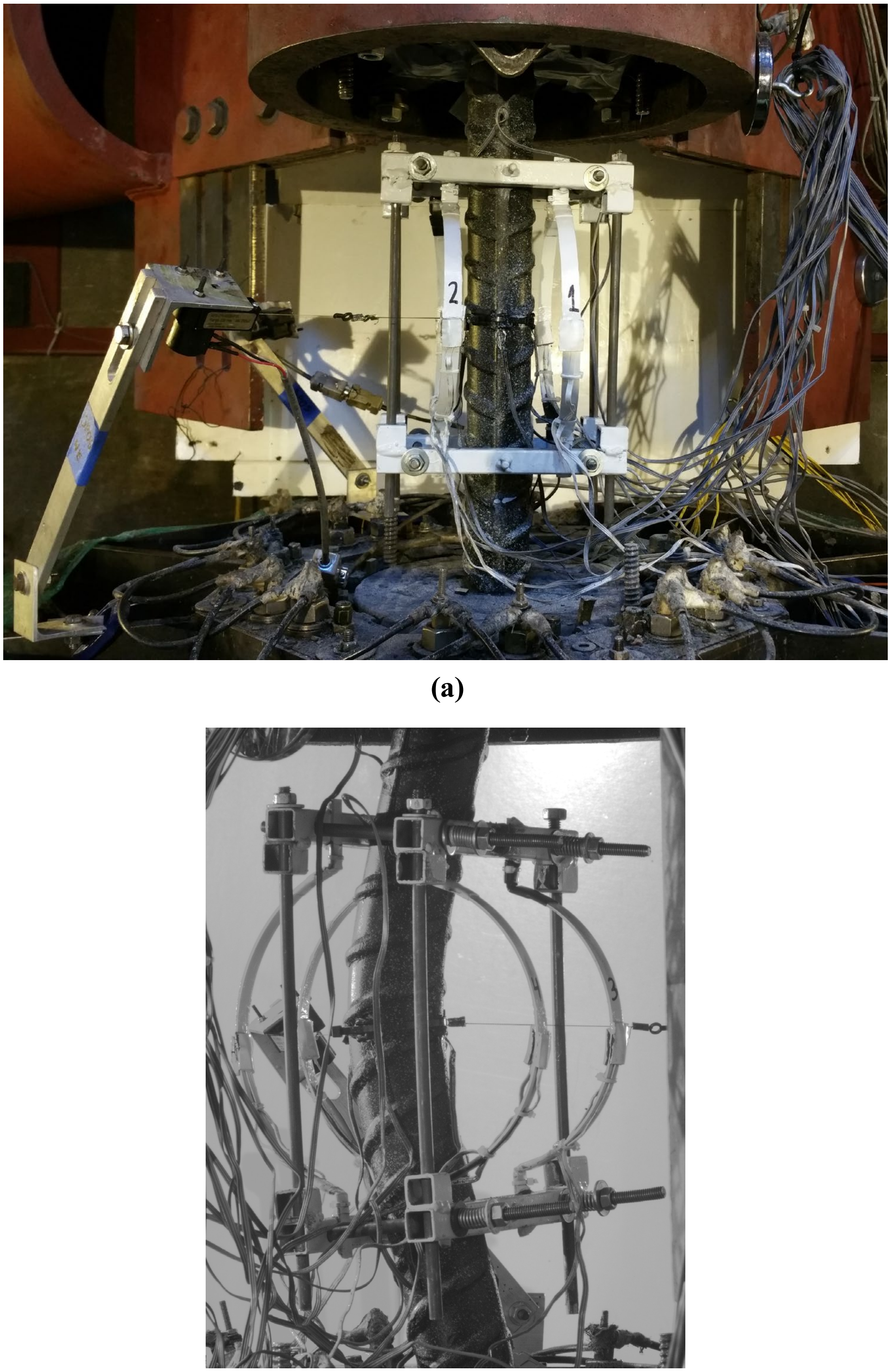

(a)

(b)

Figure D.4. Specimen18: (a) Instrumented bar; (b) Buckled bar.

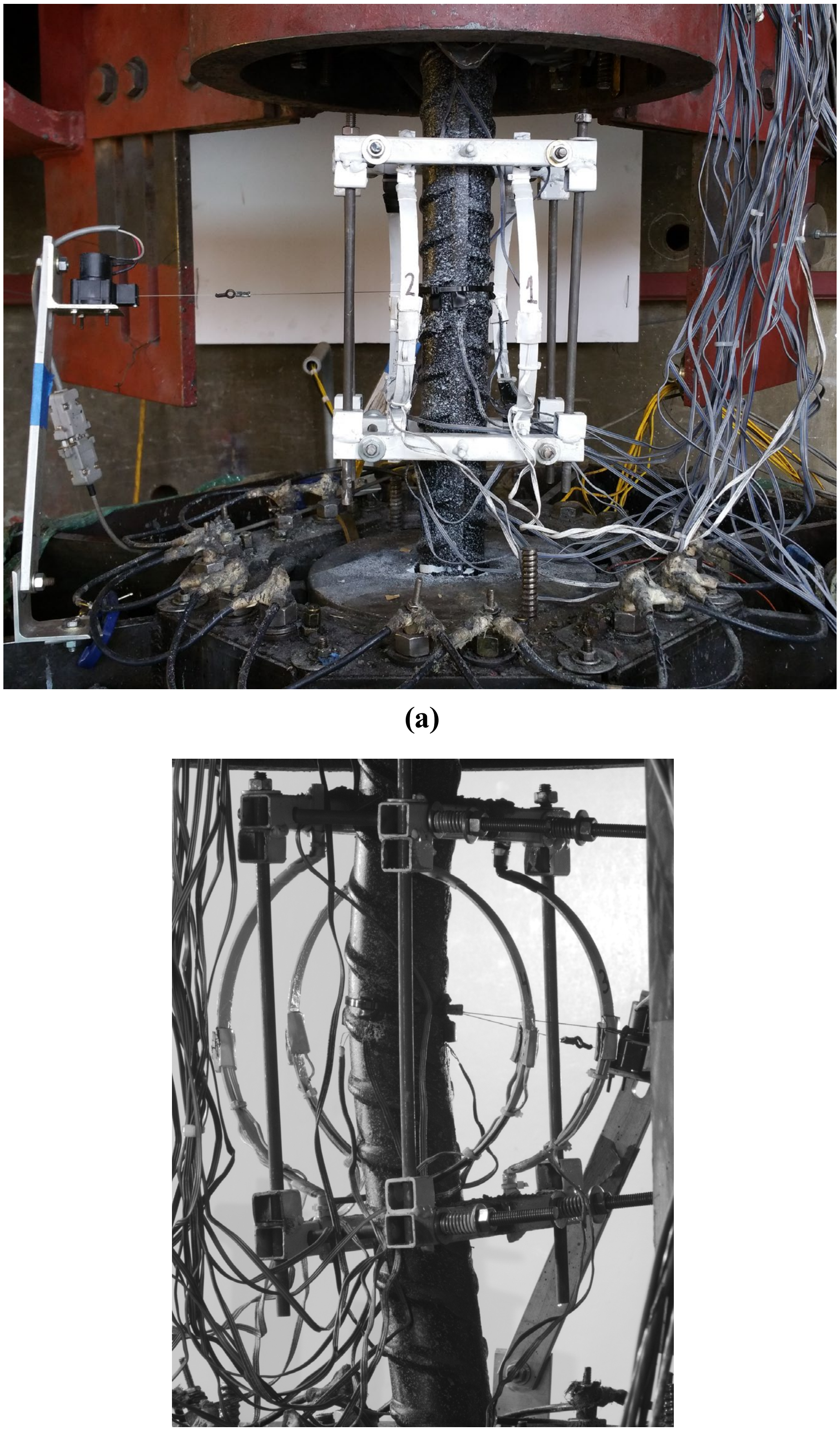

(a)

(b)

Figure D.5. Specimen19: (a) Instrumented bar; (b) Buckled bar.

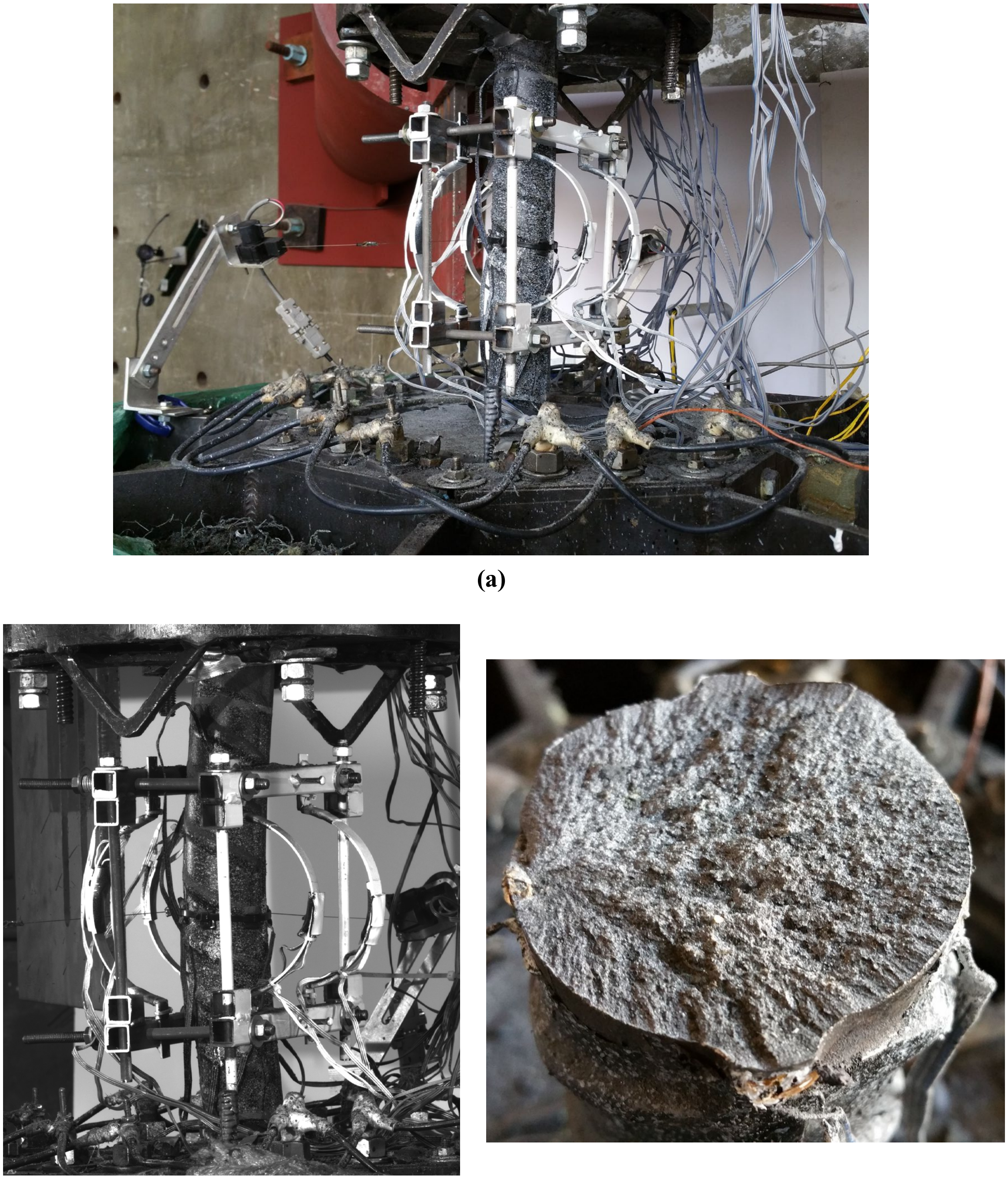

(a)

(b)

(c)

Figure D.6. Specimen 20: (a) Instrumented bar; (b) Buckled bar; (c) Fracture surface.

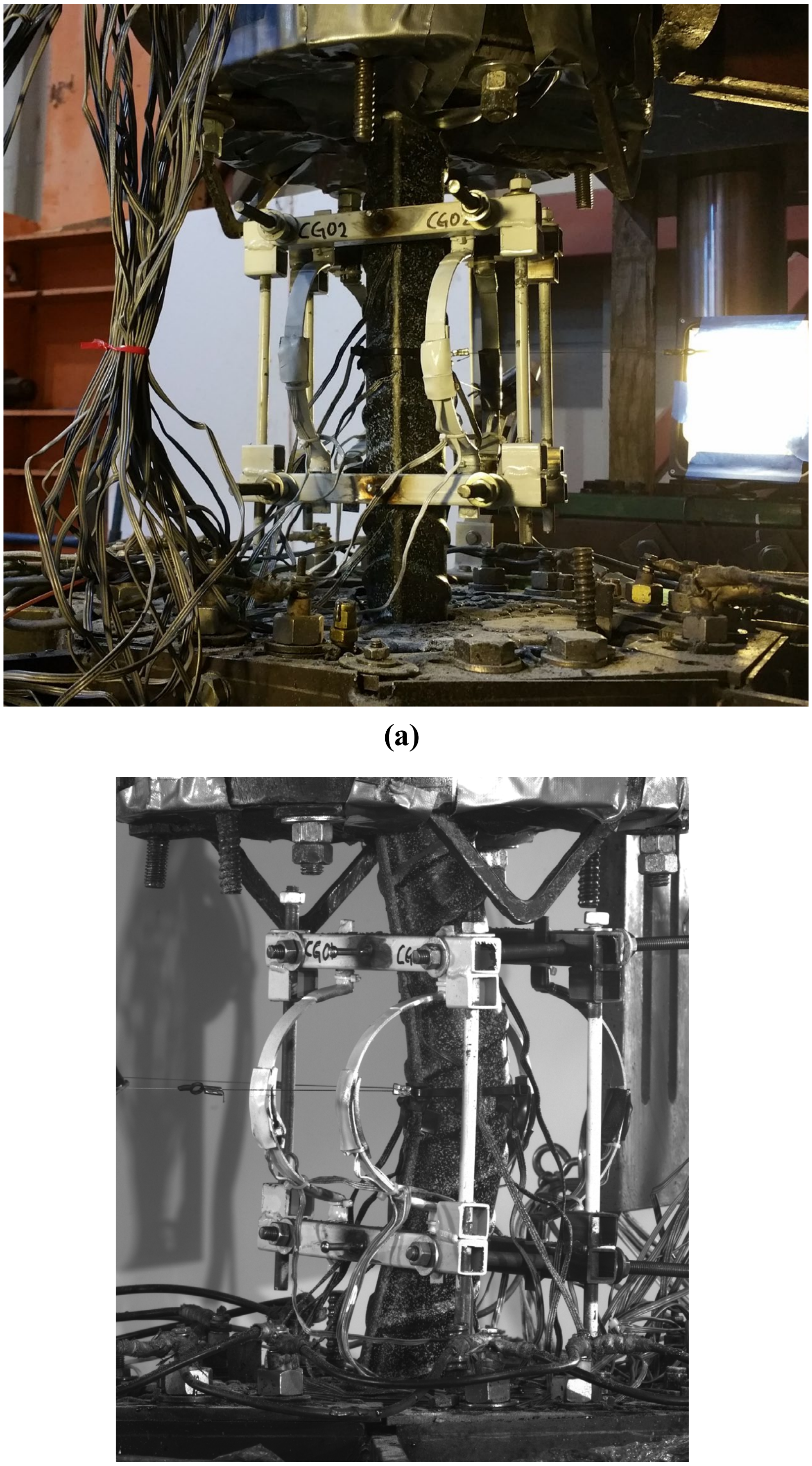

(a)

(b)

Figure D.7. Specimen21 (a) Instrumented bar; (b) Buckled bar.

(a)

(b)

Figure D.8. Specimen22: (a) Instrumented bar; (b) Buckled bar.

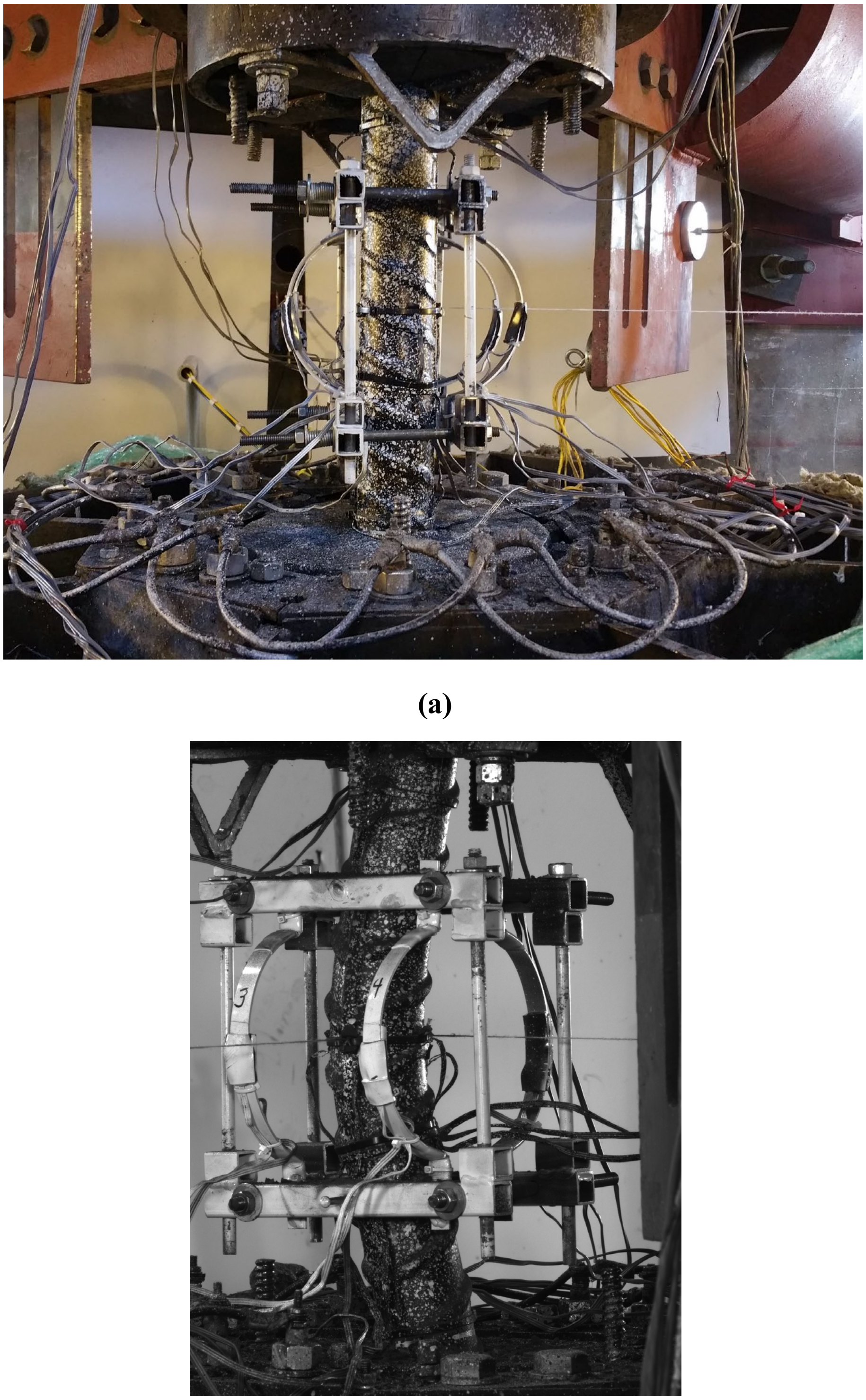

(a)

(b)

Figure D.9. Specimen23: (a) Instrumented bar; (b) Buckled bar.

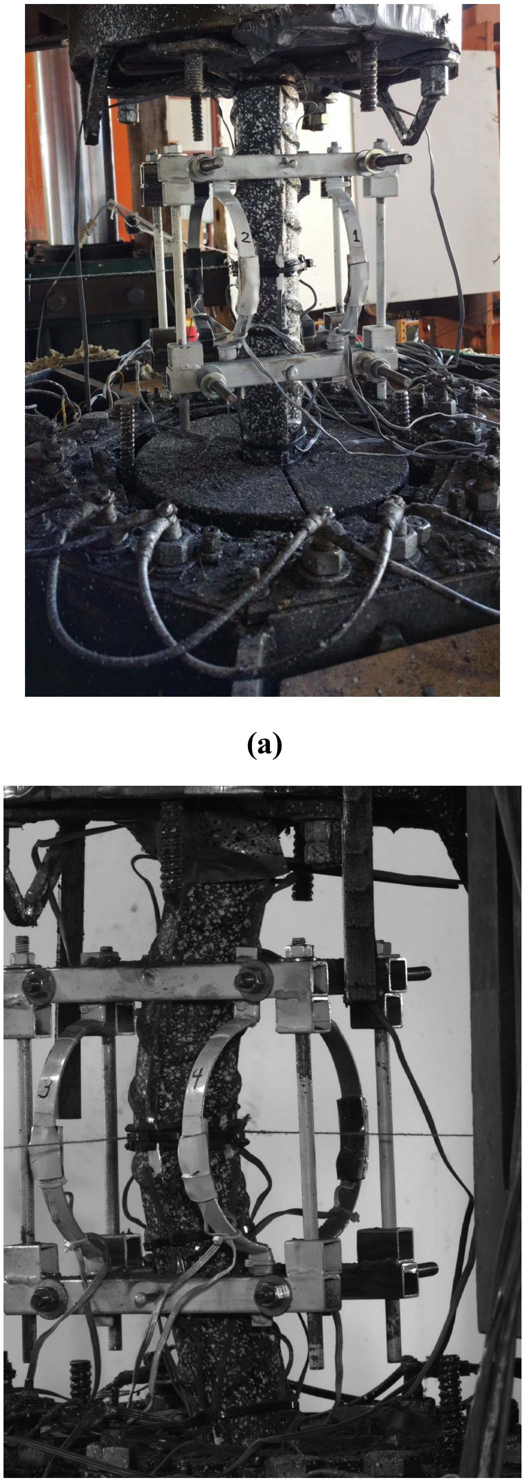

Figure D.10. Specimen24: (a) Instrumented bar; (b) Buckled bar.

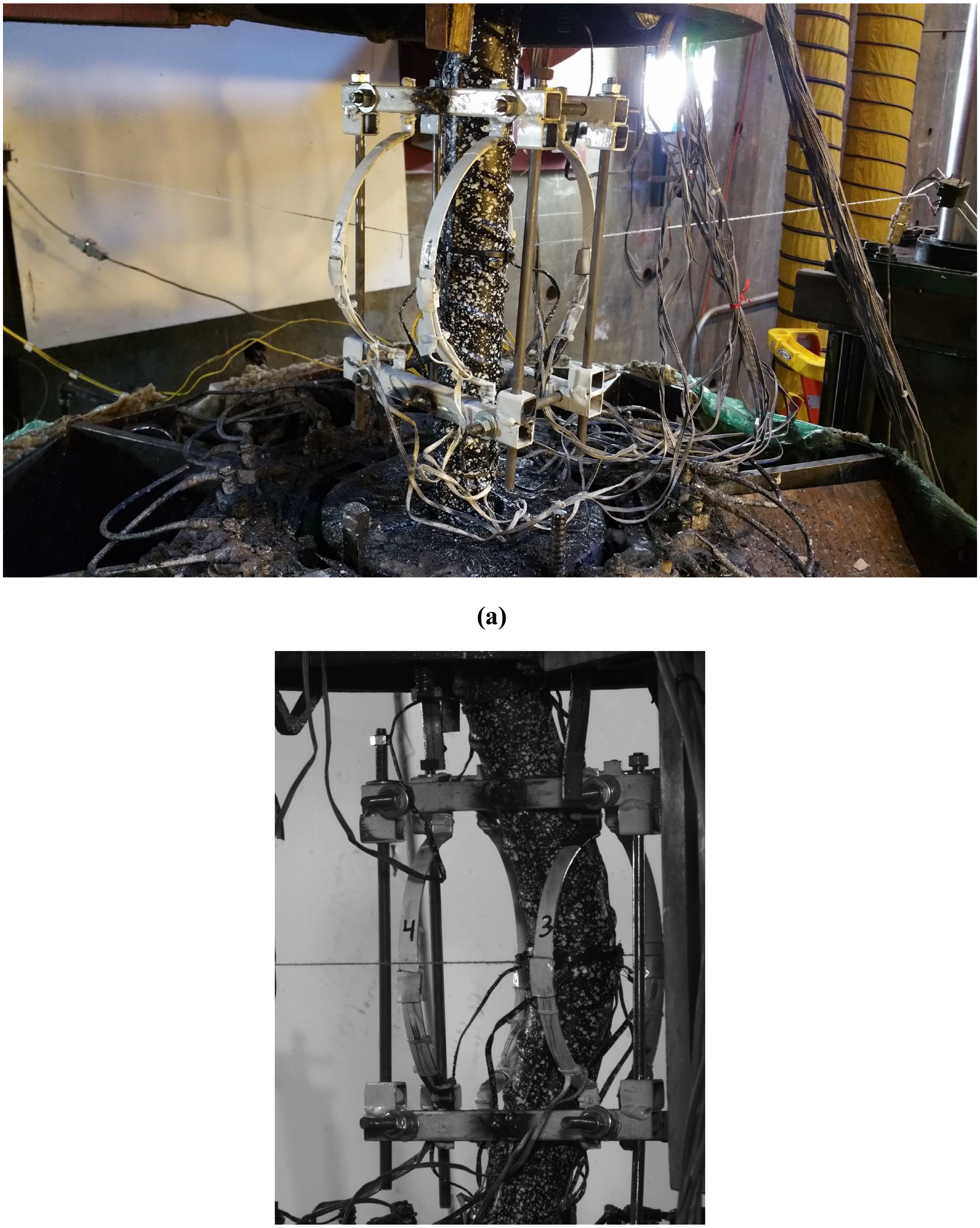

(a)

(b)

Figure D.11. Specimen25: (a) Instrumented bar; (b) Buckled bar.

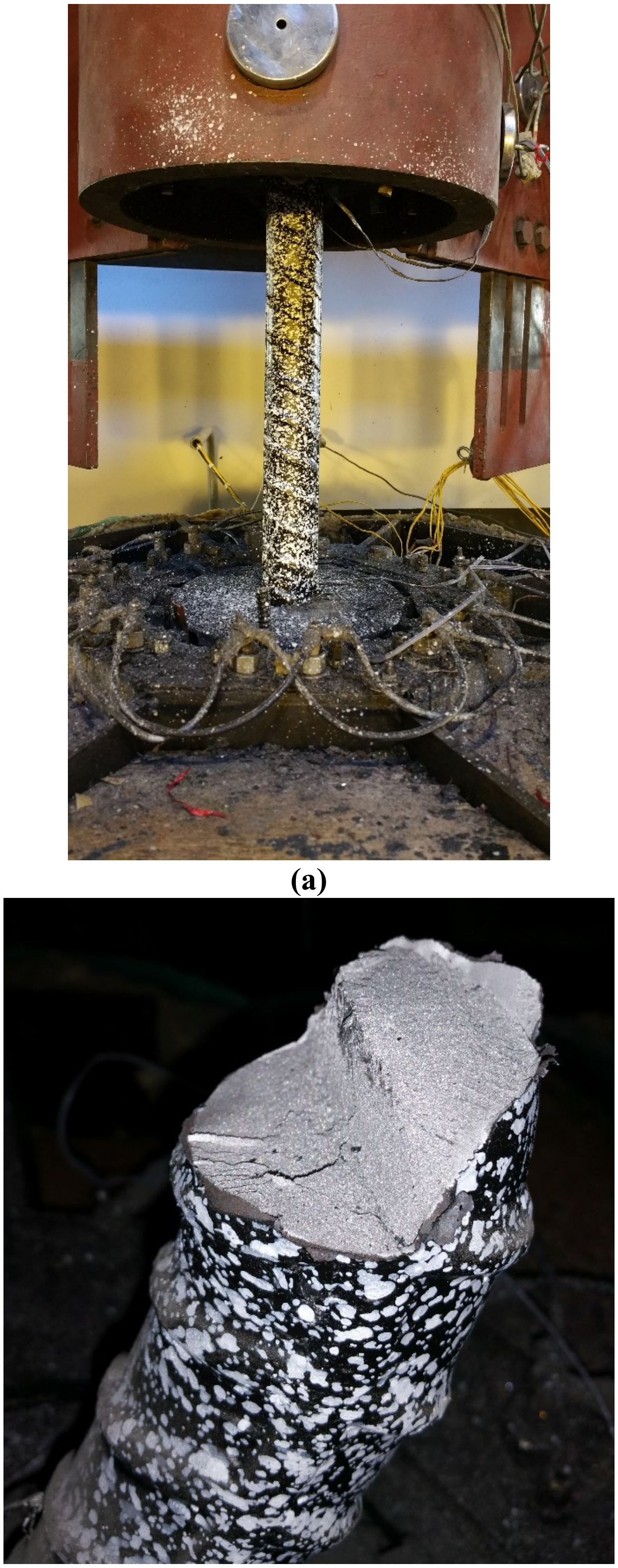

(a)

(b)

Figure D.12. Specimen 26: (a) Test bar; (b) Fracture surface.

Figure D.13. Specimen28 Instrumented bar.

(a)

(b)

Figure D.14. Specimen29: (a) Instrumented bar; (b) Fracture surface.

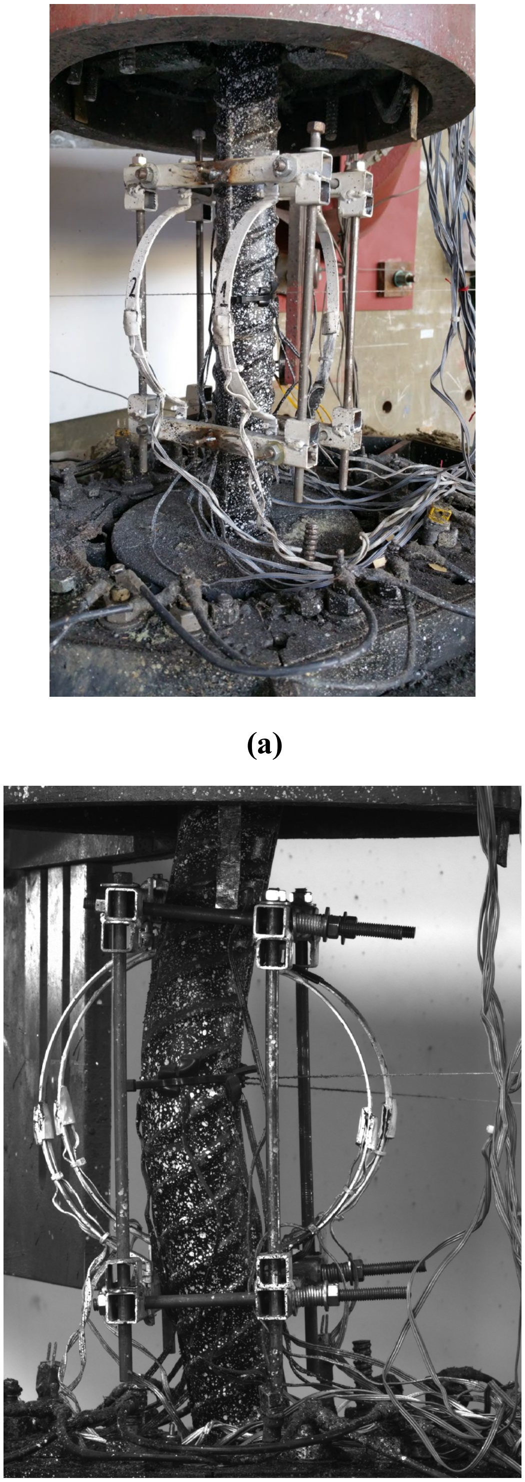

(a)

(b)

Figure D.15. Specimen 31: (a) Instrumented bar; (b) Buckled bar.

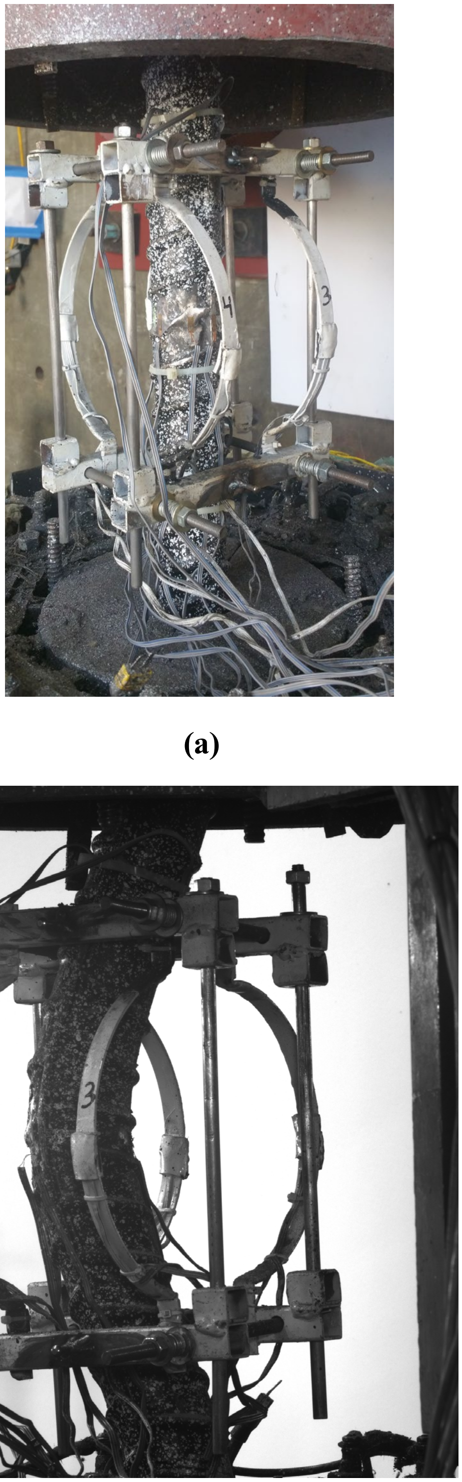

(a)

(b)

Figure D.16. Specimen32: (a) Instrumented bar; (b) Buckled bar.

APPENDIX E

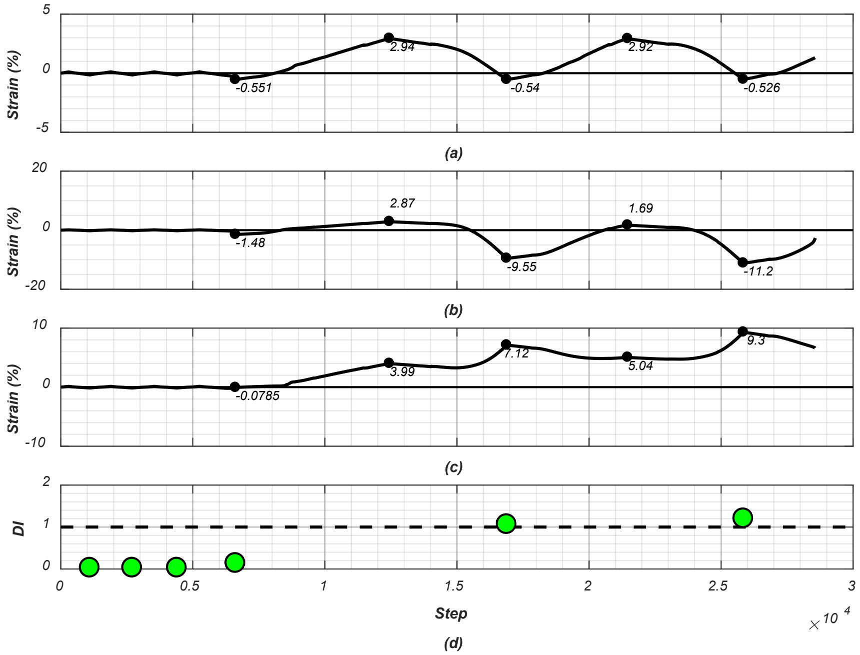

Figure E.1. Specimen14: (a) Average natural strain between theoretical POI; (b) Natural strain history on concave side of bar at mid-height; (c) Natural strain history on concave side of bar at mid-height; (d) Damage index.

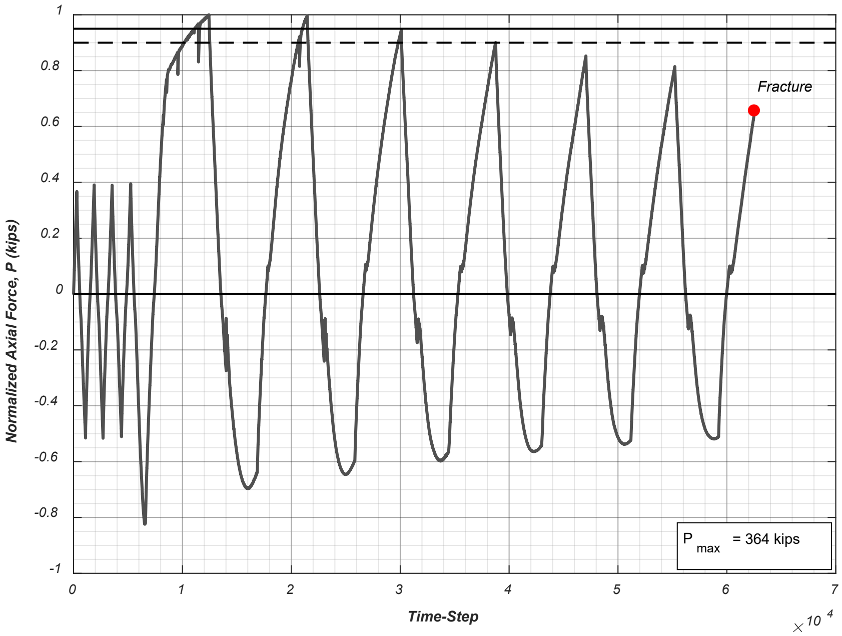

Figure E.2. Axial load history with horizontal lines indicating 90% and 95% of the maximum tensile force (Specimen14).

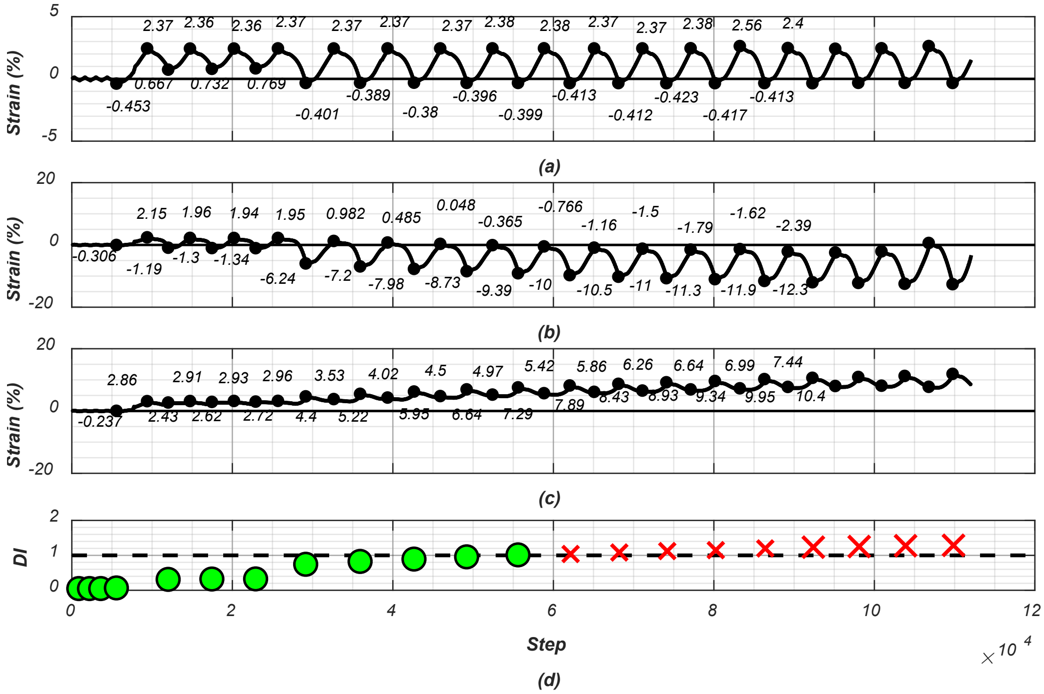

Figure E.3. Specimen15: (a) Average natural strain between theoretical POI; (b) Natural strain history on concave side of bar at mid-height; (c) Natural strain history on concave side of bar at mid-height; (d) Damage index.

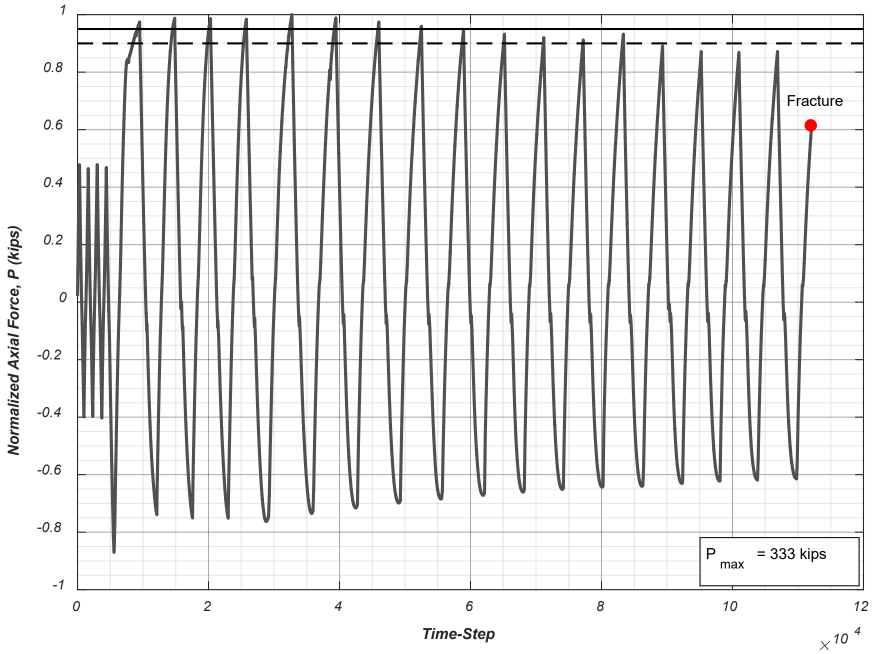

Figure E.4. Axial load history with horizontal lines indicating 90% and 95% of the maximum tensile force (Specimen15).

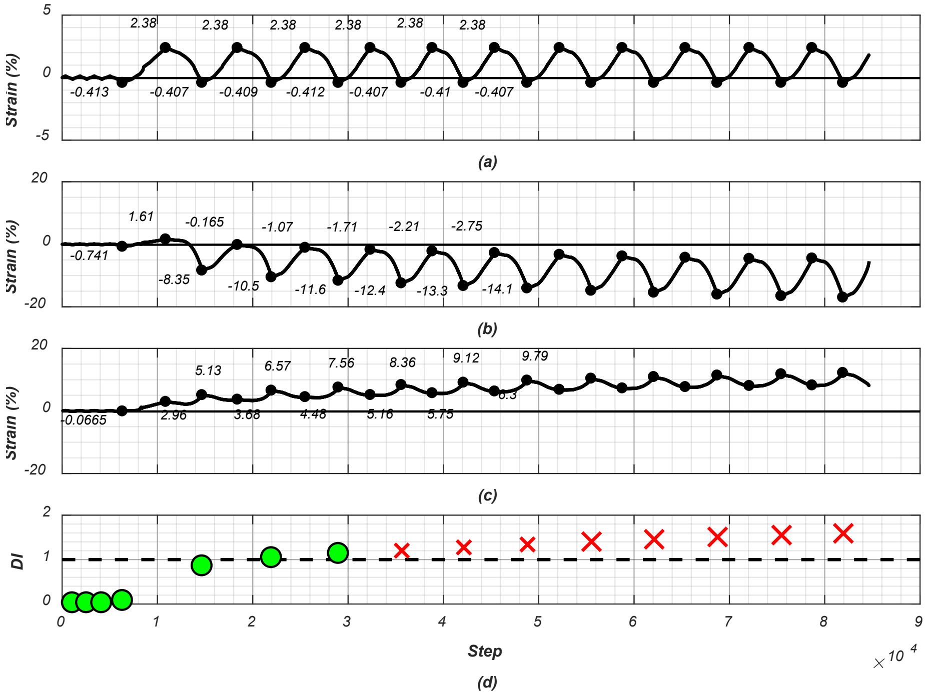

Figure E.5. Specimen16: (a) Average natural strain between theoretical POI; (b) Natural strain history on concave side of bar at mid-height; (c) Natural strain history on concave side of bar at mid-height; (d) Damage index.

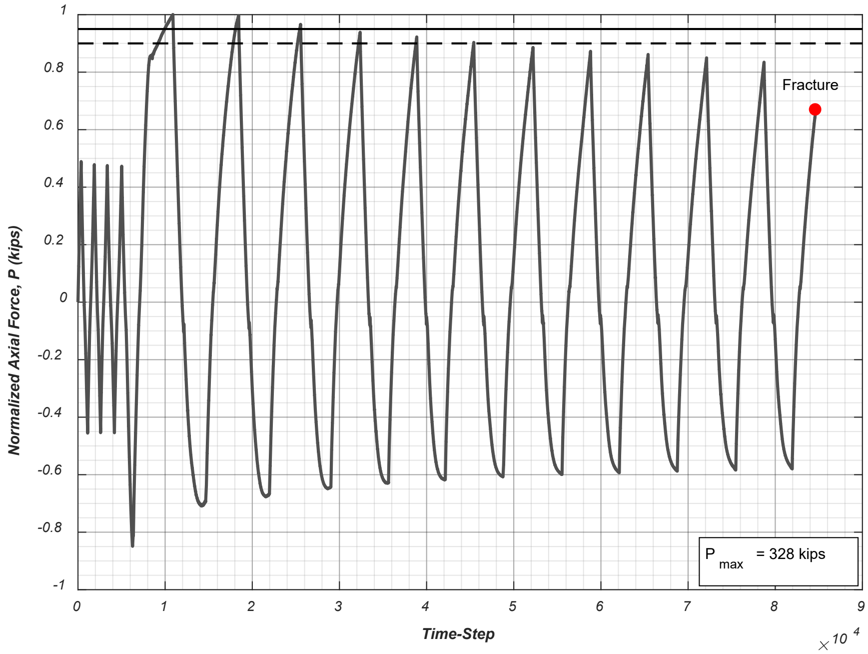

Figure E.6. Axial load history with horizontal lines indicating 90% and 95% of the maximum tensile force (Specimen16).

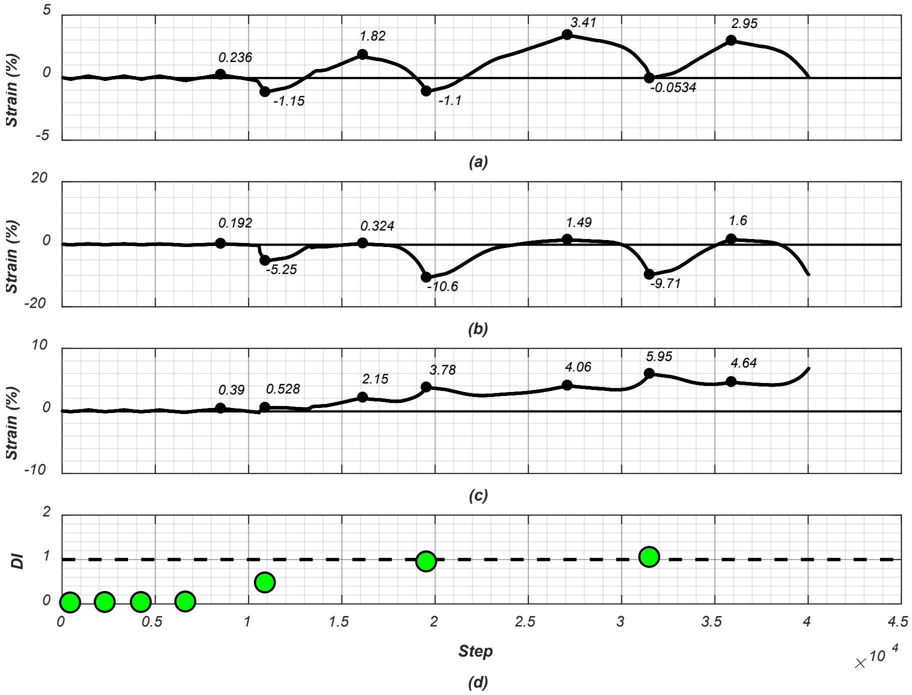

Figure E.7. Specimen19: (a) Average natural strain between theoretical POI; (b) Natural strain history on concave side of bar at mid-height; (c) Natural strain history on concave side of bar at mid-height; (d) Damage index.

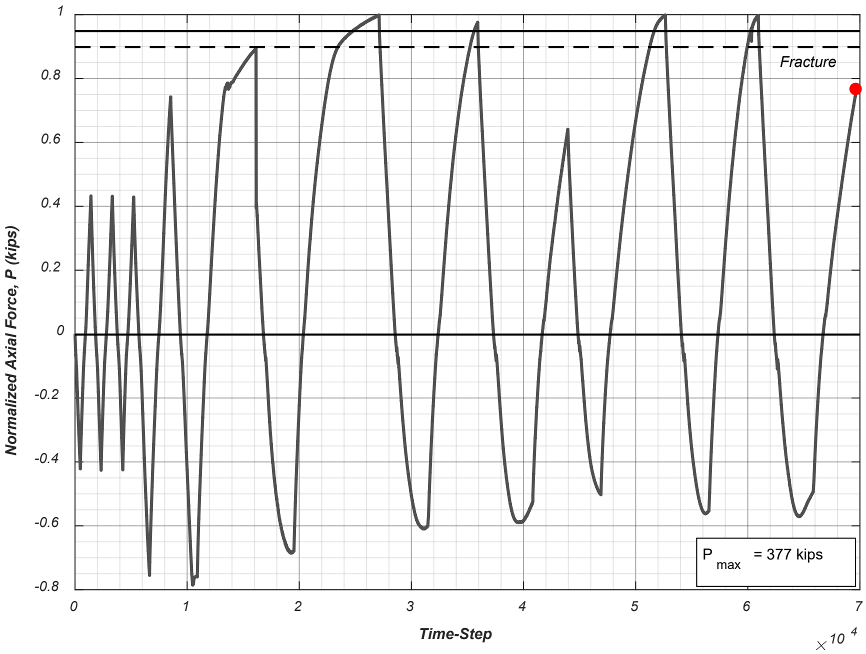

Figure E.8. Axial load history with horizontal lines indicating 90% and 95% of the maximum tensile force (Specimen19).

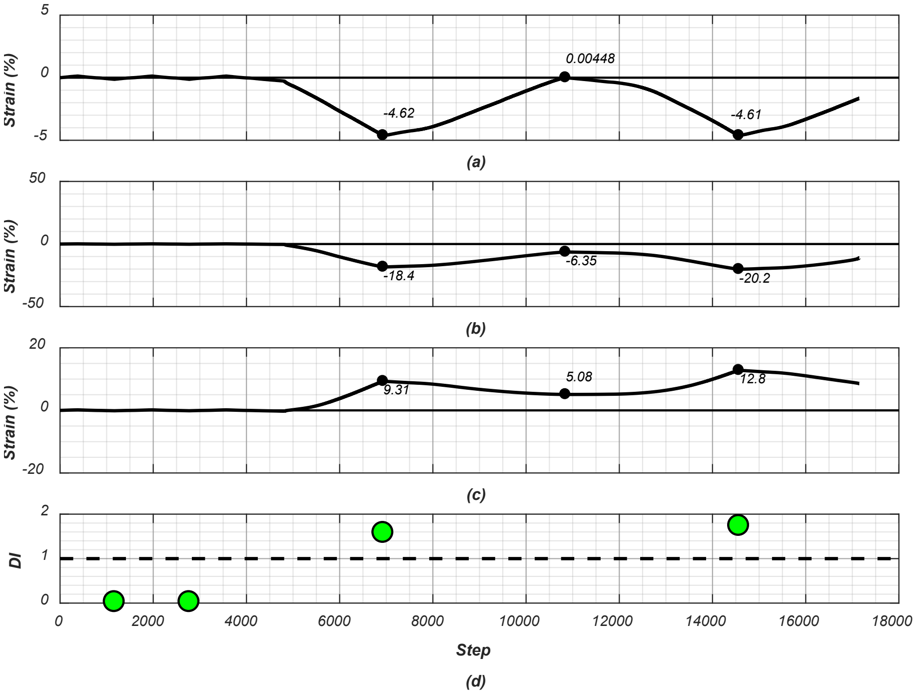

Figure E.9. Specimen25: (a) Average natural strain between theoretical POI; (b) Natural strain history on concave side of bar at mid-height; (c) Natural strain history on concave side of bar at mid-height; (d) Damage index.

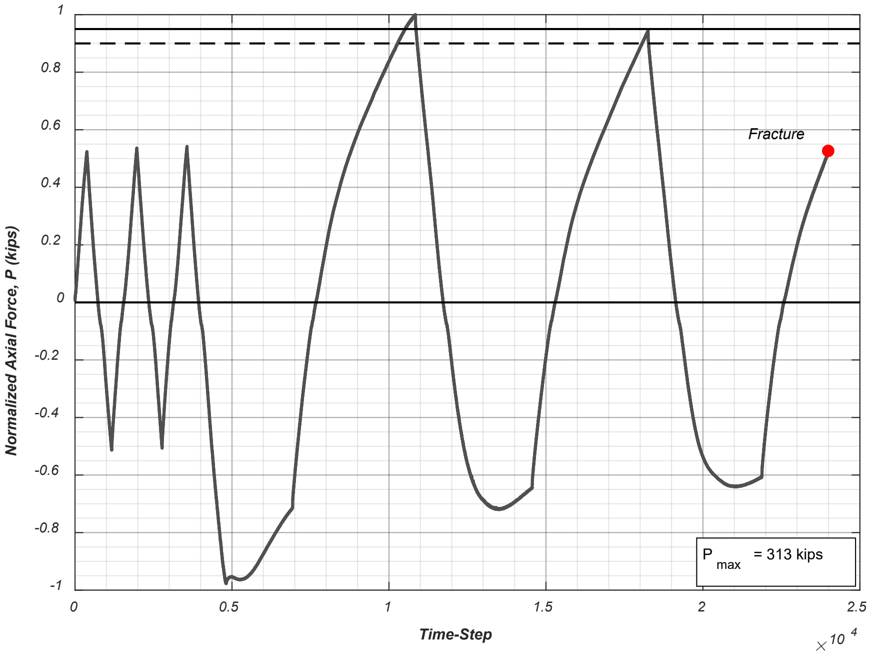

Figure E.10. Axial load history with horizontal lines indicating 90% and 95% of the maximum tensile force (Specimen25).

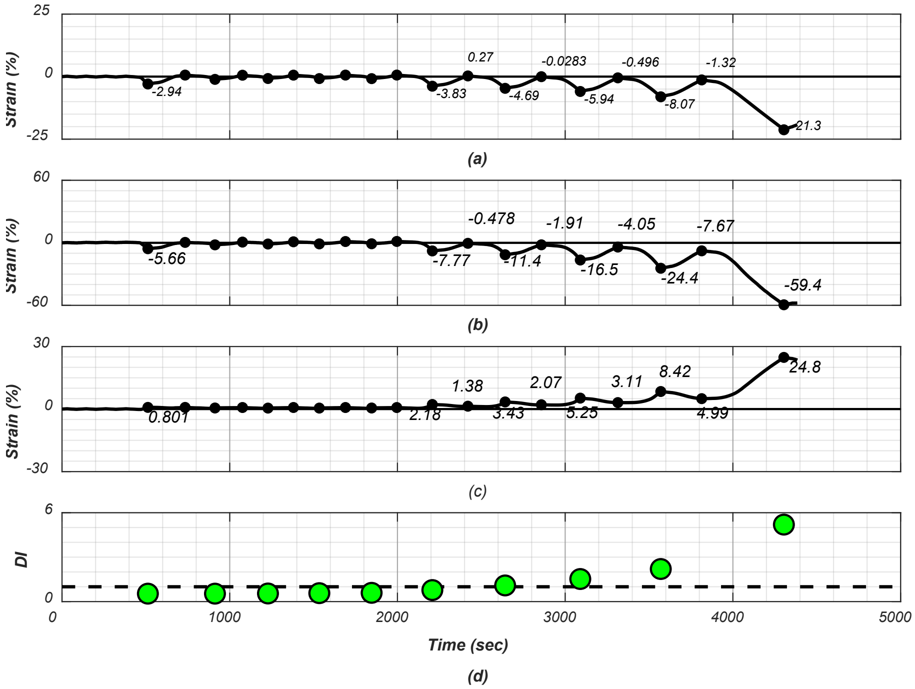

Figure E.11. Specimen26: (a) Average natural strain between theoretical POI; (b) Natural strain history on concave side of bar at mid-height; (c) Natural strain history on concave side of bar at mid-height; (d) Damage index.

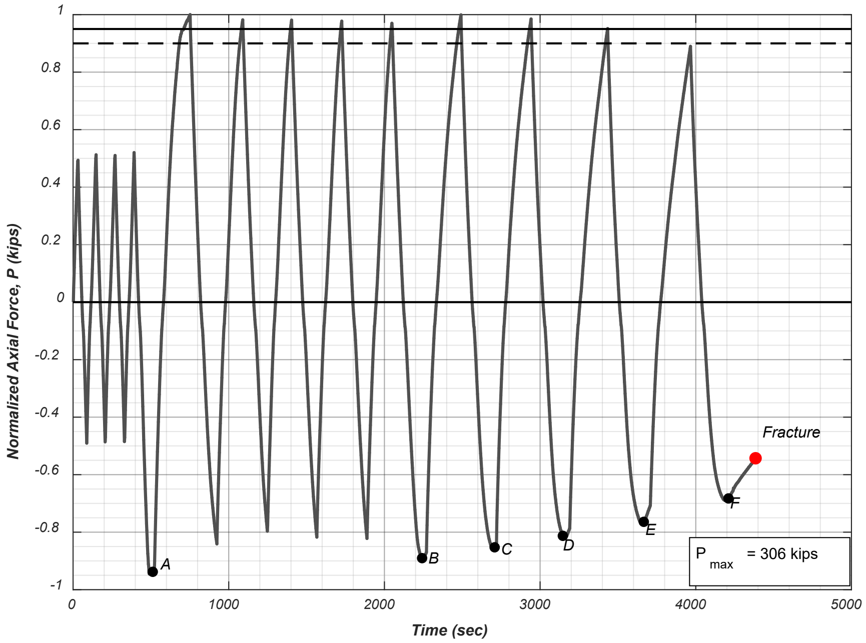

Figure E.12. Axial load history with horizontal lines indicating 90% and 95% of the maximum tensile force (Specimen26).